HIGH PERFORMANCE SHORT CHANNEL ORGANIC ELECTROCHEMICAL TRANSISTORS FOR BIOELECTRONICS

LIU HONG

PhD

The Hong Kong Polytechnic University

2023

The Hong Kong Polytechnic University

Department of Applied Physics

High Performance Short Channel Organic Electrochemical Transistors for Bioelectronics

LIU Hong

A thesis submitted in partial fulfillment of the requirements for
the degree of Doctor of Philosophy

August 2022

CERTIFICATE OF ORIGINALITY

I hereby declare that this thesis is my own work and that, to the best of my knowledge and belief, it reproduces no material previously published or written, nor material that has been accepted for the award of any other degree or diploma, except where due acknowledgement has been made in the text.

__________________ (Signed)

___LIU Hong________________ (Name of student)

Abstract

Organic electrochemical transistors (OECTs) are characterized by ion infusion into channel volume during gate modulation. The electric and ionic charges couple within the channel of OECTs, leading to much higher transconductance than that of a field-effect transistor. OECTs are well studied in channel materials and the application of biosensing. However, short-channel devices have been rarely reported. In this thesis, I will focus on the fabrication and application of short-channel OECTs as follows:

Firstly, vertical short-channel OECTs are prepared with aluminum oxide as a spacer between source and drain electrodes. Short-channel OECTs with physical channel lengths down to 0.86 nm have been realized, which show high on-off current ratio and low gate leakage. For both p-type and n-type short-channel OECTs, an on-off ratio of 10^6 in channel currents and an ideal subthreshold slope of 60 mV/dec have been achieved when the channel length is longer than 1.8 nm.

Secondly, the transient response of vertical short-channel OECTs is investigated with the variation of channel area, channel thickness, channel length and gate channel distance. Channel area and thickness are two main factors that influence the OECT response time. With a small channel area and thinner channel thickness, the transient response of PEDOT:PSS -based OECT below 1 μs is achieved for the first time. The n-type OECT can also realize a record fast response of 0.32 ms. Using fast response and high transconductance OECTs, electrocardiogram (ECG) and electrooculogram (EOG) recording on human subjects are demonstrated. A complementary inverter based on p-type and n-type OECTs is established with a record high gain (456 V/V), which is attributed to the small subthreshold slope of both devices.

Thirdly, biosensors based on OECTs are fabricated for the detection of COVID-19 IgG. OECT enables the detection of antibodies by converting charged biological signals into electrical signals. By adjusting the concentration and pH value of the test electrolyte, the COVID-19 IgG biosensor can realize a detection limit of 1 fM in PBS samples, and 10 fM in saliva and serum samples. The IgG detectable region is from 10 fM to 100 nM in serum and saliva, which can cover those SARS-CoV-2 IgG levels of COVID-19 patients. By adding a voltage pulse during the antibody incubation process, the reaction time can be reduced to only 5 minutes. A portable meter is designed and constructed to conduct wireless detections, which can be operated by mobile phone through Bluetooth.

In summary, the simple solution-gated device structure, miniaturized device size and low working voltages of OECT devices will lead to broad potential applications in bioelectronics. The study of new device structures can not only obtain high-performance organic transistors, but also promote the transistor scaling down to the next generation.

List of publications

(1) **Liu H.**; Yang A.; Song J.; Wang N.; Lam P.; Li Y.; Law H. K.-w.; Yan F. Ultrafast, Sensitive, and Portable Detection of COVID-19 IgG Using Flexible Organic Electrochemical Transistors. *Sci. Adv*. **2021**, 7, eabg8387.

(2) **Liu H.**; Yan F. Sub-1 Nanometer Short-channel Vertical Organic Transistor. (*In preparation*.)

(3) **Liu H.**; Yan F. Fast Response Short-channel OECTs and Its Application in Electrophysiology Recording and Inverters. (*In preparation*.)

(4) Song J.; **Liu H.**; Zhao Z.; Guo X.; Liu C.; Griggs S.; Marks A.; Zhu Y.; Law H. K.-w.; McCulloch I.; Yan F. 2D Metal-organic Frameworks for Ultraflexible Electrochemical Transistors with High Transconductance and Fast Response Speeds. *Sci. Adv.* **2023**, 9, eadd9627.

(5) Song J†.; **Liu H.** †; Zhao Z. †; Lin P.; Yan F. Flexible Organic Transistors for Biosensing: Devices and Applications. *Adv. Mater.* **2023**.

(6) Song J.; Tang G.; Cao J.; **Liu H.**; Zhao Z.; Griggs S.; Yang A.; Wang N.; Cheng H.; Liu C.; McCulloch I.; Yan F. Perovskite Solar Cell-Gated Organic Electrochemical Transistors for Flexible Photodetectors with Ultrahigh Sensitivity and Fast Response. *Adv. Mater.* **2023**, 35, 2207763.

(7) Yang A.; Song J.; **Liu H.**; Zhao Z.; Li L.; Yan F. Wearable Organic Electrochemical Transistor Array for Skin-Surface Electrocardiogram Mapping Above a Human Heart. *Adv. Funct. Mater.* **2023**, 2215037.

(8) Song, J.†; Zheng, J.†; Yang, A.; **Liu, H.**; Zhao, Z.; Wang, N.; Yan, F. Metal–Organic Framework Transistors for Dopamine Sensing. *Mater. Chem. Front.* **2021**, 5, 3422.

(9) Fu Y.; Wang N.; Yang A.; Xu Z.; Zhang W.; **Liu, H.**; Law H. K.-w.; Yan F. Ultrasensitive Detection of Ribonucleic Acid Biomarkers Using Portable Sensing Platforms Based on Organic Electrochemical Transistors. *Anal. Chem.* **2021**, 93,

43, 14359–14364.

Acknowledgements

This thesis represents my research works as a Ph.D. student in the Applied Physics Department of Hong Kong Polytechnic University, in Prof. YAN Feng's group from September 2019 to August 2022. I could not complete these studies without the help of many people.

I would like to express my sincere gratitude to my supervisor, Prof. YAN Feng, for his support of my study over the past three years. Prof. Yan is a highly knowledgeable and experienced authority in the fields of transistors and biosensing. He is unfailingly dedicated to academic research and closely follows and guides the progress of every student's research. Prof. Yan is not only intelligent and diligent but also approachable, always willing to address any queries I have and help me overcome scientific challenges. He adeptly generates innovative ideas and effectively directs me towards critical problem-solving strategies. Thanks to Prof. Yan's guidance in research planning, along with his teaching of data organization and scientific paper writing, I have avoided unnecessary detours and acquired invaluable knowledge on scientific research methodologies. Once again, I would like to express my heartfelt appreciation towards him.

Next, I would like to thank the support staff of Applied Physics Department and the technical staff of UMF. Ms. HO Wing Man, Dr. WONG Hon Fai, and Mr. CHAN Tsz Lam support a lot in laboratory safety management, equipment management, chemicals ordering, and instruments training. Dr. Terence WONG, Ms. Joyce LAU, Dr. Hardy LUI, and Ms. Pendy HO support a lot in instruments training and management in Cleanroom and Materials Research Centre. Especially Terence, he is always the first to help solve problems and provide advice. Ms. Cecilia CHAN, Ms. Tiffany WONG, Ms. Meijei WONG, Ms. Yonnie CHEUNG, Ms. Titus AU, Ms. Debbie LEUNG, Ms. Vivian

WONG, Mr. LO Chi Sang, and Mr. LAM Kwan Ho offer helps in information technology assistance and administrative management. Their supports allow me to have more time to focus on my study.

Next, I would like to thank my colleges in AP department. Special thanks to Dr. SONG Jiajun, Dr. YANG Anneng, Dr. WANG Naixiang, for teaching me a lot in device fabrication and further characterizations. Mr. ZHAO Zeyu, Mr. TIAN Zhiyuan, Mr. ZHAO Sanqing, Mr. WANG Ziru, Dr. TANG Guanqi, Dr. WANG Tianyue, Dr. CAO Jiupeng, Mr. CHENG Haiyang, Mr. Liu Chunki, Mr. Loi Hok-Leung, Dr. LIU Pei, Dr. FENG Guitao, Dr. ZHANG jing, Dr. XIAO Mingchao, Dr. LIU Dapeng, Ms. DENG Wenqiu, Dr. Venkatesh Piradi, Ms. LI Yuenling, and Mr. LAM Puiyiu, Dr. LING Haifeng, Dr. TANG Wei, they help me a lot in the lab and offer me many valuable suggestions. In the past three years, I spent most of my time with these friends in and outside of the lab. I cherish the moments we spent conducting experiments together, dining together, and climbing mountains together. Their company has made my research life all the more enjoyable.

Next, I would like to thank Prof. Helen LAW from the Department of Health Technology and Informatics who help me prepare biological samples. Thank Prof. Iain McCulloch, and his group members, who provided me with the semiconducting polymers used in part of my research in this thesis.

I am grateful to Prof. LIN Peng for directing me towards pursuing my studies in Hong Kong. Hong Kong, a metropolis located in southern China, exposed me to an array of scenic mountains and enchanting seas, along with diverse cultural customs.

I extend my appreciation to my friends and roommates, Vicky and Jennifer, for sharing countless moments of enjoyable conversation and shared meals in our apartment.

Last but not least, I would like to express my deepest gratitude to my parents, sister, and family members who have bestowed upon me the utmost love and selflessness. My parents' compassionate, diligent, and sagacious words and deeds have substantially shaped me, enabling me to become a better version of myself.

Table of contents

List of figures

Figure ***Captions*** ***Page***

Chapter 1 Introduction

1.1 Background

Organic electronic materials have been widely applied in light-emitting diodes,[1] thin-film transistors,[2] solar cells,[3] and bioelectronics[4] for their good electrical performance, flexibility, stretchability, and large-area low-cost processing techniques. The development of organic electronics in biological applications attract massive attention in recent decades.[5,6] In this chapter, The applications of organic electronics in the field of biomedicine are introduced. Organic bioelectronics can selectively detect, monitor, and record biological signals and physiological states, and convert relevant parameters into electrical data. According to different functions, the applications can be divided into neural interfaces, electronic skin, biofuel cells, biosensors, and electrophysiology monitoring (Figure 1.1).

(1) Neural interfaces

The neural interface, also known as a brain-computer interface (BCI), enables the connection of human or animal brains to external devices. With their good conductivity or semiconductor properties as well as biocompatibility, flexibility, and stretchability, organic materials are highly suitable for providing interfaces between living systems and electronic devices, and for realizing the integration between nervous systems and computers.[7,8] Brain-computer integration encompasses invasive and non-invasive approaches that correspond to brain connection in vivo and in vitro. Microelectrodes attached to the cerebral cortex need to be small enough to provide sufficient resolution while also being flexible and having small contact resistance.[9] Conductive polymers like polypyrrole (PPy) and poly(3,4-ethylenedioxythiophene) (PEDOT) possess outstanding electrical properties, which allow them to create interfaces with high charge capacity and low impedance.[10] In the future, it may be possible to break through traditional neural reflex arc limitations with a neural interface. Connecting brain neural signals directly with computers could allow for direct control and communication with external electronic equipment.

(2) Electronic skin

The development of electronic skin benefits from advances in organic materials, which are usually morphologically plastic. High mechanical performance is essential to withstand continuous and repeated stretching and bending. Polymer molecular designs can be tailored to meet different types of applications, while surface modification techniques can improve the biocompatibility and stability of organic films.[11,12] Flexible substrates such as polyethylene terephthalate (PET), polyethylene naphthalate (PEN), parylene, and polydimethylsiloxane (PDMS) are commonly used.[13] In addition, electronic skin needs to have sensing functions such as temperature sensors, humidity sensors, and pressure sensors, as well as the skin protection functions.[14,15] The sensitivity of the sensors determines whether weak signal variations can be captured, and the density of the sensor determines the spatial resolution. It is worth noting that the complete realization of electronic skin also requires the transmission of detected signals to the sensory organs and nervous system.[16]

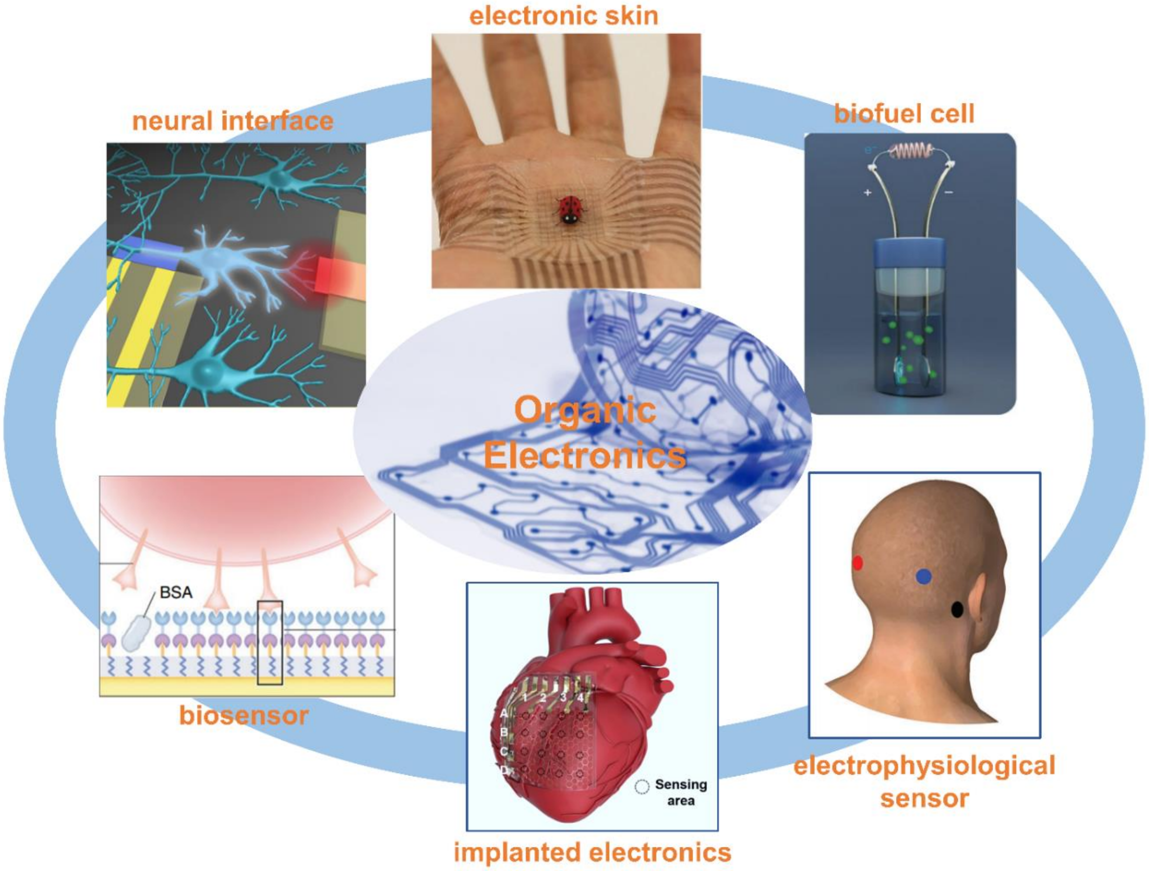

Figure 1.1 Organic bioelectronic devices have a wide range of potential applications, including neural interface, electronic skin, biofuel cell, biosensors, and electrophysiology monitoring.[17-22]

(3) Biofuel cell

Electronic equipment is reliant on energy support for its operations. This energy can be supplied through either portable commercial flexible batteries or energy harvesting systems such as triboelectric generators, biofuel cells, and solar cells. Furthermore, enzymes can be utilized to convert metabolites (such as lactic acid, glucose, uric acid) found in body fluids like urine, sweat, and saliva into electrical energy, resulting in sustainable energy generation under mild conditions.[23] With greater collaboration between the energy management circuit, a fully integrated self-powered sensing system can be designed, making it possible to drive wearable biosensors and enable real-time health monitoring.[24] Despite extensive research on biofuel cell systems, generating enough energy from body fluids to support long-term health monitoring remains a challenge.

(4) Biosensors

Biosensors can convert biological signals into readable electrical signals, allowing them to perform qualitative and quantitative analyses of biomolecules.[25] Generally, label-free specific bioassays comprise of two steps: immobilization of the bio probe and specific binding with the analyte.[26] This could include the hybridization of nucleic acids, the reaction between enzymes and metabolites, or the binding of antigens and antibodies. The variation in electrical signals (such as voltage, current, capacitance) can be used to obtain vital biomolecular information like species, concentration, amount, and state. Compared to electrochemical analysis, transistor-based biosensors can amplify electrical signals in situ and exhibit greater sensitivity. Currently, organic thin-film transistors have realized the detection of single molecule.[27] Biosensors can be combined with wearable electronics to real-time monitor the level of metabolites such as glucose, lactate, and uric acid.[28]

(5) Electrophysiology monitoring

Unlike biosensors that test biomolecules, electrophysiological sensing directly measures weak electrical signals produced by the human body.[29] These signals, known as action potentials, are generated when muscle or brain cells are stimulated, and they can be transmitted to the skin surface from multiple cells.[30] Physiological signal testing can be done either in vivo or in vitro. In vivo detection provides more sensitive signals with larger signal-to-noise ratios. Electrophysiological signals mainly include electrocardiogram (ECG), electroencephalogram (EEG), electrocorticography (ECoG), electromyogram (EMG), and electrooculography (EOG).[31] ECG signals, generated by heart muscle cells, can be used to detect abnormal heart rhythm and myocardial infarction. EEG signals, on the other hand, are weaker than ECG signals and can be used to detect epilepsy and sleep disturbances.

The application of organic electronics in biological systems can help us understand the mechanisms of life activities, study neural networks, and monitor physiological conditions. This technology serves not only as an aid to modern medical care but also as an important component in the future growth of intelligent robots and brain-computer integration.

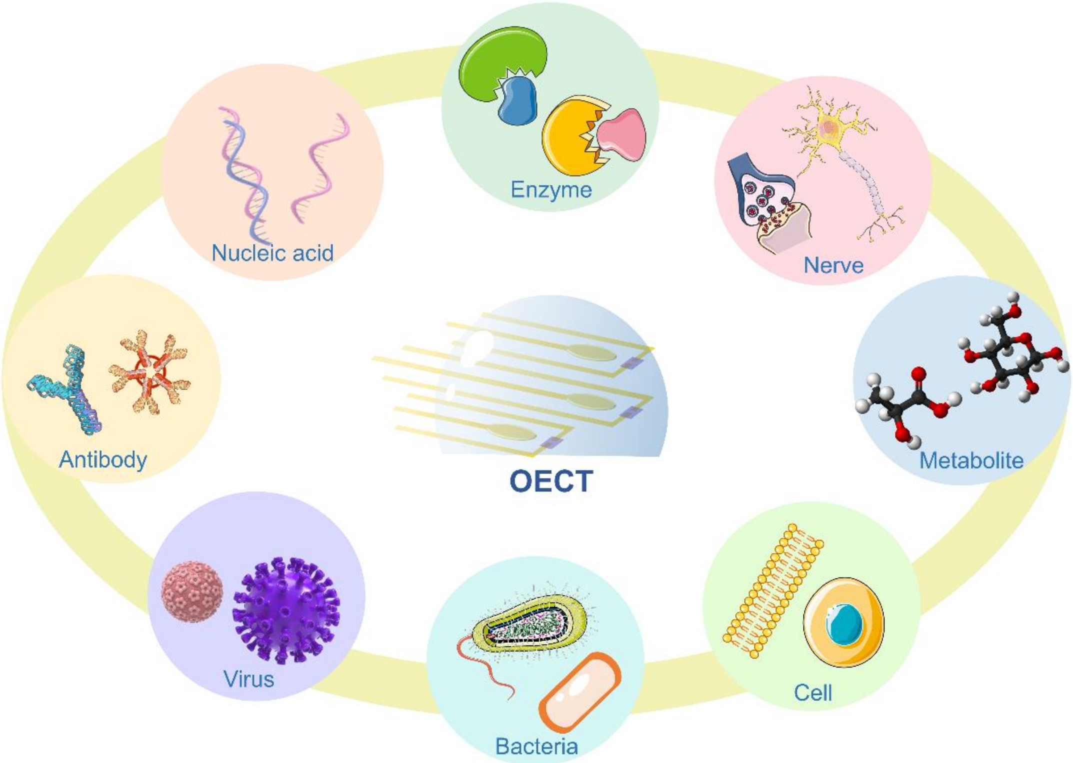

Figure 1.2 OECTs can be applied in the detection of nucleic acids, proteins, metabolites, cells, etc. (Figures of nerve, cell, bacteria, virus are free from Servier Medical Art; https://smart.servier.com/)

Organic bioelectronics, relies heavily on transistors as a fundamental component in building intelligent electronic circuits, which can capture, amplify, filter, convert, and transmit biological and physiological signals.[32] Organic thin film transistors (OTFTs) can well meet the requirements of flexible devices and better biocompatibility,[2] which not only exist high electrical performances of high transconductance and fast response, but also show high flexibility for practical applications. OTFTs can be divided into organic field effect transistors (OFET) and organic electrochemical transistors (OECT) according to different working principles.[2] The distinguishing factor between OECT and OFET lies in the ion doping/dedoping capability of the channel materials.[33] More detailed explanations of the various structure categories and device principles will be provided in the following chapter.

Since the channel material is ion permeable, the electronic and ionic charges couple within the whole volume of the channel, enabling OECT to have high transconductance. In addition, OECT can maintain good stability in solution or solid electrolyte. The liquid environment is also very suitable for bio detection.[34] OECTs are therefore widely used in diverse applications such as biosensors, electrophysiology recording, memory devices, and neuromorphic devices. Additionally, OECTs show great potential in biofuel cells and wearable detection systems.[19,35] OECT biosensors include the detection of human metabolites, proteins, cells, bacteria, viruses, nucleic acids, and other biomolecules (as shown in Figure 1.2). The following chapter of the literature review will introduce the working principle of OECTs, channel materials, biosensing strategies, and applications in biosensors and electrophysiology recording.

1.2 Objectives of research

Organic electrochemical transistors and their biosensing applications are very promising. However, the generation of high-performance OECTs (i.e., high transconductance, fast response, and stability) is crucial for their further development and wider range of applications. Presently, efforts to improve OECT device performance are primarily focused on the development of channel materials, while research on novel device structures is limited. It is important to note that high transconductance and fast response characteristics are not only dependent on the choice of channel material but are also influenced by device structures. Increasing the channel volume can improve transconductance, but it comes at the expense of transient response. A more effective solution is to shorten the channel length of transistors, which improves both transconductance and transient response parameters. Currently available lithography-based fabrication technologies make it challenging to achieve a planar resolution lower than 50 nm. In addition, the short-channel effect presents a significant obstacle to improving electrical performance as channel length is reduced. Addressing this challenge is an urgent priority.

The research objectives include the following points. (1) Prepare vertical short-channel OECTs to investigate the minimum achievable channel length and identify the channel length required to overcome the short-channel effect. Achieve high-performance OECTs with high transconductance, high on-off current ratio, and low subthreshold slope. Test transistor performance using different channel materials, including n-type and p-type polymers. (2) Investigate the transient response of short-channel OECTs and analyze related influencing factors. Use high-performance vertical short-channel OECTs to detect electrophysiology signals (ECG and EOG). Prepare a complementary inverter based on p-type and n-type short-channel OECTs to realize high gain, fast response, and low energy consumption. (3) For the current COVID-19 epidemic, to realize high-sensitive, fast, and portable detection of COVID-19 antibodies. Investigate methods to improve the sensitivity of biological detection.

1.3 Outline of thesis

The organization of the thesis is as follows:

Chapter 1: Introduction. This chapter provides a brief introduction to the application of bioelectronic devices in different research fields, and the application of OECTs in biosensing.

Chapter 2: Literature review. In this chapter, the working principles of OECTs and their differences from field effect transistors are introduced in detail. Three key performance parameters of OECTs and various channel materials used OECTs are summarized. The applications of OECTs in biosensors and electrophysiology recording are introduced.

Chapter 3: Short-channel vertical organic electrochemical transistor. A short-channel vertical organic electrochemical transistor (OECT) was developed using Al_2O_3 as the electrode spacer. By utilizing solution-gating, the OECT was able to weaken the short-channel effect and achieve a sub-1nm channel length of 0.86 nm with an over 400 on-off current ratio. Both p-type and n-type short-channel OECTs demonstrated over 10^6 on-off current ratios and an ideal subthreshold slope of 60 mV/dec. The stable short-channel OECTs were found to exhibit over 3960 S/m of width-normalized transconductance.

Chapter 4. Fast response short-channel OECTs and their application in electrophysiology recording and inverters. In this chapter, the transient response of short-channel OECTs and related influencing factors are investigated. Fast response (below 1 μs) OECTs are applied in ECG and EOG recording. A complementary inverter based on p-type and n-type OECTs is fabricated which show record high gain of 456 V/V and low power consumption.

Chapter 5: Ultrafast, sensitive, and portable detection of COVID-19 IgG using flexible OECTs. In this chapter, a COVID-19 antibody biosensor based on OECT was fabricated. The biosensor operated by a portable meter can realize the detection of COVID-19 IgG with 1 fM detection limit in PBS samples and 10 fM in saliva and serum samples. The antigen antibody incubation time can be reduced to 5 minutes under a voltage pulse.

Chapter 6: Conclusions and perspectives. In this chapter, the high electrical performances of vertical short-channel OECTs and their transient response characteristics are summarized. The COVID-19 antibody detection based on OECTs is discussed. The perspectives of related works mainly focus on further studying the device operation mechanisms of short-channel OECTs and exploring more mature bio applications.

Chapter 2 Literature review

2.1 Introduction

Over the past 40 years, OECTs have undergone significant advancements in channel materials, device structures, and device performance, making them a diverse and remarkable technology that is capable of meeting the requirements for building integrated circuits and biosensing platforms.[36] This chapter begins by describing the device physics of OECTs, including a discussion of the three key parameters (transconductance, response time, and subthreshold slope) and their relationship with device geometric dimensions. A summary of the most commonly used p-type and n-type materials is provided to help readers better understand the relationship between material properties and device performance. The chapter then introduces OECT biosensing strategies and different types of biosensors, which can serve as a useful reference for establishing biosensors. Finally, the chapter reviews the use of OECTs for in vivo and in vitro electrophysiological sensing.

2.2 OECT operation mechanisms

2.2.1 Device physics

In a typical organic electrochemical transistor (Figure 2.1a), there are three electrodes (source, drain, and gate), an organic semiconductor channel, and the electrolyte (solution, gel, solid) connecting the gate and channel.[37] In a field effect transistor, when a gate voltage is applied, the electric field induces electric carries in the channel through electric dipole in the dielectric layer (Figure 2.1b). Since the deflection of the electric dipole needs a strong electric field, the gate modulation is laborious, usually requiring tens of volts gate voltage.[38] In a solution-gated structure (include electrolyte-gated OFET and OECT), when gate voltage applied, two electrical double layer (EDL) formed at the gate/electrolyte and channel/electrolyte interface.[39] The length of EDL is usually no more than tens of nanometers, enabling two interface have large capacitance. Transistors with solution-gated structure can be operated at low gate voltage (below 1 voltage). OECT channel are ion-permeable conductive polymer, in which ions can inject into the whole polymer when gate voltage applied.[33] The higher volume capacitance of OECT results in larger transconductance.

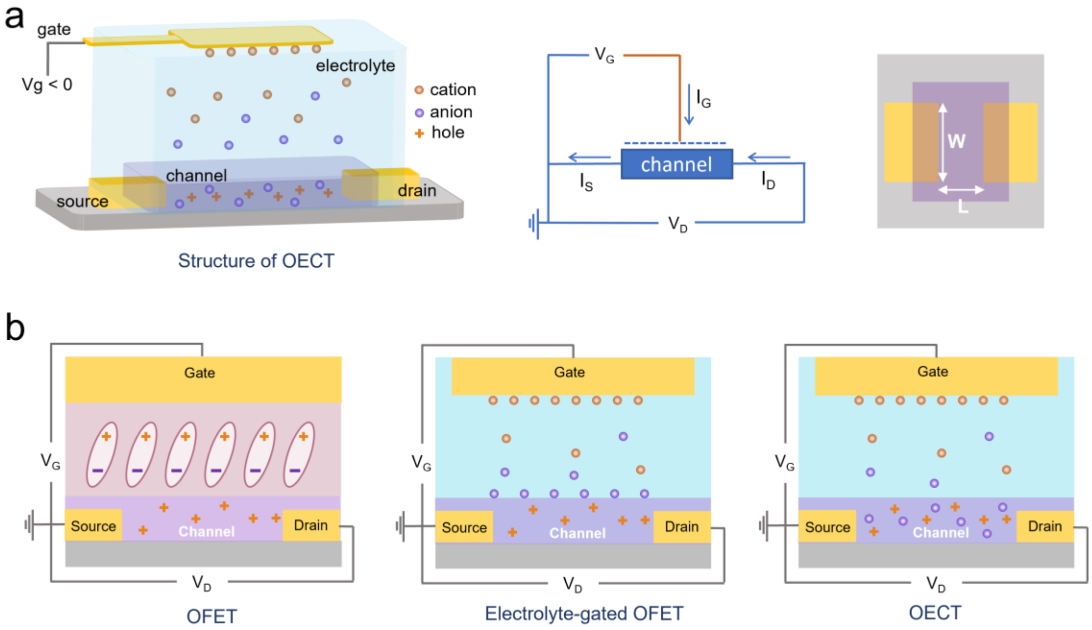

Figure 2.1 (a) The typical device structure and circuit diagram of OECT. (b) Diagrams of different operation mechanisms between OFET (e.g., top gate bottom contact), electrolyte-gated OFET, and OECT.

2.2.2 Performance parameters

(1) Transconductance

High transconductance is a significant characteristic of OECT devices, as it represents the current amplification capability of the transistor. Transconductance is defined as the magnitude of the change in channel current per unit change in gate voltage, and is an important factor in determining device performance.[40] For an OECT, the transconductance at the saturation region is expressed as[37]:

$$g_m = \frac{W}{L}\mu d C^*(V_{TH} - V_{GS}) \ , \qquad (1.1)$$

where W is channel width, L is channel length, d is channel thickness, μ is the electronic carrier mobility, and C* is the capacitance of the channel per unit volume, V_{th} is the threshold voltage. The Wd/L value in this function is determined by the geometric dimensions of the device. The μC* represents a material-system-dependent product that determines the geometric normalized transconductance. Having a high transconductance is essential for achieving a large current gain in OECT-based circuits and sensors. In OECTs with high transconductance, small variations in gate voltage can induce significant channel currents, which can enhance the sensitivity of chemical and biological sensors.[41]

According to Equation 1.1, transconductance is positively correlated to both Wd/L and μC*.[42] A large Wd/L value means a small channel resistance, whereas a high μC* value indicates a high charge storage capacity. Organic semiconductor with high μC* level will be discussed in detail later in materials section. In addition to the factors dominated by channel characteristics, transconductance is also influenced by the nature of the gate and electrolyte.[43] In ionic circuit, except using the nonpolarizable gate electrode (such as Ag/AgCl), higher gate capacitance can be realized by larger gate area or thick PEDOT:PSS film.[44] The nature of electrolyte (liquid, gel or solid), ion concentration, and ionic radius determine the migration rate of ions in solutions and conjugated polymer.[45] For bio application, solutions close to physiological fluid such as 0.1 M NaCl and 1X PBS are usually chosen as the electrolyte.

The most studied high transconductance OECTs are PEDOT:PSS based, which have a high μC* value. By adjusting the channel geometric dimensions (channel length 150 nm, channel thickness 50 μm), the g_m can be increased to 63.45 mS.[46] Internal ion gated OECT exhibit high volumetric capacitance, resulting in a large transconductance (52.74 mS).[47] P-type accumulation material p(g2T-TT) has the top-performance μC* level, and the g_m value can reach 50 mS with an ordinary flat device structure.[21] The normalized

g_m and the μC* level of p-type and n-type materials are shown in Figure 2.2.

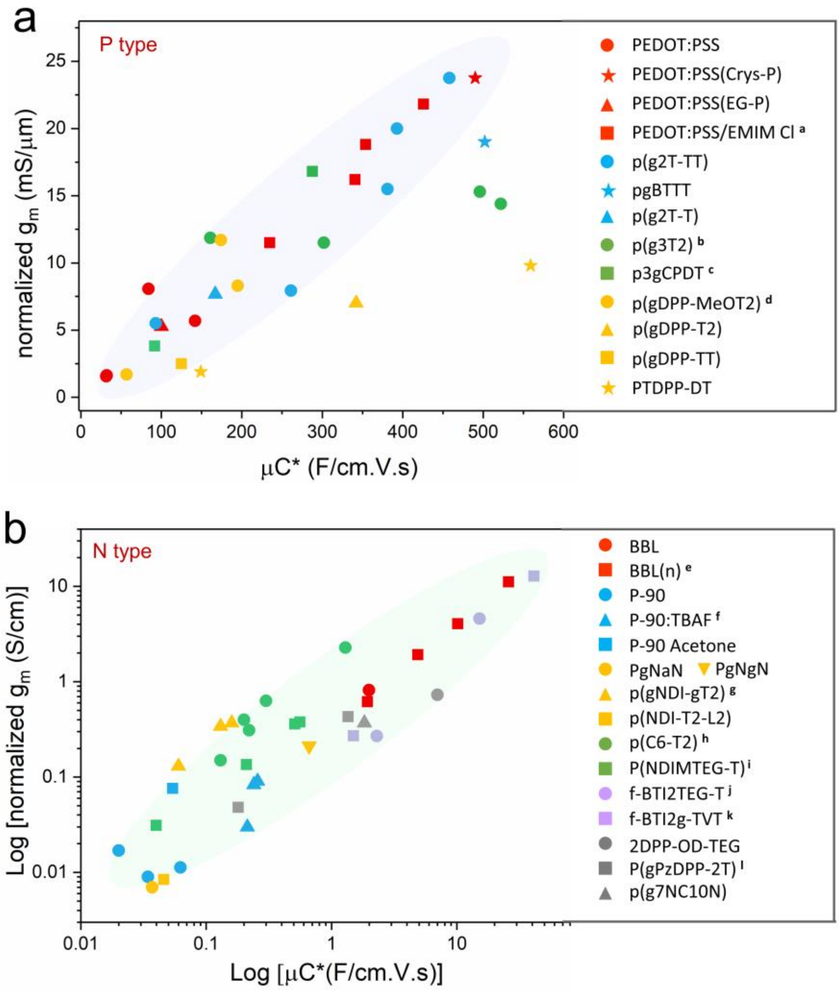

Figure 2.2 The normalized transconductance and μC* level of (a) p-type OECTs and (b) n-type OECTs. **a** includes PEDOT:PSS/EMIM Cl, PEDOT:PSS/EMIM OTF, PEDOT:PSS/EMIM TFSI, and PEDOT:PSS/EMIM TCM. **b** includes p(g3T2), p(g2T2-g4T2), p(g1T2-g5T2), p(g0T2-g6T2). **c** includes P3gCPDT-2gT2 and P3gCPDT-1gT2. **d** includes p(gDPP-MeOT2), p(lgDPP-MeOT2), and p(bgDPP-MeOT2). **e** includes BBL_{15}, BBL_{60}, BBL_{98}, and BBL_{152}. **f** includes P-90:TBAF(10%), P-90:TBAF(40%), and P-90:TBAF(80%). **g** includes p(gNDI-gT2), p(C3-gNDI-gT2), and p(C6-gNDI-gT2). **h** includes p(C4-T2-C0-EG), p(C2-T2), p(C4-T2), p(C6-T2), p(C8-T2). **i** includes P(NDITEG-T), P(NDIDTEG-T), P(NDIDEG-T), P(NDIMTEG-T). **j** includes f-BTI2TEG-T and f-BTI2TEG-FT. **k** includes f-BTI2g-TVT and f-BTI2g-TVTCN. **l** includes P(gPzDPP-2T) and P(gPzDPP-CT2). (Specific references can be found in Table 2.1 and Table 2.2)

(2) Transient response

Transient response is another important parameter attention-getting, especially in OECT based circuits, neuron detection,[48] and electrophysiological measurements[49]. The response time is related to both the ionic and the electronic circuit, and usually dominated by the ionic circuit due to the slow migration rate of the ions. Early in 2007, Bernards et al. present a simplified model to express the transient characteristics of OECTs.[37] Limited by the ionic circuit, OECT response time τ is dictated by the product of the resistance of the electrolyte R_S and the capacitance of the channel C_{CH}. The channel capacitance is scaled with organic semiconductor channel volume (WdL), which represent the charge capacity brought by whole volume ion injection. On the other hand, the electrolyte R_S is scaled with channel area $1/(WL)^{1/2}$, resulting that the transient response τ is scaled with $d(WL)^{1/2}$.[50,51] In terms of the channel geometry, a smaller channel volume, particularly the thickness, can lead to a faster transient response. In addition, the response time can also be shortened by adjusting the electrolyte concentration[52], electrolyte ion species[53], and gate electrodes[43]. Moreover, according to the research of Friedlein et al.,[54] the response time can be significantly reduced by adjusting the gate voltage to balance the channel current and the gate current, but the practical using of this method is limited by fixed gate voltage.

The transient response of p-type and n-type OECT devices are summarized in Table 2.1 and Table 2.2 respectively. Overall, p-type OECTs, especially PEDOT:PSS devices, respond faster than n-type devices. The transient response of n-type devices is limited by lower electron mobility and ion migration speed. The top-performance PEDOT:PSS based device can reach fast response as less as 2.6 μs with internal ion gated device structure.[55] The fast transient response promoted the development of integrated circuits and kinds of electrophysiological testing.[47,55] Through increasing the molecular weight, long chain BBL_{152} outstand in n-type materials with a record fast response 0.38 ms.[56]

(3) Subthreshold slope

Subthreshold slope (SS) is a parameter measuring the switch rate between transistor on and off states, representing the gate voltage variation when channel current change one decade. Low SS is helpful in improving power efficiency and decreasing energy consumption. The subthreshold region of operation in MOSFETs has been of considerable interest. However, it hasn’t addressed lots of attention in the OECT field. Giovannitti et al. were the first to report OECT with an ideal SS of 60 mV/dec, which was realized by p-type conjugated polymer p(g2T-TT).[21] Because p(g2T-TT) based OECTs are hole transporting with accumulation mode, the subthreshold region occurs at a low gate voltage offset, in which the gate current is small. Low SS is easier to be realized with less influence of leakage gate current. In addition, large channel geometric dimensions Wd/L can also promote lower SS.[21] PEDOT:PSS based OECTs are operated in the depletion model, which are theoretically get higher subthreshold slope for higher gate current in the subthreshold region. In 2022, Weissbach et al. reported PEDOT:PSS based OECTs with a subthreshold swing of 61 mV dec^{-1}.[57] A general approach of photo patternable solid electrolytes was introduced in this work, bringing a sufficiently low gate current in subthreshold region. Small subthreshold slope OECTs have high voltage gains and lower power consumption, which is significant in integrated circuits and physiological signal detection.

2.2.3 Channel materials

As discussed above, the channel materials play a key role in device performances, regulating the device's transconductance, transient response speed, subthreshold slope, and stability. The character of OECT channel material is ion permeable, which usually include a backbone for electronic charge transport, and the ionic transport can be allowed through the bulk. Depending on the type of charges, the channel materials were divided into p-type (hole transport) polymer and n-type (electron transport) polymer. The physic performances of different channel materials OECTs are concluded in Table 2.1 and Table 2.2.

(1) P-type material

According to the molecular structure and composition, the p-type channel materials are mainly divided into 3 classes: (1) Conducting polymer composite with doped polyelectrolyte or small molecules; (2) Conjugated polyelectrolytes; (3) Semiconducting polymer. The most commonly used PEDOT:PSS is conducting polymer poly(3,4-ethylenedioxythiophene) (PEDOT) doped with poly(styrene sulfonate) (PSS) polyelectrolyte, in which the holes on the PEDOT are compensated by acceptors (SO_3^-) on the PSS. Except PSS, anionic polyelectrolyte dopants such as (trifluoromethylsulfonyl)sulfonylimide (TFSI)[58] and tosylate (TOS)[59] were also studied. For conjugated polyelectrolytes (such as PEDOTS[60], PTHS[61]), their conjugated carbon backbone and pendant ionic side chains allow the mixed ionic–electronic transport. For example, self-doped polyelectrolyte PEDOTS consist with a PEDOT backbone and covalently bonded aliphatic side chains with sulfonate functional groups. Semiconducting polymers are ion-free neutral polymers, which have alkoxy or ethylene glycol side chains. The hydrophilic glycol side chains can significantly enhance the volume capacitance. Types of semiconducting conjugated polymers are abundant, such as P3HT, g2T-T, p(g2T-TT), gBDT-g2T, polypyrrole, polyaniline, et al. Next, the two top performance p-type materials PEDOT:PSS and p(g2T-TT) will be introduced in detail.

The most well-studied OECTs are PEDOT:PSS based, which are charactered with high channel current, high μC* value, high transconductance, fast response, high stability, and easy for fabrication. The typical PEDOT:PSS exhibits a μC* value around 50 F cm^{-1} V^{-1} s^{-1}, and a Wd/L normalized transconductance around 8 S mm^{-1}.[51] Through the nano scale short-channel[46] or extremely high Wd/L channel size[62], the transconductance can reach as high as 63.45 mS and 180 mS respectively. Spyropoulos et al. were the first reported the internal ion-gated OECT device structure. In their device structure, the mobile ions embedded in the channel PEDOT:PSS, creating a self-(de)doping process with no needs of external electrolyte. Finally, the transconductance can reach 52.74 mS, and the response time was shortened to 2.9 μs.[47,55] In addition, through processing like crystallizing[63], or adding additive, the conductance and μC* level can be significant enhanced.[53,62,63] Ethylene glycol (EG) is additive that can improve electronic conductivity of polymer films, and increase the μC* level to 100 F cm^{-1} V^{-1} s^{-1}. Through using ionic liquids as additives, for example, the 1-Ethyl-3-methylimidazolium (EMIM) as cation, and the trifluoromethanesulfonate (OTF) or tricyanomethanide (TCM) as anion, the μC* level can be increased to 426 F cm^{-1} V^{-1} s^{-1}.[53] By introducing ionic liquid 1-ethyl-3-methylimidazolium chloride [EMIM][PF6] and dodecylbenzenesulfonate (DBSA) into PEDOT:PSS, the μC* can be improve to 490 F cm^{-1} V^{-1} s^{-1}, [62] which is comparable to crystallized PEDOT:PSS. [63]

It is obviously that PEDOT:PSS have many advantages among kinds of channel materials. However, it is operated in depletion mode, which is relativity energy consuming. In 2016, Giovannitti et al. introduced a semiconducting polymer poly(2-(3,3′-bis(2-(2-(2-methoxyethoxy)ethoxy)ethoxy) [2,2’-bithiophen]-5-yl)thieno[3,2-b]thiophene) (p(g2T-TT)), which outpacing the PEDOT-based OECTs of the same geometry. There are glycol side chains on the thiophene backbone of p(g2T-TT), which can promote the penetration and transport of ions in electrolyte and enable a large modulation in capacitance. The accumulation mode p(g2T-TT) OECTs can perform quite stable without additives or cross-linkers. Cendra et al. studied the performances of p(g2T-TT) OECTs with different kinds of anions in electrolyte. Anions with a larger crystallographic radius can increase the transconductance but also delay the transient response. The μC* value of p(g2T-TT) OECTs in different electrolyte varies from 268 F cm^{-1} V^{-1} s^{-1} to 458 F cm^{-1} V^{-1} s^{-1}.

In addition to the two top performance PEDOT:PSS and p(g2T-TT), efforts are made to synthesis p-type channel materials with even higher μC* value. McCulloch group and other researchers introduced the semiconducting polymers pgBTTT with a μC* value of 502 F cm^{-1} V^{-1} s^{-1}, [64] the p(g2T2-g4T2) with a μC* value of 522 F cm^{-1} V^{-1} s^{-1}, [65] P3gCPDT-MeOT2 with a μC* value of 448 F cm^{-1} V^{-1} s^{-1}, [66] and the PTDPP–DT with a μC* value of 559 F cm^{-1} V^{-1} s^{-1}. [67] The side chains of these high-performance semiconducting polymers are glycolated, enabling high volume capacitance.

(2) N-type materials

Limited by low carrier mobility, the performance of n-type OECTs is lagging far behind that of p-type OECTs. The delayed development of n-type organic mixed ionic-electronic conductors is mainly due to unstable electron transport caused by reactions between the n-type material and water or oxygen.[68] The LUMO level of this n-type materials should be deep enough for efficient electron injection. N-type materials are indispensable for building the OECT-based integrated circuit, such as the complementary logic circuits. Although the study of n-type OECTs is no more than ten years, the development is quick and effective in recent years.[69]

The first reported n-type OECT channel material is p(gNDI-gT2), which can be stably operated in water.[69] The p(gNDI-gT2) is composited with a naphthalenediimide (NDI) backbone and long linear ethylene glycol-based side chains. The EG side chains enable the interacting with hydrated ions and water, which facilitate the ionic transport and result high volume capacitance (397 F cm^{-3}). The NDI derivatives (donor–acceptor) n-type polymer make up the majority of current n-type materials. The ratio of the backbone and EG side chains was studied, resulting the best performance ratio of 90%, namely P-90. [70] Additives like acetone (15%) and TBAF (40%) were found can enhance the channel capacitance and mobility. [71,72] Ohayon et al. found that the distance of the EG from the backbone affects the film order, crystallinity and the electron mobility.[73] Through the side-chain engineering, the first NDI-based polymer that own μC* level over 1 F cm^{-1} V^{-1} s^{-1} (1.29 F cm^{-1} V^{-1} s^{-1}) was synthesized, namely (p(C6-T2). Except the NDI-based polymer, the DPP-based, [74,75] fullerene-based, [76,77] and BTI-based[78,79] donor-acceptor type polymer can also receive relatively high μC* level. Specific information can be referred to Table 2. By balancing more charges to the donor moiety, the D-A n-type polymer P(gTDPP2FT) exhibits a record high μC* value of 54.8 F cm^{-1} V^{-1} s^{-1}, high mobility of 0.35 cm^2 V^{-1} s^{-1}, and fast response speed. [75]

Another class of n-type OECT channel material is the fully fused acceptor–acceptor derivatives, typically, poly(benzimidazobenzophenanthroline) (BBL). BBL is an old material that was not used in OECT until 2018, which exhibt a μC* value of 1.99 F cm^{-1} V^{-1} s^{-1}, and performed much better than many donor-acceptor type copolymer. [80,81] Wu et al. demonstrated that through increasing the molecular weight of ladder-type n-type polymer BBL, the μC* value can be obviously increased to 26 F cm^{-1} V^{-1} s^{-1}. [56] The longer polymer chains may act as the connection between crystalline regions. This high transconductance fast response long chain BBL performed also much better than other acceptor-acceptor type copolymer like PgNaN, [82] PgNgN, [82] gNR, [83] hgNR, [84] and p(g_7NC_{10}N) [85].

For bio detection, especially cell monitoring and in vivo detection, the channel material should be stable, non-toxic, no immune response, and favorable for cell attachment. While materials such as PEDOT:PSS have demonstrated their biocompatibility, there is still a need to explore and expand the variety of materials used in biosensor development.

Table 2.1. Summarization of p-type channel materials.

Channel materials p-type	Wd/L (μm)	gm (mS)	gm norm (mS μm^{-1})	μC* (F cm^{-1} V^{-1} s^{-1})	μ (cm^2 V^{-1} s^{-1})	C* (F cm^{-3})	τ on	(Year) Ref
PEDOT:PSS	0.4	4.02	10.05	NA	0.05	NA	NA	(2013) [41]
	0.2	1.6	8	NA	NA	NA	37 μs	
PEDOT:PSS	0.28	2	7.14	NA	NA	NA	NA	(2013)[42]
PEDOT:PSS	0.5	5	10	NA	1.9 ± 1.3	39.3 ± 1.3	320 μs	(2015) [44]
PEDOT:PSS	2	3.51	1.755	NA	NA	NA	49 μs	(2016) [58]
PEDOT: PSTFSILi100	2	3.41	1.705	NA	NA	NA	90 μs	
PEDOT:PSS (Crys-P)	0.8	19	23.75	490 ± 41	NA	113 ± 1.38	NA	(2018)[63]
PEDOT:PSS (EG-P)	0.76	4	5.26	100 ± 7	NA	31 ± 0.79	NA	
PEDOT:PSS	200	32.3	0.16	NA	NA	NA	NA	(2019)[55]
	NA	0.8	NA	NA	NA	NA	31.7 μs	
	NA	NA	NA	NA	NA	NA	2.6 μs	
PEDOT:PSS-PET	30	52.74	1.758	NA	NA	NA	NA	(2020) [47]
	0.1	1.5	15	NA	NA	NA	2.9 μs	
PEDOT:PSS	1.67×10^4	63.45	3.8×10^{-3}	NA	NA	NA	300 μs	(2020)[46]
PEDOT:PSS	1.6	12.9	8.06	84 ± 17	2.26 ± 0.45	37.3 ± 3.1	NA	(2020)[51]
PEDOT:PSS	16.1	139	8.6	NA	NA	NA	138 μs	(2021)[49]
PEDOT:PSS (144k-1.7)	2.284	16.1	7.05	142.4 ± 27.3	4	35 ± 4	NA	(2022)[86]
PEDOT:PSS/EMIM Cl	1.05	~12.5	11.5 ± 1.1	235 ± 39	NA	NA	NA	(2022)[53]
PEDOT:PSS/EMIM OTF	1.05	~19	18.8 ± 3.2	354 ± 60	3.55 ± 1.68	78 ± 7	14.4 μs	
PEDOT:PSS/EMIM TFSI	1.05	~16.5	16.2 ± 1.6	314 ± 43	NA	NA	NA	
PEDOT:PSS/EMIM TCM	1.05	~22	21.8± 3.7	426 ± 65	4.17 ± 2.35	89 ± 8	26.4 μs	
PEDOT:PSS/[EMIM][PF6]/DBSA	6	22.7	3.78	490	NA	12.8	NA	(2020)[62]

	32000	180	5.6×10^{-3}	490	NA	NA	NA	
p(g2T-TT)	3.4	27	7.94	261	0.95	240	NA	(2016)[87]
p(g2T-TT)	2	50	25	NA	NA	NA	NA	(2018)[21]
p(g2T-TT) electrolyte (NaSbF6)	0.8	~19	23.75	458 ± 57	~0.9	~340	NA	(2019)[45]
p(g2T-TT) EG side chain 75%	0.55	7.1	12.9	78.28	0.38	206	NA	(2020)[88]
p(g2T-TT) EG side chain 100%	0.55	18.8	34.1	163.3	0.55	297	116 µs	
p(g2T-TT) EG side chain 2g	0.55	1.3	2.36	16.1	0.07	231	166 µs	
p(g2T-TT)	1.11	6.2	5.5	93	0.41 ± 0.14	244 ± 51	NA	(2021)[64]
pgBTTT	1.08	21	19	502	3.44 ± 0.13	164 ± 7	NA	
gBDT-g2T	1.10	0.47	0.43	NA	NA	NA	NA	(2016)[89]
p(g2T-T)	1.03	7.9	7.67	NA	NA	NA	1.4 ms	
p(g3T2)	0.75	8.9	11.87	161	0.90 ± 0.10	156 ± 1	NA	(2020)[65]
p(g2T2-g4T2)	0.45	6.5	14.4	522	1.72 ± 0.31	187 ± 8	NA	
p(g1T2-g5T2)	0.65	10	15.3	496	2.61 ± 0.30	133 ± 3	NA	
p(g0T2-g6T2)	0.7	8.1	11.5	302	2.95 ± 0.37	74 ± 4	NA	
PTDPP–DT (Cl^-)	1.51	7.2	1.9 ± 1.7	149 ± 61	1.1 ± 0.5	123	NA	(2021)[67]
PTDPP–DT (BF_4^-)	1.51	21.4	9.8 ± 1.6	559 ± 65	2.5 ± 0.3	224	NA	
p(gDPP-TT)	1.23	3.1	2.5	125 ± 22	0.57 ± 0.09	184	NA	(2021)[90]
p(gDPP-T2)	0.9	6.3	7	342 ± 35	1.55 ± 0.17	196	NA	
p(gDPP-MeOT2)	0.82	1.4	1.7	57 ± 5	0.28 ± 0.04	169	NA	
P(gTDPPT)	0.6	1.18	NA	65.1	0.40	161 ± 15	0.46 ms	(2022)[75]
P(lgDPP-MeOT2)	0.6	7.04	11.7	174 ± 25	2.15 ± 0.27	80.8 ± 1.4	578 µs	(2021)[91]
P(bgDPP-MeOT2)	0.64	5.33	8.3	195 ±21	1.63 ± 0.14	120.0 ± 2.4	516 µs	
P3gCPDT-2gT2	0.57	2.4	3.83	92 ±2.3	0.66	140 ± 25	22.8 ms	(2022)[66]
P3gCPDT-1gT2	0.39	7.2	16.83	288.6 ± 5.5	0.90	320 ± 33	36.7 ms	

P3gCPDT-MeOT2	0.44	16	34.4	448.6 ± 27.8	3.10	145 ± 37	49.3ms	

Table 2.2 Summarization of n-type channel materials

Channel materials **N-type**	Wd/L (μm)	g_m (μS)	gm norm (S cm^{-1})	μC* (F cm^{-1} V^{-1} s^{-1})	μ (cm^2 V^{-1} s^{-1})	C* (F cm^{-3})	τ on	(Year) Ref
p(gNDI-gT2)	2	21.7	0.1085	0.18 ± 0.01	3.1×10^{-4}	397	NA	(2016)[69]
P-75	0.39	NA	0.141	0.027	1.46×10^{-4}	188.0	NA	(2018)[70]
P-90	0.52	NA	0.210	0.047	2.38×10^{-4}	198.2	NA	
P-100	0.28	NA	0.204	0.038	1.96×10^{-4}	192.4	NA	
P-90	0.87	0.78	0.009	0.0343	7.45×10^{-5}	261.5	41 ms	(2021)[81]
P-90	0.88	1.5	0.017	0.02	8.5×10^{-5}	217	NA	(2019)[71]
P-90 Acetone 15%	0.62	4.7	0.076	0.054	1.85×10^{-4}	317	NA	
P-90	1.6	1.8	0.0113	0.0624	8.0×10^{-5}	78	NA	(2020)[72]
P-90:TBAF(10%)	1.47	4.4	0.0299	0.213	1.6×10^{-4}	133	NA	
P-90:TBAF(40%)	1.16	10.5	0.0905	0.257	1.8×10^{-4}	143	24 ms	
P-90:TBAF(80%)	0.72	6.0	0.0833	0.24	1.6×10^{-4}	150	NA	
p(NDI-T2-L2)	1	0.84	0.0084	0.046	NA	95	40 ms	(2020)[92]
p(gNDI-gT2)	0.55	~0.13	0.13	0.06	2.2×10^{-4}	221	NA	(2021)[93]
p(C3-gNDI-gT2)	0.57	~0.34	0.34	0.13	9.2×10^{-4}	72	NA	
p(C6-gNDI-gT2)	0.46	~0.37	0.37	0.16	6.3×10^{-4}	59	NA	
p(C4-T2-C0-EG)	NA	~5	0.31	0.22	1.16×10^{-3}	188	24.6 ms	(2021)[73]
p(C2-T2)	NA	~7	0.4	0.2	3.97×10^{-4}	492	6.3 ms	
p(C4-T2)	NA	~11.5	0.63	0.3	1.90×10^{-3}	158	7.5 ms	
p(C6-T2)	NA	~30	2.28	1.29	4.74×10^{-3}	272	9.6 ms	
p(C8-T2)	NA	~7	0.15	0.13	3.76×10^{-4}	342	12.7 ms	
P(NDITEG-T)	NA	NA	0.031	0.04	2.4×10^{-4}	165.8	NA	(2022)[94]
P(NDIDTEG-T)	NA	NA	0.135	0.21	9.4×10^{-4}	221.5	NA	
P(NDIDEG-T)	NA	NA	0.359	0.51	2.12×10^{-3}	239.9	NA	

P(NDIMTEG-T)	NA	NA	0.378	0.56	2.23×10^{-3}	250.9	NA	
P4gNDTI	5.9	~30	0.47± 0.06	0.27±0.04	1.42×10^{-3}	167 ± 11.4	NA	(2022) [95]
2DPP-OD-TEG	1.15	84±19	0.73	~7	NA	61.6	500 ms	(2021)[74]
P(gPzDPP-2T)	6.55	31.4	0.048	0.18	1.6×10^{-3}	134	22.7 ms	(2022)[96]
P(gPzDPP-CT2)	0.68	29.5	0.43	1.36	0.019	91	3 ms	
P(gTDPP2FT)	0.6	930	NA	54.8	0.35	156 ± 24	1.75 ms	(2022)[75]
C60-TEG	2.8	4.1 ± 0.5	0.0146	7±2	0.03	220 ± 50	80 ms	(2019)[76]
PrC60MA	2	NA	6.1	21.7	NA	NA	20± 3ms	(2022)[77]
f-BTI2TEG-T)	6	160	0.27	2.3	0.044	52	322 ms	(2021)[78]
f-BTI2TEG-FT	5.25	2500	4.6	15.2	0.034	443	272 ms	
f-BTI2g-TVT	0.41	11	0.27	1.5	0.014	110 ± 19	68 ms	(2022)[79]
f-BTI2g-TVTCN	0.42	~800	12.8	41.3	0.24	170 ± 22	52 ms	
BBL	351	9700	0.276	NA	7×10^{-4}	930 ± 40	NA	(2018)[80]
BBL	0.8	65.1	0.815	1.99	2.14×10^{-3}	731	5.2 ms	(2021)[81]
BBL:PEI	1.67	380	2.28	NA	NA	NA	167 ms	(2021)[97]
BBL 15	0.04	~2.5	0.617	1.94	3.59×10^{-3}	540 ± 20	0.89 ms	(2022)[56]
BBL 60	0.04	~7	1.92	4.9	9.42×10^{-3}	520 ± 32	0.52 ms	
BBL 98	0.04	~16	4.04	10.2	0.0205	499 ± 19	0.43 ms	
BBL 152	0.04	~42	11.1	25.9	0.044	589 ± 26	0.38 ms	
PgNaN	15	~180	0.212	0.662	6.50×10^{-3}	100 ± 6	NA	(2021)[82]
PgNgN	5	~2.9	0.007	0.037	1.89×10^{-4}	239 ± 97	NA	
gNR	5E-5	7900	0.402	2.5 ± 0.1	0.013	198 ± 12	195 ms	(2022)[84]
hgNR	7.5E-5	7500	0.263	1.2 ± 0.04	9×10^{-3}	129 ± 3	128 ms	
gNR	3.5E-5	NA	1.21	5.12	0.0178	288 ± 12	94 ms	(2022)[83]
p($g_7NC_{10}N$)	14.9	580	0.37	1.83	0.012	153 ± 34	NA	(2022)[85]

2.3 OECT biosensors

Because of OECT's simple device structure, high current gain, and high stability in solution, they are wildly applied in biosensors for the detection of metabolites, nucleic acid, protein, and cells.[98] OECT biosensors can transform bio signals into electrical signals. The modification of biomolecules on the transistor interface can lead to changes in electrical potential or interface capacitance, thus altering the voltage or current of the electrical signal being measured.[99] Compared with inorganic materials, organic semiconductors and conductive polymers are easier to be fabricated on flexible substrates without the degrading of original electrical properties. Therefore, OECTs can also be applied in wearable biosensing for health monitoring.[100] In this part, different modification methods, sensing strategies, and bio-reorganization sites will be discussed.

2.3.1 Modification strategies

Strategies for bio modification are mainly divided into the physical adsorption, covalent binding, and bio-affinity interaction. Bare solid interfaces including the clean metal gate electrodes and inactive channel surfaces are usually difficult for bio grafting. Self-assembled monolayers (SAM) are introduced to provide surface functional groups through silanization or gold–thiol contacts. According to the chemical nature of solid interface and molecules to be grafted, the head and tail groups of SAM can be designed. The SAM layer are usually utilized for the connection of DNA or protein probe, which can provide carboxyl and amino end groups. In the case of antibody detection, one possible method is to use thioglycolic acid (TGA) with its thiol group in contact with a gold gate electrode, while the end carboxyl group is covalently bound to probe antigens. [101] Moreover, it is also feasible to directly modify the thiol functional group on the bio probe (such as ssDNA) for grafting on the gold gate electrode, escaping the SAM step. [102]

Bio probe can also be immobilized on solid interface through physical adsorption, which is widely used in enzyme-catalyzed reactions. Physical adsorption is a simple process that does not harm the enzyme's activity. Chitosan and Nafion are commonly used to assist the immobilization and improve the selectivity of enzymatic reactions.[103] Besides, the biotin avidin system (BAS) is often applied in transistor biosensors. The side chain of biotin ends with a carboxyl group, which can connect antibodies and other biological macromolecules. Biotin and avidin have strong affinity and specificity and are less affected by reagent concentration and pH value of the environment.[104] In addition to the solid interface modification, analytes labeling with nano materials or enzymes are also commonly used as a signal amplification strategy. Specific examples are given next for the explanation of different kinds of bioassays.

2.3.2 Bio reorganization

Bio-recognition sites for bio probe modification include the surface of the gate electrode, the surface of the channel, and in electrolyte. The specific binding with analytes includes nucleic acid hybridization, antigen-antibody binding, and enzyme catalysis reaction, et al. (Figure 2.3). Usually for higher sensitivity and selectivity, bioassays often involve interface modifications and analyte labeling.

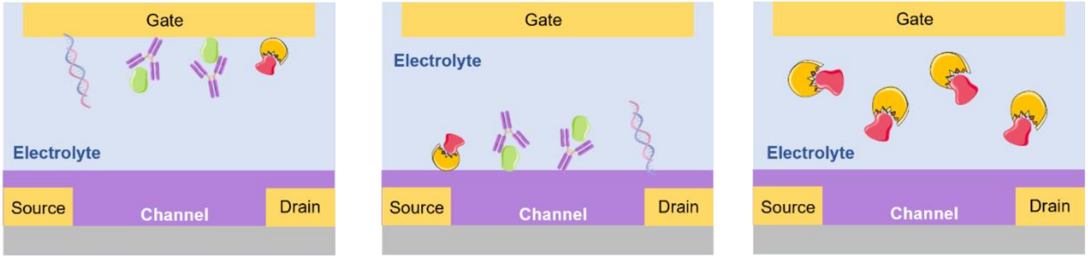

Figure 2.3 Scheme of three bio recognition sites (gate, channel, electrolyte) and different selective bio-binding types. The reaction between DNA strands, antigen/antibody, and enzymes/substrates are selectivity, which guaranteed the successful detection.

(1) Gate modification

The gate electrode is considered to be a stable and convenient bio-recognition site. The OECT biosensor gate electrodes are generally made of inert metal materials (such as gold, and platinum), which ensures the stability of the gate electrode in various liquid environments (water, high oxygen, acid, or alkali). Through SAM layer,[22,105,106] functional groups such as hydroxyl, carboxyl, and amino groups are easily modified on the gold electrode for the next step of biological modification. Au can also directly connect with the biomolecules having sulfhydryl groups, such as the designed ssDNA probes.[102] In the research of Fu et al., (Figure 2.4a), mercaptoacetic acid SAM layer was modified on Au gate to provide dense carboxyl groups for the next modification of probe antibodies.[69] The enzymes were introduced as a label of the analyte to amplify the bio signal, resulting a very low detection limit (10 fg mL^{-1}) of cancer biomarkers.

Except the inert gold electrodes, there are some functionalized gate electrodes, such as platinum electrocatalytic electrodes, and photoelectric effect electrodes. Platinum can catalyze the reaction of analytes such as hydrogen peroxide, dopamine (DA), uric acid (UA), and ascorbic acid (AA).[107] In the work of Xie et al.(Figure 2.4b), OECT was applied in the monitoring of neurotransmitter dopamine in rat brains.[107] The redox reactions of dopamine can be catalyzed by Pt gate and transmit the electrons to gate electrode, bring a decrease of gate potential. Finally, the mapping of evoked dopamine release at brain regions was demonstrated. To achieve high selectivity in metabolite analysis, enzymes (such as glucose oxidase, phosphatase, lactase, etc.) can be modified on the gate electrode to react with the corresponding analytes.[100,108] In a research that detect glucose exported from chloroplasts (Figure 2.4c), the PEDOT:PSS gate was modified with platinum nanoparticles and chitosan-crosslinked glucose oxidase.[109] The GOx and CHIT mixture was physically absorbed on gate surface to react with glucose, and the H_2O_2 produced can further react with Pt NPs. Electrons generated in this process can be directly transferred to the gate electrode and change the effective gate voltage. The gate potential variation brought by this direct charge transfer is obvious, which can achieve highly sensitive detection of metabolites.[110,111] The utilize of nano material for higher sensitivity and selectivity is common in gate modification.[112] Yan et al. had previously reported an flexible OECT for the detection of uric acid in saliva, in which the Pt gate was physically modified with PANI/Nafion-graphene bilayer (Figure 2.4d).[113] The bilayer can block the charged molecules such as AA and DA to enhance the detection sensitivity. Finally, the UA detection limit can reach 10 fM with very good selectivity.

In an organic photo electrochemical transistor (OPECT) biosensor,[114] the gate electrode is generally a transparent conductive electrode (such as ITO) modified with photosensitive species (such as CdS QDs). The light-generated gate potential can be varied by the steric hindrance of analyte, or the light quenching material labeled on the analytes. In research of Song et al. (Figure 2.4e),[115] CdS QDs and probe DNA were modified on the surface of ITO gate, and then the target DNA labeled with gold nanoparticles were connected to quench the photoelectric effect of cadmium sulfide. The sensitivity of this sensing is orders of magnitude higher than the steric hindrance effect DNA biosensor. Lin and Zhao's group have done lots of research on OPECT biosensors in recent years, including the detection of enzyme,[116,117] proteins,[114,118-121] RNA,[122,123] and ATP[124].

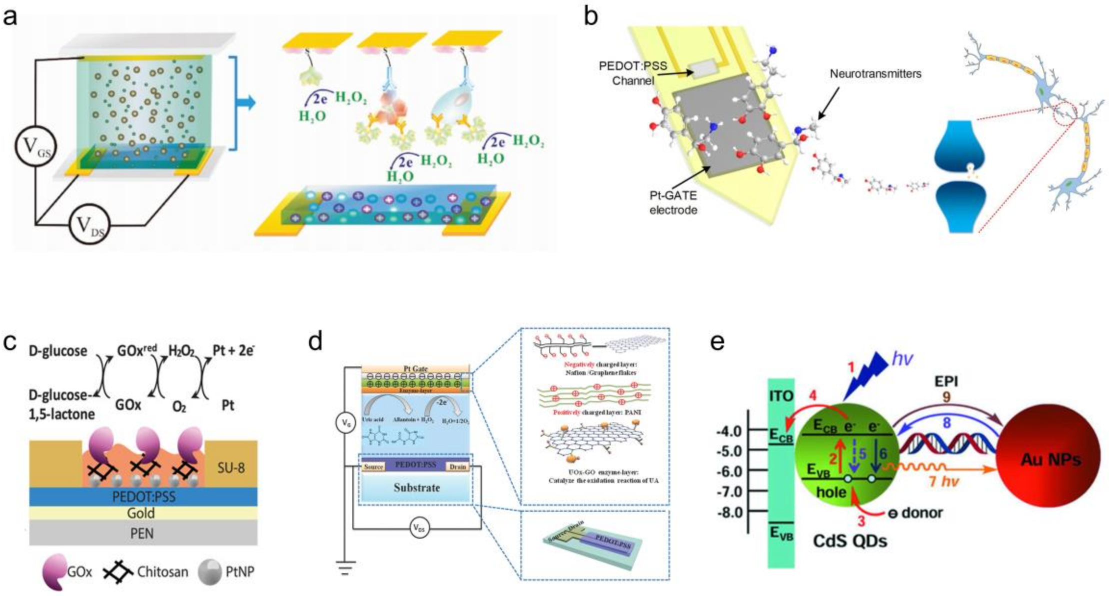

Figure 2.4 OECT biosensors with gate electrodes as bio recognition sites. (a) Detection of cancer protein biomarkers, the human epidermal growth factor receptor 2 (HER2). Horseradish peroxidase (HRP) and Au NPs are used as nanoprobe to enhance the detection sensitivity.[106] (b) Real-time mapping of dopamine in vivo. The Pt gate catalyze the redox reaction of dopamine. (c) Detection of glucose exported from

chloroplasts. The PEDOT:PSS gate was physically modified with glucose oxide and Pt nanoparticles. [109] (d) Detection of glucose and uric acid. The Pt gate is modified with PANI/Nafion-graphene bilayer.[113] (e) Detection of DNA. The ITO/CdS QDs gate has a photoelectric conversion function.[115]

(2) Channel modification

Bio modification on channel is not as common as gate modification in OECT biosensors since most channel material is not as stable as inert metal electrode. For channel modifications, biomolecules can directly generate steric hindrance on the surface of organic semiconductors or change the interface charge distribution and capacitance. Moreover, some conductive polymer is rich in functional groups for bio grafting. In research of Feno et al. (Figure 2.5a),[125] poly(3,4-ethylenedioxythiophene):tosylate (PEDOT:TOS) and polyallylamine hydrochloride (PAH) composites channel was fabricated for the detection of acetylcholine (LOD: 5 μM). In which, the PAH component can provide amino moieties as anchoring sites for the immobilization of the acetylcholinesterase (AchE). It is noteworthy that the application of nanomaterials for higher sensitivity also works in channel modification. In the study of Chou et al.,[126] poly(EDOT-COOH-co-EDOT-EG3) nanotubes were decorated on the channel layer (Figure 2.5b). The poly(EDOT-COOH) can chemically immobilize cortisol antibodies on channel, and poly(EDOT-EG3) can minimize nonspecific binding of other biomolecules. The nanotube structure was verified to immobilize more cortisol antibodies than bald PEDOT:PSS film. In the case of detecting cellular activity, channel modification is more commonly used than gate modification.[127-130] Cells are prone to attach and grow on the surface of organic semiconductor films. Single cell detection was realized by detecting the impedance of a dielectric microparticle (Figure 2.5c).[127] With the optimized device geometry, the OECT-based impedance sensor shows a high gain (20.2 dB) compared with single electrode-based impedance sensor. In 2018, Pitsalidis et al. demonstrated the cells growing in three-dimensional porous PEDOT:PSS-based scaffold channel (Figure 2.5d). Cells attached on the PEDOT:PSS pores and formed tissue, resulting the poor charge injection. Finally, the cells growth can be monitored by transistor electrical performances (channel current and response time) variation.

The gate electrode and the channel can both be settled as bio-recognize sites at the same time in one biosensor. Inal's group has done researches in metabolite detection with an n-type accumulation mode organic electrochemical transistor.[19,131,132] In 2018, they put forward a new concept in metabolite detection based on n-type OECT (Figure 2.5e).[58] The electron-transporting organic semiconductor is able to has direct electrical communication with oxidase and promote the ion-to-electron transducing qualities, which results higher sensitivity and fast response. The hydrophilic side chains of the n-type polymer P-90 serve as polar groups for enzyme modification, as well as promoting ion transport and injection. In addition to metabolites sensing, the detection of cell activities can also be conducted at both gate and channel sites. [133-135] Francesco's group used PEDOT:PSS-based OECTs to detect the growth and detachment of both leaky-barrier (NIH-3T3) and strong-barrier (CaCo-2) cell lines (Figure 2.5f). The planar configuration, in which cells grow on both the gate and channel, has been shown to have higher sensitivity due to the dual passage of ions through the cell layer.

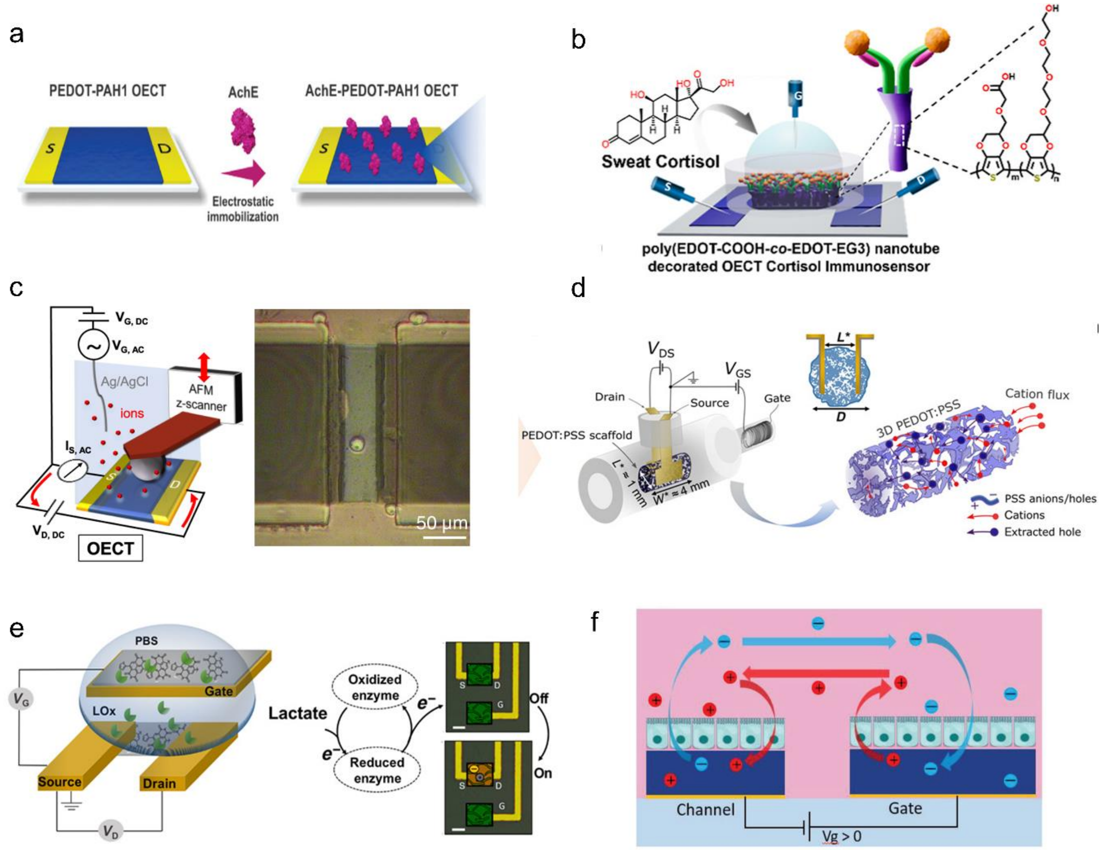

Figure 2.5 OECT biosensors can use either the channel (a-d) or both the gate and channel (e-f) as the bio-recognition site. (a) The immobilization of AchE on channel for the detection of acetylcholine.[125] (b) Polymer nanotubes immobilized on channel for the detection of cortisol. [126] (c) Single cell detection with a cell growing on the surface of channel.[127] (d) Monitoring cell growth in 3D scaffold PEDOT:PSS-based channel.[136] (e) The metabolite detection based on n-type OECT, in which the LOx was modified on both channel and gate surface.[58] (f) The growth of cells on both the gate and channel leads to higher detection sensitivity.[133]

(3) Reaction in electrolyte

The reactions that happened in the electrolyte are mainly related to enzymatic catalysis metabolites detection and cell tissue integrity monitoring. Through embedding the enzyme in solid state electrolyte, flexible OECTs can detect various metabolites including glucose, lactate, and alcohol (Figure 2.6 a,b) .[137-139] This method of placing enzymes into ion gel electrolyte is useful for portable detection and wearable electronics because the flexible device can stick to the skin surface to detect metabolites in sweat. To monitor cell growth, cells can be cultured not only on the channel surface, but also suspended in the electrolyte to avoid damaging the integrity of the channel film.[140] A transwell filter allowing ions penetration was placed in electrolyte to separate the gate and channel (Figure 2.6 c). If healthy cells attach to the filter to form a barrier tissue, ion migration to the channel will be hindered. This cell sensor can be applied in drug screening to identify drugs that disrupt cell-tissue barriers.

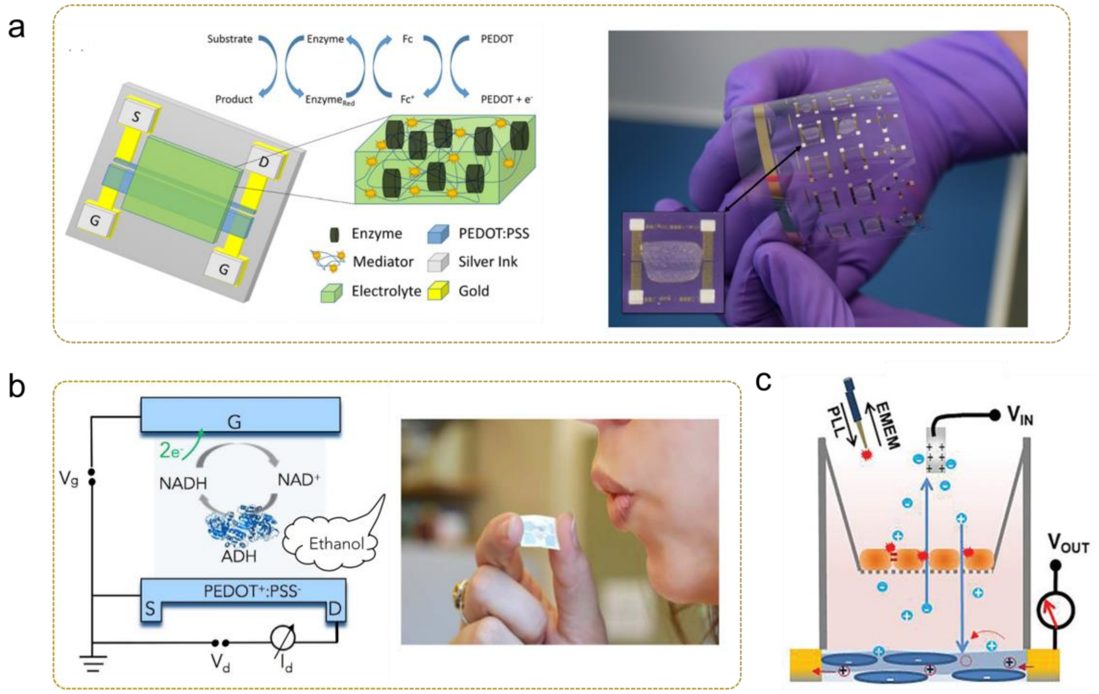

Figure 2.6 OECT biosensors with reaction in electrolyte. (a) Detection of lactate with flexible OECT devices, the enzyme was entrapped in the sol-gel electrolyte.[138] (b) Alcohol sensing by disposable paper-based OECT, the enzyme alcohol dehydrogenase (ADH) and its cofactor are trapped in electrolyte gel.[139] (c) Cell layer cultured on transwell filter is used as the barrier to regulate the ions penetration.[140]

2.3.3 Electrophysiology recording

Cells can generate action potentials when they are stimulated, which can be recorded in vivo with tiny electrodes or detected in vitro by electrodes pasted on the surface of the body.[141] Different types of cells produce electrical signals with different frequencies, ranging from one to hundreds of milliseconds. The action potentials or electric fields caused by cells can be generated and transmitted outward to the skin surface, which can then be measured by electrodes attached to the skin surface. Because the action potentials generated by specific muscles and organs are different, the detected electrophysiological signals are divided into electrocardiography (ECG), electroencephalography (EEG), electromyography (EMG), electrooculography (EOG), and in vivo electrocorticography (ECoG).[142]

The specific descriptions are as follows. (1) ECG signal is caused by cardiomyocytes. The rhythmic action potential generated by the sinoatrial node can be delivered to all cardiomyocytes by ion transport between cells, simultaneously initiating contraction and relaxation. Following is the transmission of generated electric field to the skin surface. The ECG wave contains three main parts, the P wave, the QRS complex, and the T wave, which represents the activity of different ventricles of the heart. The waveform of the ECG changes depending on where the electrodes are located. (2) EEG records the activity of cortical brain cells. EEG needs to observe the frequency, amplitude, and phase parameters of brain waves, which have four main frequency bands: α, β, δ, and θ. EEG can be used to detect epilepsy, sleep disorders, and neurological disorders. (3) EMG records the potential changes of muscle cells after being stimulated by nerves or electric currents. Epidermal EMG shows a potential difference between the two electrodes, which have larger noise than the signal of intramuscular EMG. The electrodes of EMG are usually placed on sebum-thin muscles to get stronger signals. EMG has no specific waveform and needs to filter out high frequency noise. (4) EOG detects electrostatic potential and can be used to record eye movements. There is a resting potential across the omentum, positive on the corneal side and negative on the scleral side. For left and right eye movements, electrodes are placed on the inner and outer corners of the eye, and when moving up and down, the electrodes are placed on the upper and lower eyelids. The potential difference between the two electrodes can be recorded. (5) ECoG also records the activity of brain cells, but it is invasive. Due to direct contact with brain cells, it has a higher spatial resolution, larger signal amplitude, and is less susceptible to other electrophysiological signals such as EMG and EOG.

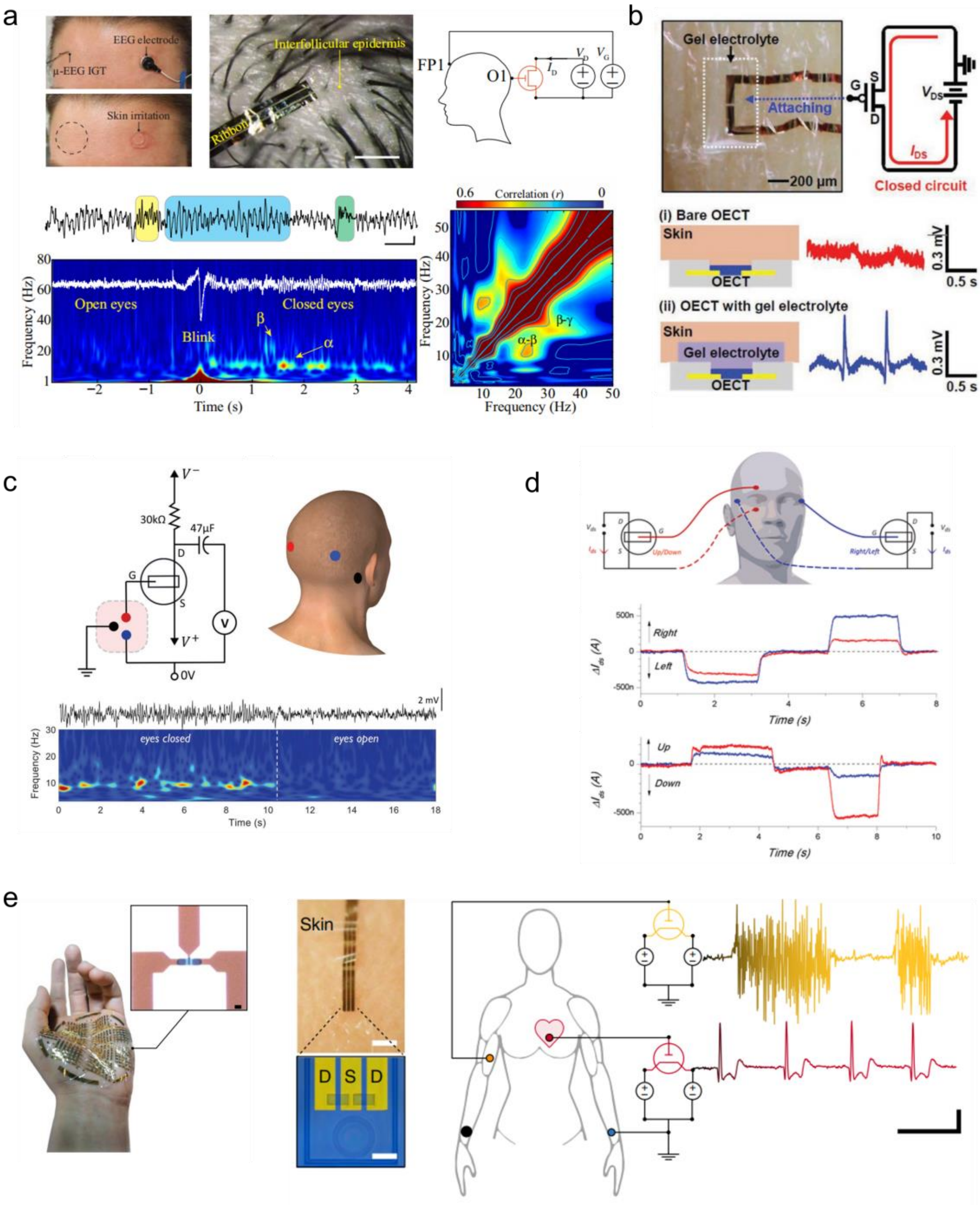

Figure 2.7 In vitro electrophysiological sensing of (a,c) EEG, (b) ECG, (d) EOG, and (e) EMG based on OECTs.[21,47,55,143,144]

To achieve favorable electrophysiology recording, devices should possess the following characteristics: (1) High transconductance. High transconductance means higher current gain and high resolution, a small change of gate potential can induce large current variation. (2) Low subthreshold slope. Different from the current gain, when signals are transferred to voltages, devices with a low subthreshold slope can induce larger voltage gain and higher transconductance efficiency. (3) Fast response. This parameter is important for electrophysiological sensing because the active potential switching is fast, especially for the detection of high frequency EEG. The response time of OECTs has been improved to below 10 μs with different techniques, which fully meet the testing needs. (4) Wearable electronics. Organic devices are suitable for the preparation of flexible and stretchable electronics. By combining with integrated circuits, signals at different positions can be mapped. Overall, for both in vitro (Figure 2.7) and in vivo recording (Figure 2.8), OECTs have achieved good experimental results.

(1) In vitro electrophysiology sensing

George D. Spyropoulos reported an internal ion-gated organic electrochemical transistor (IGT), which has high-transconductance, fast response, biocompatibility, and conformability.[55] In IGT, mobile ions are trapped in the conducting polymer and form a self-(de)doping process that is no need of ion exchanging from the electrolyte. The IGTs can be applied in integrated circuits such as digital logic gates and cascaded amplifiers. They are micrometer-scale and are easily attached to the skin or scalp without broking the skin (Figure 2.7a). EEG signals are record with the α, β, γ frequency bands, and demonstrate the reactivity of posterior dominant rhythm to eye closure. Takao Someya group has attributed a lot to ultrathin soft bioelectronics.[143] They demonstrated a wearable electrophysiological sensor based on a thin gel electrolyte (Figure 2.7b). The soft electrode can be attached to dry skin and monitor bio signal stably for more than one week.

Pierre Leleux verified that OECTs can measure a broad range of typical clinical electrophysiological signals, in which ECG, EOG, and EEG were all demonstrated.[144] EOG was recorded through changes in channel current when the eyeball moves up and down and from side to side (Figure 2.7d). It can also detect symptoms of drowsiness, and detect the frequency and duration of spontaneous blinks. Claudia Cea[47] reported high performance ion-gated organic electrochemical transistor (5 μm channel length, 2.9 μs rise time, 1.5 mS transconductance) for both in vivo and in vitro monitoring. In this work, even high frequency EMG signals can show low noise and high SNR (Figure 2.7 e).

It's worth noting that the in vitro sensing OECTs mentioned above are primarily based on a PEDOT:PSS channel, with few reports utilizing other high-performance materials aside from p(g2T-TT). Vishak Venkatraman used p(g2T-TT) based OECT to detect electroencephalogram (Figure 2.7 c), taking advantage of its low subthreshold slope and high voltage gain.[21] In addition, different from PEDOT:PSS, p(g2T-TT) based OECTs are enhanced mode, enabling low power consumption. More channel materials are expected to have prominent applications in OECT based electrophysiological sensing.

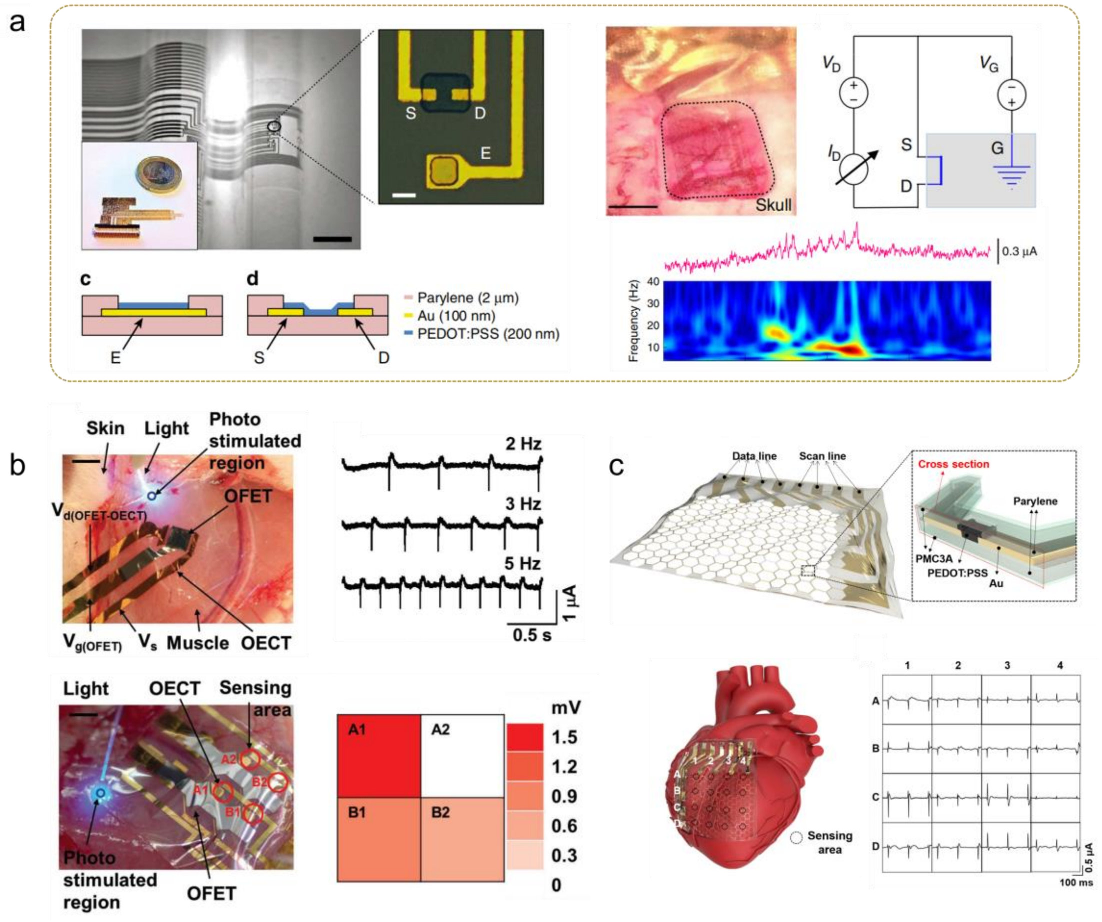

Figure 2.8 OECT based in vivo electrophysiological sensing of (a) ECoG, (b) EMG, and (c)EEG.[20,34,145]

(2) In vivo electrophysiology sensing

The in vivo detection by OECTs relies on its flexibility and biocompatibility. Dion Khodagholy fabricated PEDOT:PSS based OECT on the 2 µm thick parylene film substrate.[34] Ultrathin devices were patched on the somatosensory cortex of rats for ECoG detection (Figure 2.8 a). The ultra-flexible OECTs arrays have a high signal-to-noise ratio for epilepsy recordings. In addition to being attached to brain cells to detect ECoG, it can also be placed on muscle cells (Figure 2.8 b) and on the heart (Figure 2.8 c) to detect EMG and ECG.[20,145] These ultra-flexible multielectrode OECT arrays can conformal contact with the surface of organs and behaving high spatial-temporal resolution. Compared with in vitro detection, in vivo sensing shows an obvious higher signal-to-noise ratio, which is promising for brain-computer integration.

Chapter 3 Short-channel vertical organic electrochemical transistor

The limitations of short-channel effects and fabrication techniques make it difficult to promote Moore's Law. Although many new technologies are trying to reduce transistor channel length and gate length, however, they are still limited by poor device performances and practical availability. Here we report a vertical organic transistor with a channel length as short as 0.86 nm, which is dependent on the thickness of the oxide spacer. Organic electrochemical transistors (OECTs) based on this vertical structure can overcome the short-channel effect and achieve excellent transistor performances. The on-off current ratio of ultra-short (0.86 nm) channel OECT is 476. Both p-type and n-type devices with channel lengths longer than 1.8 nm can realize on-off current ratio of over 10^6 and ideal subthreshold slope of 60 mV/dec. Short-channel OECTs can achieve high width-normalized transconductances of 3960 S/m. OECTs that operate at low voltages can overcome the short-channel effect, making them a promising technology for the development of next-generation electronic devices.

3.1 Introduction

Moore's law predicts that the number of transistors in a dense integrated circuit doubles about every two years.[146] The fabrication of transistor is now struggling on 5 nm and 3 nm nodes.[147] Further reducing the transistor size depends on the development of more sophisticated fabrication processes or the creation of ingenious device structures. Due to the limitation of lithography technology, it is almost impossible to fabricate planar structure transistors with a channel length below 10 nm.[148]

The current state-of-the-art fabrication techniques for transistors with dimensions smaller than 10 nm are based on vertical structures. 1-nanometer physical gate length MoS_2 transistor was realized in 2019 by Ali Javey's group.[149] In their device, a single-walled carbon nanotube (SWCNT) gate and a MoS_2 channel are spaced by a ZrO_2 gate dielectric. The physics gate length is dependent on the thickness of ZrO_2. In this work, the key to reduce the source-to-drain tunnelling leakage current is decreasing the thickness of the MoS_2 film. After two years in 2022, a gate length approaching 0.34 nm was realized by sidewall MoS_2 transistor, which is gated by the edge of graphene.[150] In addition to the above two latest shortest gate lengths, the channel length can be shortened to 0.62 nm. In 2021, reported by Yuan Liu et al.,[151] a vertical MoS_2 transistor with a 0.65 nm channel length was fabricated with an on-off current ratio of 26. The channel length is determined by the thickness of the semiconductor layer. From the latest progresses, it can be summarized that there are two key points to achieve the nano dimension (either gate length or channel length). (1) Sophisticated device structure. An alternative method is using vertical device structures, in which, the thickness or boundaries of the thin films (including semiconductor layers or dielectric layers) are used to define transistor dimensions. (2) Low leakage current. Leakage current mainly includes source-to-drain tunnelling current and source-to-gate leakage current, which are determined both by the device structures and materials. Low off current ensures the modulation capability of short-channel transistors.

To achieve an ultra-short-channel length in a vertical transistor, the channel length can be determined by either the thickness of the semiconductor layer or the edge length of the dielectric spacer. One of the challenges associated with the continuous reduction of channel length is the increased tunnelling current, which can negatively impact the on-off switching characteristics of the transistor. The level of the source-drain tunneling current is related to the applied voltage, overlap area, spacer film thickness, and properties of spacer materials.[152] Obviously, choosing a dielectric spacer is better than directly using the semiconductor film between two vertically stacked electrodes in obtaining a small tunneling current. Al_2O_3 is an available high dielectric constant insulating material, which thickness can be precisely controlled by low-temperature atom layer deposition technology.[153]

It is important to note that smaller dimensions increase the probability of deviation during device fabrication and create more challenges in precisely controlling device topography. To maintain uniform geometry size and electrical performance, it is necessary to avoid complicated and rigorous device preparation processes. For example, in the fabrication process of two-dimensional material field effect transistors, techniques such as film stripping, transfer, etching, and van der Waals metal integration technique are often involved. Regularizing the area and thickness of 2D materials is often challenging, and the thin-film transfer process can increase variability in device performance. The photolithography and etching steps required in these approaches can also make fabrication more complicated, which may not be suitable for low-cost electric circuits. In contrast, organic semiconductors may offer simpler fabrication processes that are more cost-effective.

Organic electrochemical transistors outstand for their simple device structure, low applied voltages (below 1 volt), and high transconductance, which is a critical ingredient of flexible and low-cost organic electronics.[2,154] OECT channel current is modulated by gate voltage through ion doping/dedoping from the electrolyte to organic semiconductors. Few reported vertical structure OECTs use parylene as channel spacer, which is about a few hundred nanometers and cannot acquire the ultra-short-channel length.[155,156]

In this chapter, a straightforward but delicate vertical device structure is designed and demonstrated. An aluminum oxide layer is fabricated as a channel spacer between two vertically stacked electrodes, and the channel length is determined by the Al_2O_3 layer thickness. The low-temperature atom layer deposition is conducted with 5-67 cycles pulses, with channel length varying from 0.86 nm to 12 nm. Three organic semiconductors, the most studied PEDOT:PSS, the top performer p-type polymer p(g2T-TT), and a newly reported high-performance n-type polymer p($g_7NC_{10}N$) are tested as channel materials. The on-off current ratio is 476 even with 0.86 nm ultra-short-channel length. OECT devices with channel lengths larger than 1.8 nm can reach on-off current ratio of over 10^6 and ideal subthreshold slope of 60 mV/dec. The short-channel effect is significantly reduced in OECTs due to their low gate voltage, low drain voltage, and high gate capacitance. Short-channel OECT device can achieve high width-normalized transconductances of 3960 S/m, which is less limited by channel width and thickness, and shows good stability under long time testing.

3.2 Experimental Section

3.2.1 Materials

Poly(3,4-ethylenedioxythiophene)−poly(styrenesulfonate) (PEDOT:PSS) (Clevios PH-1000) aqueous solution was purchased from Heraeus Ltd. GOPS [(3-glycidyloxypropyl)trimethoxysilane] was purchased from International Laboratory, USA. P(g2T-TT) and p($g_7NC_{10}N$) were synthesized by Iain McCulloch's group.[85,87] SU-8 photoresists, AZ5214 photoresists were purchased from Microchemicals GmbH. Chloroform, methylpyrrolidone, dimethyl sulfoxide (DMSO), and glycerin were purchased from Sigma-Aldrich Co.

3.2.2 Device fabrication

Electrodes (source, drain, and gate) were fabricated by multiple photolithography and magnetron sputtering (Figure 3.1). Photoresist AZ5214E was negatived patterned for smooth metal edges. 10 nm Cr and 40 nm Au were sputtered on clean silicon oxide substrate. The first layer of photolithography was prepared for the source and gate electrode. For the Ag/AgCl gate, another layer of photolithograph and magnetron sputtering of Ag was added to cover the Cr/Au gate electrode. The third layer of photolithography pattern was shared by an aluminum oxide dielectric layer and the drain electrode. The dielectric layer Al_2O_3 was deposited by atom layer deposition

(ALD) using the TMA/H_2O-plasma gas pulse at 80 °C. The thickness of Al_2O_3 was controlled by TMA/H_2O plasma cycle numbers. The second layer of Cr/Au drain electrode was deposited by magnetron sputtering. The metal electrodes lift off process was conducted by immersing in methylpyrrolidone (NMP) overnight. The overlap width of the two electrodes is 5 ± 1 μm. The SU8 layer was used for photolithography to shield the Au electrodes from the aqueous electrolyte. Subsequently, a channel window was created using the fifth layer of photoresist. To prepare Ag/AgCl electrode, the Ag gate was immersed in 0.5 M HCl and applied a positive voltage (0.3 V, Pt cathode) for 1 min.

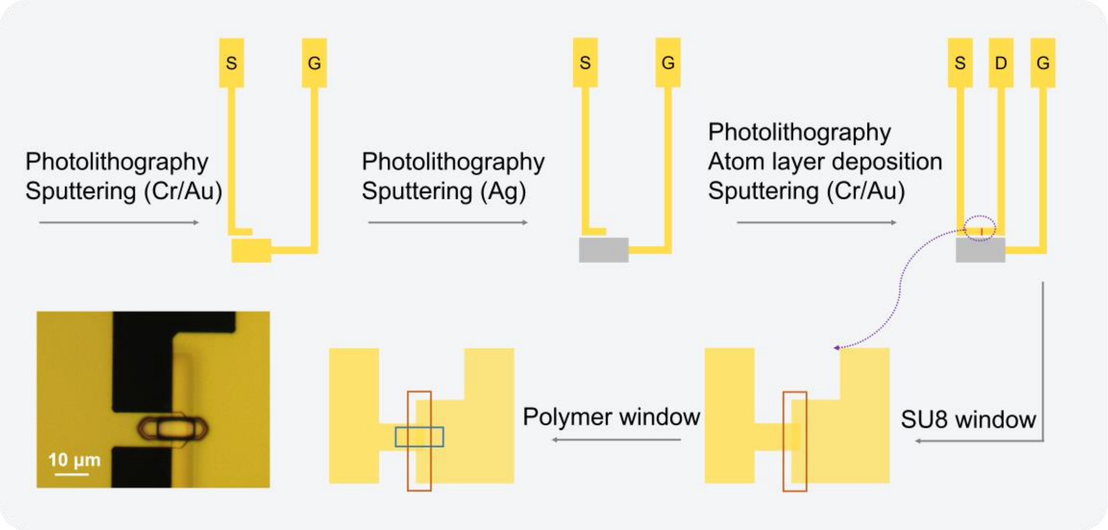

Figure 3.1 Fabrication process of the short-channel vertical OECT. Inset is the microscope image of the device. The widths of top and bottom electrodes are 10 μm and 60 μm respectively. The electrodes overlap is about 5*10 μm^2, and the channel width is 5 μm, channel area is about 5*20 μm^2.

As to channel materials, PEDOT:PSS was mixed with dimethyl sulfoxide (DMSO) and glycerin (both with a volume ratio of 5% and cross-linker (3-glycidyloxypropyl) trimethoxysilane (GOPS) (1%). PEDOT:PSS was then spin-coated (3500 r/s, 30s) on the positive patterned AZ5214E photoresist and annealed at 110 °C for 20 min. P(g2T-TT) (2 mg/ml) and P($g_7NC_{10}N$) (5 mg/mL) were diluted in chloroform separately and spin coated (1000 r/s) on the patterned AZ5214E layer. The resulting films were then annealed at 100°C for 30 min.

3.2.3 Device characterization

The electric characteristic transfer curves, output curves of OECT devices, and tunneling currents were tested by Keithley 4200A-SCS Parameter Analyzer. The device stability was tested by Agilent 33220A waveform generator and Keithley source meters (Keithley 2400). The AFM images were tested by Scanning Probe Microscope (Asylum MFP-3D Infinity).

3.3 Results and Discussion

3.3.1 Device structure with ultra-short-channel

(1) Negative patterned electrodes with smooth edges

To prevent short circuits, it is important to ensure that the edges of the vertically stacked electrodes are smooth. Photolithography can be categorized into two types: positive pattern and negative pattern (Figure 3.2). The negative pattern process is prone to obtaining neat and smooth electrodes, which also makes the lift off process to be easier. The Cr /Au electrodes prepared by the two kinds of processes are shown in Figure 3.3. According to the AFM morphology characterization, it can be verified that the edge prepared by the negative pattern process is a smooth slope, and there are no uplifted metal spikes. According to the microscope images, it can also be observed that the overlap edges of the top electrode and the bottom electrode are cleaner and tidier. Smooth edges prevent the connection of source-drain electrodes, which aids in achieving a shorter channel length.

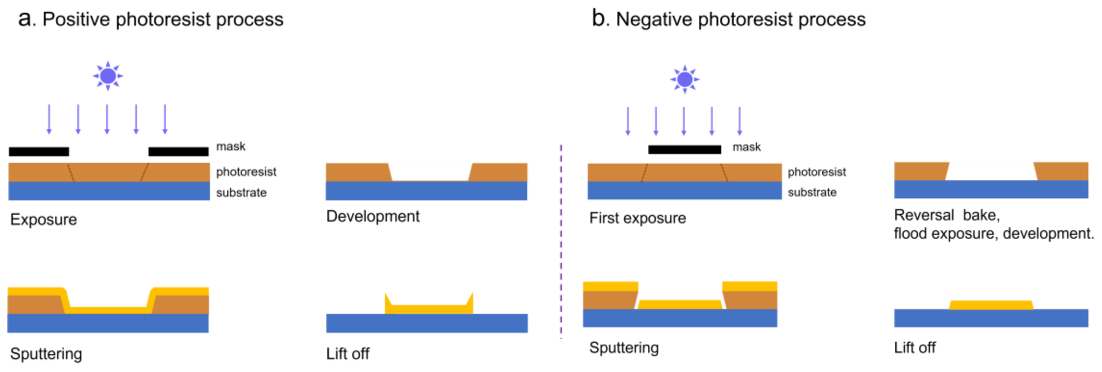

Figure 3.2 The photolithography process of (a) positive pattern and (b) negative pattern. The electrode edges fabricated by the two methods are different.

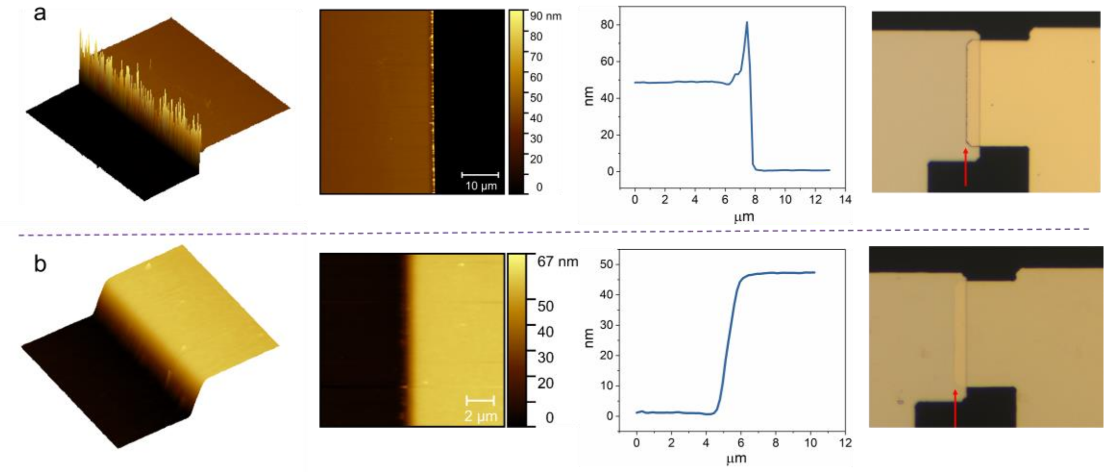

Figure 3.3 AFM images of (a) positive patterned and (b) negative patterned Cr/Au electrode. The micrographs show the overlap of top and bottom electrodes.

(2) Preparation of Al_2O_3 layer with different thickness.

H_2O and trimethylaluminum (TMA) pulse were used for the deposition of Al_2O_3 films. The pulse time of H_2O and TMA are both 0.015s, which were separated by 10 s nitrogen purging. The substrate temperature keeps 80 °C during the whole process. AFM images of Al_2O_3 film deposited with different cycle numbers were shown as Figure 3.4. The thicknesses of Al_2O_3 film with 5, 7, 10, 14, 27 ALD cycles are about 0.86 nm, 1.2 nm, 1.8 nm, 2.4 nm, and 4.8 nm respectively, which shows a very good linear relationship.

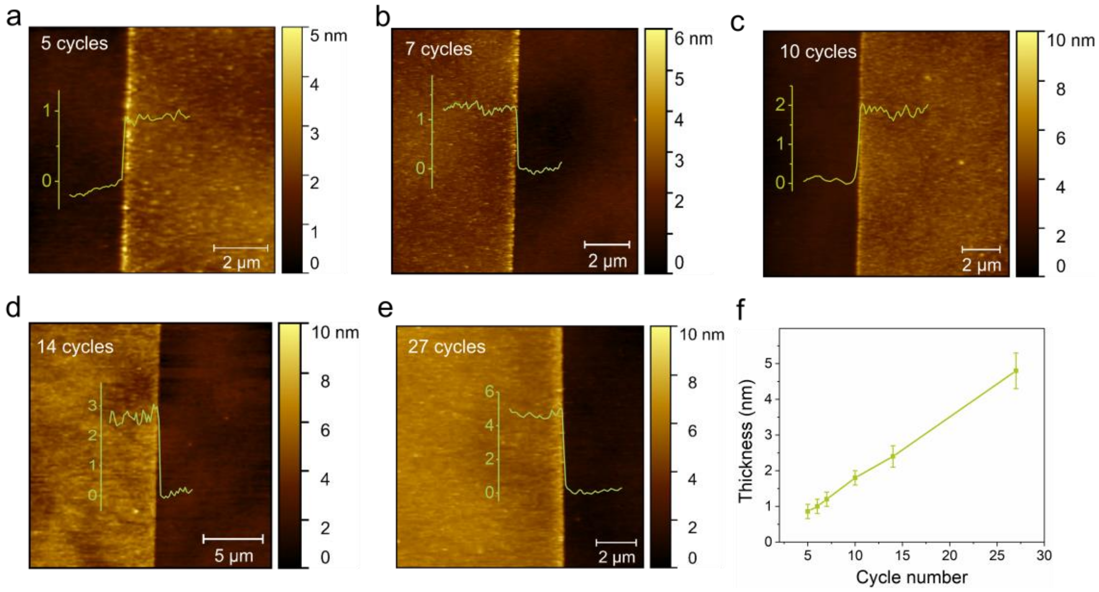

Figure 3.4 (a-e) AFM images of the Al_2O_3 film deposited with 5, 7, 10, 14, and 27 ALD cycle pulses. The corresponding average thicknesses are 0.86 nm, 1.2 nm, 1.8 nm, 2.4 nm and 4.8 nm. (f) Relationship of Al_2O_3 film thickness with the ALD cycle numbers.

(3) Vertical OECTs and morphology characterization

The vertical structure was fabricated by twice photolithography and magnetron sputtering (Cr/Au) process and one ALD process. The top Cr/Au electrode shares the same photolithography pattern with the Al_2O_3 layer. Figure 3.5a shows the scheme of the vertical structure, in which the channel length is depended on the thickness of the Al_2O_3 layer. AFM stereogram shows smooth surfaces of the top and bottom electrodes overlap. Both the top and bottom electrodes have a height of around 50 nm. Figure 3.5bc shows AFM image and optical microscope image of electrodes overlap. The bottom electrode is 10 µm width, overlap length of two electrodes is about 5 µm. The schemes of OECT device (transverse and longitudinal sections) are shown in Figure 3.5de. In which, the organic semiconductor was spin coated on the edge of top electrode. The electrodes that used as leads are covered by photoresist SU8 to minimize the gate leakage current.

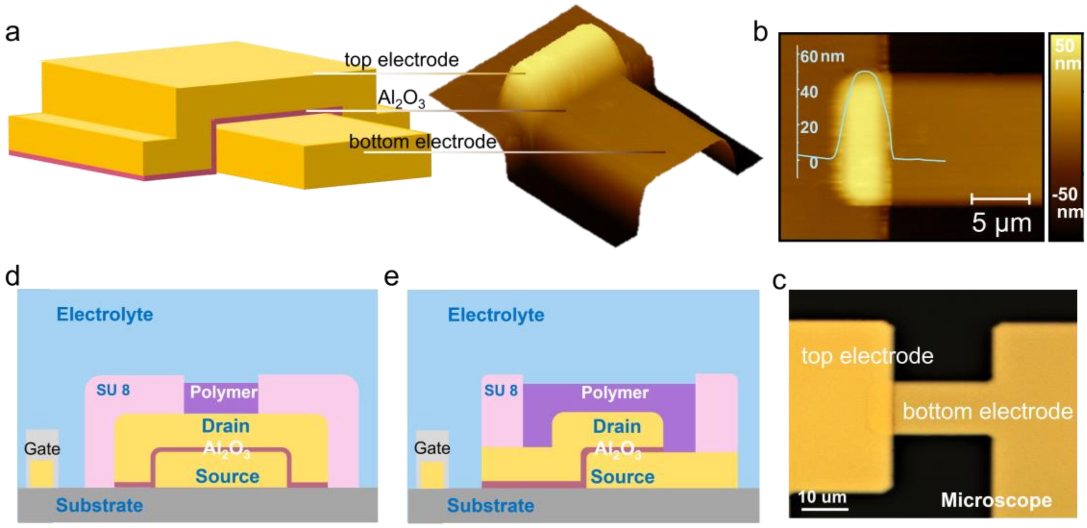

Figure 3.5 Vertical short-channel OECT device structure. (a) Structure of oxide spacer determined short-channel. On the right is the AFM stereogram of the stacked electrodes. (b) AFM image of overlapped top and bottom electrode. The heights of both electrodes are around 50 nm, the overlap length is around 5 µm, and the ALD is 7 cycles (~ 1.2 nm Al_2O_3). (c) Microscope image of the source drain electrodes overlap. (d) The transverse and (e) the longitudinal sections schemes of the OECT device.

In addition to observing the electrode morphology and the Al_2O_3 film thickness thorough AFM images, the existence of the Al_2O_3 layer is also observed with high-resolution transmission electron microscopy (HRTEM) and high-magnification EDS mapping (Figure 3.6). The EDS mapping image shows signals of Au, Cr, and Al. The signals of Al and Au overlapped because their EDS energy values are close, making peaks divided together. By HRTEM image, the Al_2O_3, Cr, and Au layers can be distinguished by the contrast differences. The thickness of Al_2O_3 is around 1 nm (7 cycles ALD).

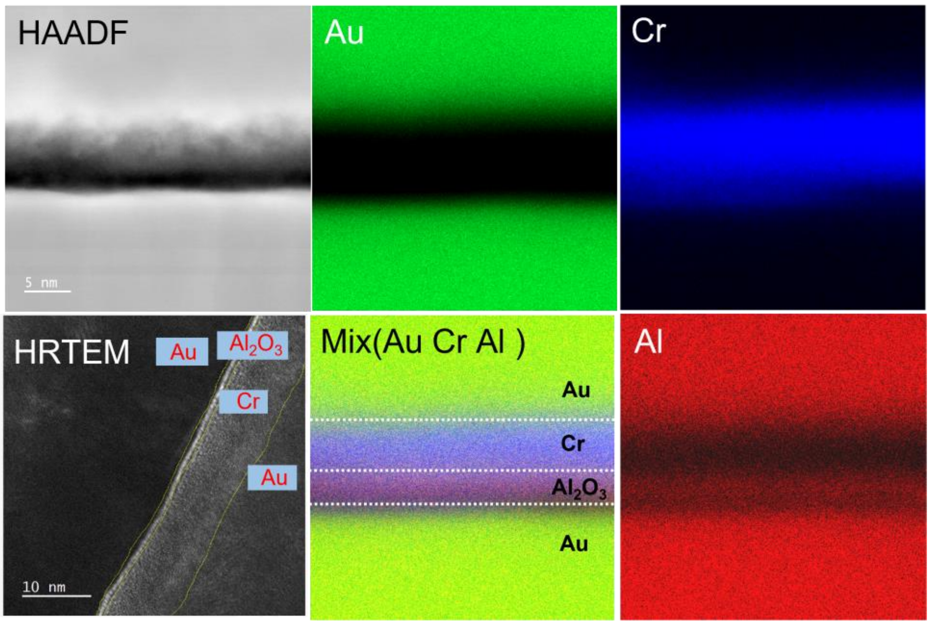

Figure 3.6 HAADF image, EDS mapping, and HRTEM image of Au-Al_2O_3-Cr-Au layers.

3.3.2 Oxide tunneling current

The thickness of the Al_2O_3 layer determines the transistor channel length. However, using an ultra-thin Al_2O_3 layer results in higher tunneling current, which is dependent on several factors such as the material of the metal electrode and oxide layer, the thickness of the oxide layer, the overlap area, and the applied voltage. The influence of the overlap area is shown as Figure 3.7. The Al_2O_3 thickness is around 1.2 nm with 7 cycles ALD, and the overlap length is about 5 μm. The tunneling current increase with the increasing of bottom electrode width (10 μm, 15 μm, 40 μm), and exhibit a good linear relationship.

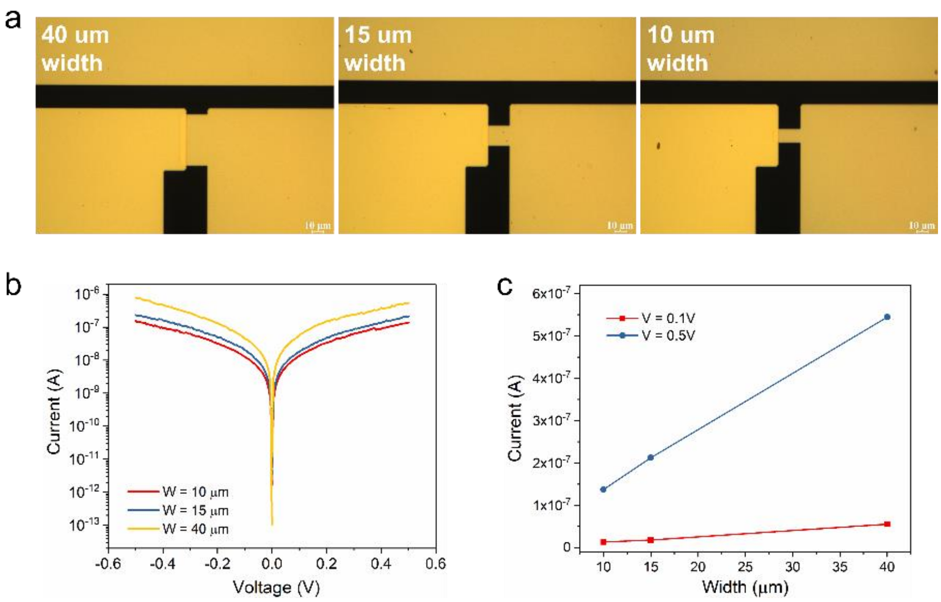

Figure 3.7 The tunneling currents with different electrodes overlap area. (a) The micrographs of source drain electrodes with different overlap area. (b) The tunneling currents with 10, 15, 40 μm overlap width. (c) The linear relationship between tunneling current and the overlap area.

Tunneling currents of Al_2O_3 film with different thicknesses were tested as shown in Figure 3.8. With the increase of Al_2O_3 thickness, the tunneling current decreased obviously. When the ALD cycle number is 4, the voltage bias and current are a linear relationship (Figure 3.8b), which means that the source and drain electrodes are shorted. The electrode resistance is around 200 ohms with 50 nm Cr/Au electrodes. With 7, 14, 27 cycles ALD, the IV curves exhibit exponential increase, $I = A*\exp(-V/t) + y_0$. The value of A and y_0 are found to be almost equal, the exponential function can be approximated as $I = A*[1+\exp(-V/t)]$. With the increasing of Al_2O_3 thickness, the values of A decrease rapidly, and the t values have no obvious change.

On the other hand, the asymmetry of I-V curves under positive and negative voltage bias can be observed. That means electrons are easier to cross Au-Al_2O_3- Cr barrier than Cr-Al_2O_3-Au barrier. Therefore, for electrical characterization, always keeping the Cr electrodes at lower potential is helpful to decrease the tunneling current. Figure 3.8c shows the detail of tunneling currents with different ALD cycles numbers from 4 to 27.

Figure 3.8d shows the relationship between tunneling current and ALD cycle numbers under 0.1 V and 0.5 V voltage bias. With the decreasing of ALD cycles, especially under 10 cycles, the tunneling current increases dramatically beyond the exponential increase.

The above findings pertain to the investigation of source drain tunneling current. However, for a complete OECT device, it's important to factor in the impact of gate current on the device's electrical performance. Figure 3.8e shows the OECT device current distribution diagram. Finally tested Ids includes oxide tunneling current, portions of gate current, and channel current flowing through the semiconductor polymer.

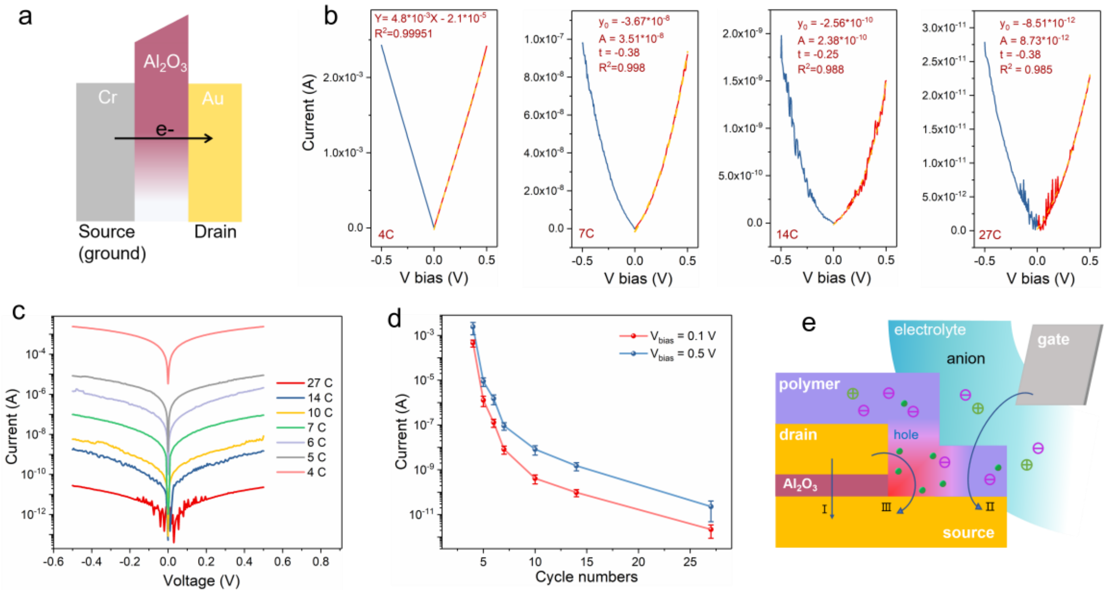

Figure 3.8 (a) Energy band diagram of Cr-Al_2O_3-Au structure. (b) The linear (4 cycles) and exponential (7, 14, 27 cycles) fitting of tunneling IV curves. (c) The tunneling current between source and drain electrodes with different Al_2O_3 film thickness. ALD cycles numbers are from 4 to 27. (d) Relationship between tunneling current and ALD cycle numbers under 0.1 V and 0.5 V voltage bias. (e) The current distribution diagram of OECT devices.

3.3.3 OECT electrical performances

OECT devices with different channel lengths (from 0.86 nm to 12 nm) were fabricated. Three kinds of conducting polymers, the most studied PEDOT:PSS, the top performer p-type polymer p(g2T-TT), and a newly reported high-performance n-type polymer p($g_7NC_{10}N$), were tested with the short-channel vertical OECTs. Transfer curves of devices with different channel lengths were shown in Figure 3.9a. For p(g2T-TT) based devices (Vd = -0.1 V), the on current with different channel lengths are similar, and the main differences are shown at the off current. In devices with channel length from 0.86 nm (5 cycles) to 1.2 nm (7 cycles), the oxide tunneling current is the main component of the off current, which is larger than the gate leakage current Ig. This result is consistent with the tunneling current discussed above. For devices with channel lengths from 1.8 nm to 12 nm, the tunneling current is very small, and the off current is mainly affected by the gate current Ig, which is independent of the channel length. The same is applied to other two polymer p($g_7NC_{10}N$) (Vd = 0.1 V) and PEDOT:PSS (Vd = -0.1 V). Because of the lower gate voltage and lower polymer conductivity at the off state, p($g_7NC_{10}N$) devices show a very low gate current. Therefore, n-type devices are tested with lower off current, which are mainly affected by the tunneling current. For PEDOT:PSS devices, due to the higher gate voltage (1V) at the off state, the gate current is larger, decreasing the on-off current ratio. Figure 3.9b shows that the short-channel OECT exhibits output curves with well-defined linear and saturation regimes. Due to the low operating voltages, low tunneling currents can be obtained even with very thin Al_2O_3 film.

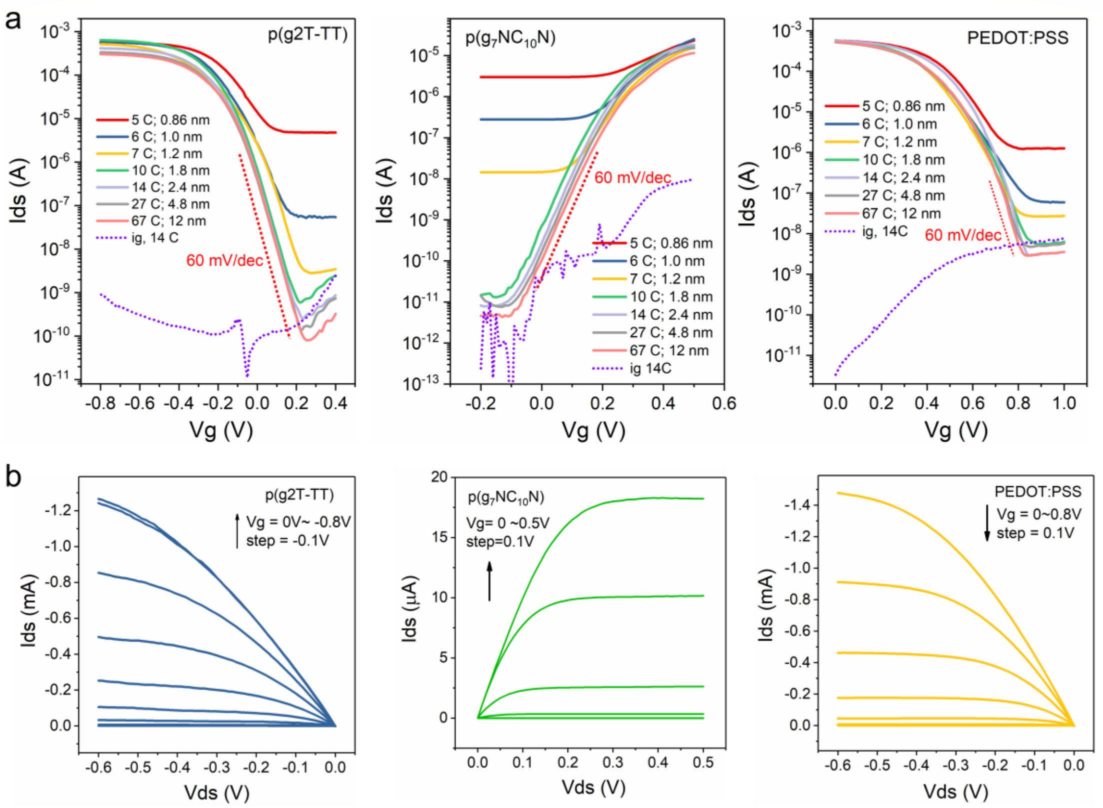

Figure 3.9 (a) Transfer curves of OECT devices with different channel lengths (from 0.86 nm to 12 nm). Three typical channel materials p(g2T-TT), p($g_7NC_{10}N$) and PEDOT:PSS were demonstrated. (b) Output characteristics of OECT devices, the channel lengths are 2.4 nm.

The on-off current ratios of three kinds of OECT devices with different channel lengths are concluded as Figure 3.10a. When channel lengths are longer than 1.8 nm (include), the on-off current ratios of p(g2T-TT) and p($g_7NC_{10}N$) devices are all higher than 10^6, and are higher than 10^5 for PEDOT:PSS devices. When the channel length is shorter than 1.8 nm, the on-off current ratios decrease rapidly. Same happened for subthreshold slope (Figure 3.10b). Devices with channel length longer than 1.8 nm can all achieve ideal subthreshold slope of 60 mV/dec, which is less affected by short-channel effects. Electrolyte gating facilitate very high gate coupling which enables full control of the charge carrier density via ions diffusing into the semiconducting channel.[157] Therefore, short-channel effects are drastically decreased. Even though there was a reported OECT realized ideal subthreshold slope by p(g2T-TT) channel, [87] but its channel current not across multiple orders of magnitude like the short-channel OECT devices. From the transfer curves above, the p(g2T-TT) device can keep ideal subthreshold slope of 60 mV/dec over a current range of about 4 orders of magnitude, while the n-type p($g_7NC_{10}N$) also keep over 3 orders of magnitude. Affect by the larger gate leakage current, the PEDOT:PSS device can keep ideal subthreshold slope over a current range around 2 orders of magnitude.

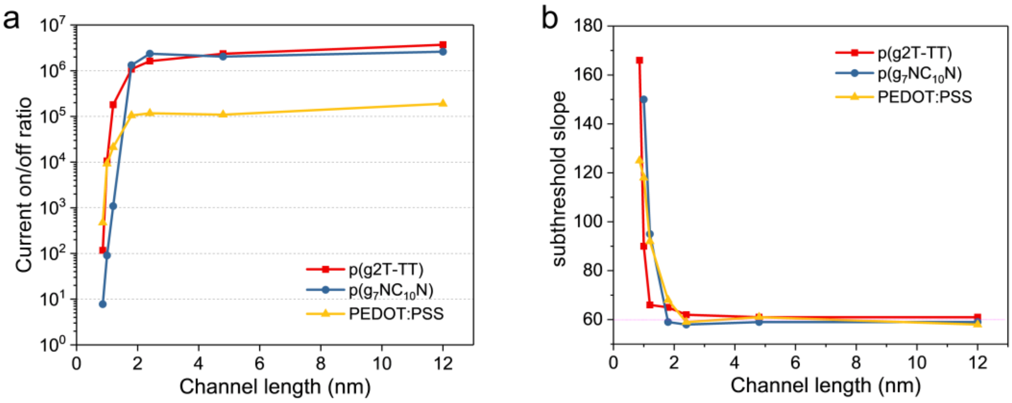

Figure 3.10 (a) The relationship between on-off current ratio and the channel length. (b) The relationship between subthreshold slope and the channel length.

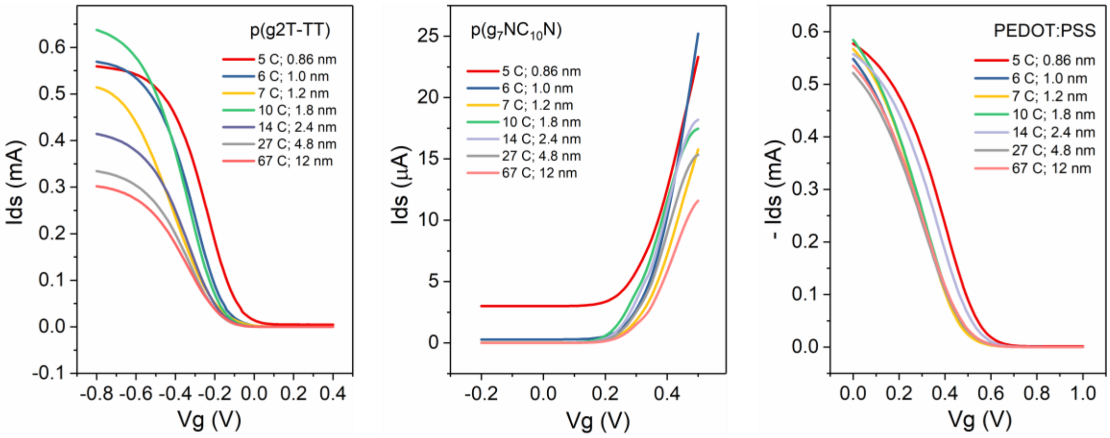

Figure 3.11 Transfer curves (in linear mode) of short-channel OECTs with three kinds of semiconductor polymers.

Figure 3.11 shows the transfer curves of OECTs in linear mode. It can be observed that the channel length has little influence on the channel current. For PEDOT:PSS devices, the on current and transconductance change little even if the channel length is increased by a factor of 10. Similarly, comparable levels of the channel on currents were also tested when changing the channel width. A 40 μm width bottom electrode was used to vary the channel width. The Al_2O_3 thickness is 2.4 nm to ensure a very low tunneling current. The AZ5214E channel windows were fabricated with 5, 10, 20, and 40 μm widths, which determines the channel width (Figure 3.12 a). Results show that the channel on currents of p(g2T-TT) and PEDOT:PSS devices have no fold change with a larger channel width (Figure 3.12 bc). One reason may be that the channel current is limited by parasitic resistance.

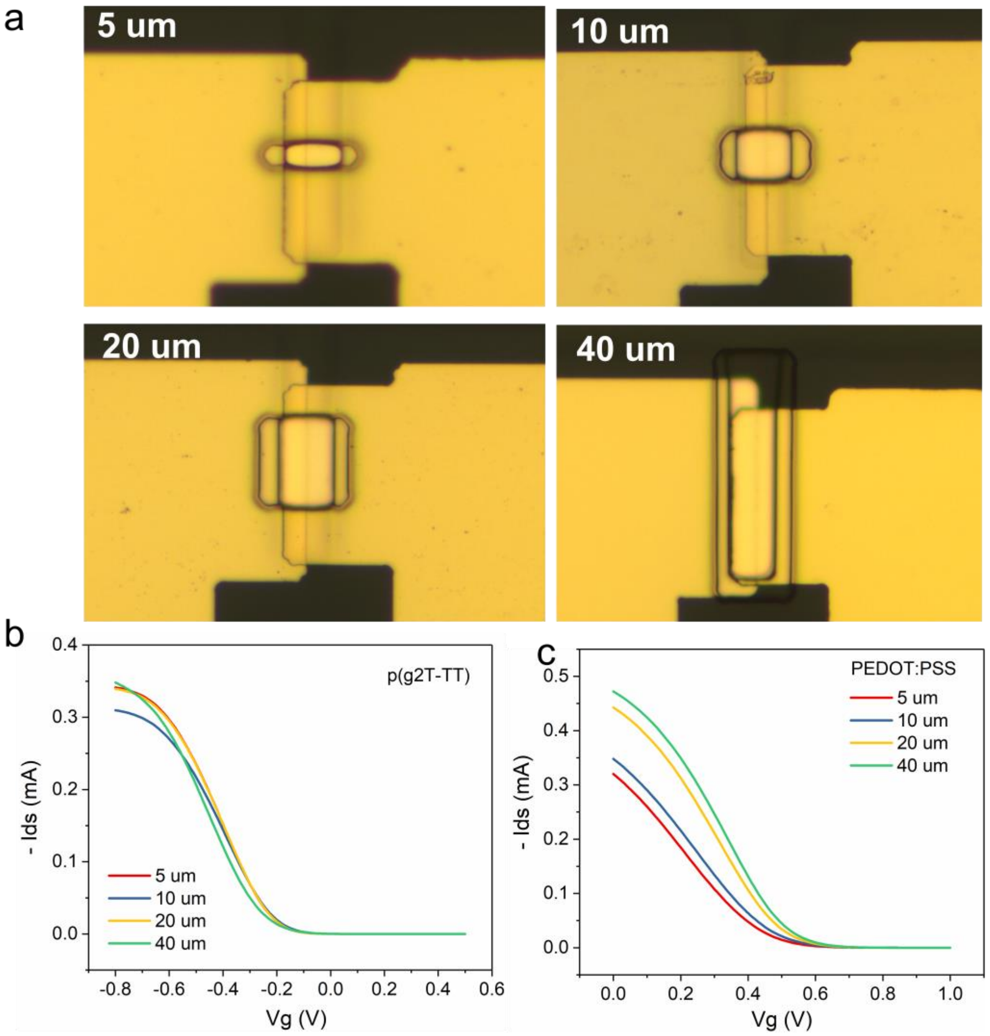

Figure 3.12 (a) Micrographs of OECT devices with different channel widths (5, 10, 20, and 40 μm). Transfer curves of (b) p(g2T-TT) devices and (c) PEDOT:PSS devices with different channel widths. Vd is -0.1 V, and channel length is 2.4 nm.

To decrease the parasitic resistance, the thickness of the Cr/Au electrodes was increased from 50 nm to 120 nm, and the parasitic resistance drops to around 50 ohms. Both the channel current and the transconductance are increased (Figure 3.13). Finally, the transconductance of p(g2T-TT) and PEDOT:PSS device can reach 19.8 mS (Vd = -0.6 V) and 19.1 mS (Vd = -0.8 V) respectively. High width-normalized transconductances about 3960 S/m are realized for both devices.

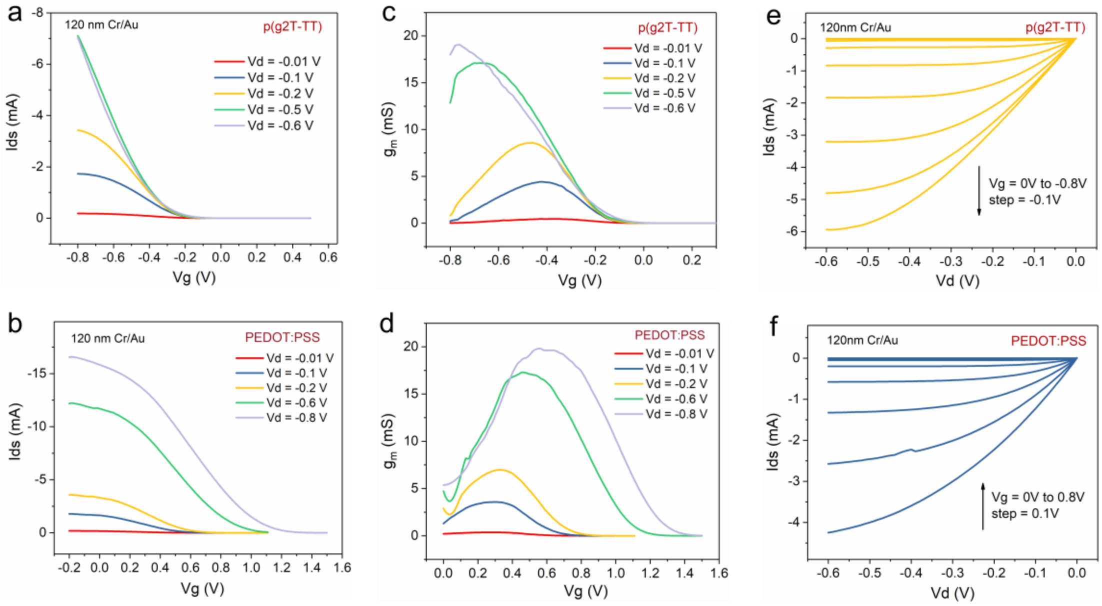

Figure 3.13 The transconductance of OECT devices with 120 nm thick Cr/Au electrodes. The transfer curves (ab), transconductance curves (cd), and output curves (ef) of p(g2T-TT) and PEDOT:PSS devices are shown.

3.3.4 Short-channel device stability

The vertical short-channel device stability was tested in 0.1 M NaCl electrolyte with long time gate voltage pulses. PEDOT:PSS device was tested over 2 hours with 1 second per cycle, Vg is 0.5 V/0 V pulse, Vd is -0.1 V. P(g2T-TT) device was tested 3 hours with 1 second per cycle, Vg is -0.5 V/0 V pulse, Vd is -0.1 V. P(g$_7$NC$_{10}$N) device was tested about 2 hours with 2 seconds per cycle, Vg is 0.5 V/0 V pulse, Vd is 0.1 V. The results (Figure 3.14) show that the short-channel vertical structure is stable, what makes difference is the stability of the conductive polymer. Two p-type OECT devices show better stability than n-type OECT devices.

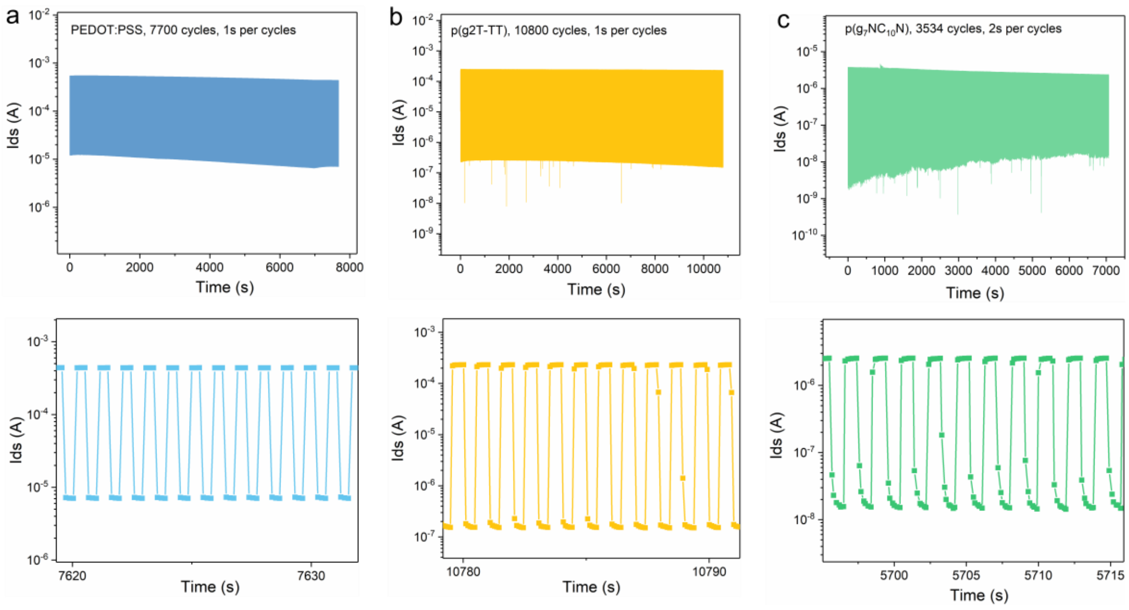

Figure 3.14 The stability of vertical short-channel OECTs.

3.4 Summary

By improving the fabrication strategies and adjusting the device parameters, high-performance short-channel vertical OECTs were realized. OECT device structure can overcome the short-channel effect and realize sub-1nm (0.86 nm) channel length. By reducing electrodes overlap area, the source drain tunneling current can be controlled in a small range even with 1 nm Al_2O_3 thickness. Both p-type and n-type short-channel OECTs can achieve on-off current ratios higher than 10^6 and ideal subthreshold slopes of 60 mV/dec. The transconductance of p(g2T-TT) and PEDOT:PSS devices are 19.8 mS and 19.1mS respectively, and the width-normalized transconductances are as high as 3960 S/m. The short-channel OECTs can maintain long-term stability under sustained voltage pulses. These good transistor performances were demonstrated for both p-type and n-type organic semiconductor materials.

Chapter 4 Fast response short-channel OECTs and its applications in electrophysiology recording and inverters.

The transient response is an important parameter in electronics and circuits, especially in high-frequency circuits. However, OECTs are knowns as slow response devices. In this chapter, the transient response of short-channel OECT is investigated by adjusting the channel geometric dimensions. High performances short-channel OECT was successfully applied in the monitoring of in vitro ECG and EOG. Complementary inverters with high gain and low power consumption were demonstrated.

4.1 Introduction

Transient response plays a crucial role in the development of high frequency bioelectronics. OECTs are slow devices, with time constants typically longer than 1 ms. Their slow switching speeds rely on the injection of ions into the conductive polymer, almost irrelevant with carries drift times along the channel. In Bernards model the transient behavior of OECTs includes the injection of cations from the electrolyte into the organic film and the removal of the holes at the source electrode.[37] In this model, the spatial variation of the voltage and the hole density are ignored. In the model established by Pushpa R. Paudel in 2022,[158] the case of asymmetrical distribution of channel carriers is supplemented, in which, the response of the channel current consists of two parts: the lateral ion moving and the vertical ion moving. In recent state-of-the-art works, [47,53,55] by changing the device structure and using additives in the active layer, the response time can be decreased to a few microseconds, but no faster than 1 microsecond yet.

Over the past few years, OECTs have experienced significant advancements in various applications such as high-performance transistors, bio-detection, electrophysiological signal recording, and neuromorphic devices.[98,100,101] The detection of electrophysiological signals can be used for monitoring the activity of organs or tissues, and disease diagnosis. Action potentials are generated when the cell membrane is stimulated, which can be transmitted through the tissue to the skin surface and recorded by instruments. In vivo signals (heart surface, muscle surface, and cerebral cortex) exhibit lower noise. Non-invasive in vitro detections are attenuated during transmission and are easily affected by non-target electrical signals. Physiological electrical assays such as EEG require fast-response devices to accurately record high-frequency signals. OECT has been applied to the detection of physiological signals on the body surface and in vivo, including EEG, ECG, EOG, EMG, and ECOG.[47] OECT is characterized by high transconductance, low operating voltages, and good biocompatibility. The structure of the OECT is very simple, making it possible for direct electrolyte-gated operation. The ultra-thin OECTs can be comfortably attached to the surface of tissues or organs and can monitor signals stably.[34]

As we have investigated in chapter 3, the use of oxide as a channel spacer in vertical OECTs allows for the reduction of the channel length to under 1 nm. Therefore, only the speed of ion doping/dedoping needs to be considered in transient response. In this chapter, we investigated the transient response of the short-channel vertical OECTs. By adjusting the area and thickness of organic semiconductor film, the transient response can be reduced to below 1 μs. Fast response, high transconductance OECTs are further applied in the monitoring of electrocardiogram (ECG) and electrooculogram (EOG). The low noise recording of the electrophysiology signals relies on the fast response speed and high current gain of short-channel OECTs. In addition, complementary inverters based on p-type and n-type OECTs were fabricated, which showed a recorded high static voltage gain of 456 V/V. The high voltage gain relies on the sharp subthreshold slopes and balanced electrical performance of p-type and n-type OECTs.

4.2 Experimental Section

4.2.1 Materials

AZ5214E photoresists, SU 8 photoresists were purchased from Microchemicals GmbH. Poly(3,4-ethylenedioxythiophene)−poly(styrenesulfonate) (PEDOT:PSS) (Clevios PH-1000) aqueous solution was purchased from Heraeus Ltd. Methylpyrrolidone, chloroform, dimethyl sulfoxide (DMSO), and glycerin were purchased from Sigma-Aldrich Co. GOPS [(3-glycidyloxypropyl)trimethoxysilane] was purchased from International Laboratory, USA. P(g2T-TT) and P($g_7NC_{10}N$) were synthesized by Iain McCulloch's group.[85,87]

4.2.2 Device fabrication

(1) Vertical short-channel OECT fabrication

The vertical short-channel transistor fabrication can be referred to the chapter 3. For the preparation of the PEDOT:PSS channel layer, Clevios PH-1000 was mixed with DMSO and glycerin (both with a volume ratio of 5%) for improving the stability and conductivity of channel layer. In addition, the GOPS cross-linker was added to prohibit PEDOT:PSS dissolution. The thickness of the channel film was adjusted by diluting the polymer solution. For p(g2T-TT) and p($g_7NC_{10}N$), they were diluted by chloroform. PEDOT:PSS was diluted by DI water without changing the concentration of additives. The channel length can be adjusted by the thickness of Al_2O_3. The gate channel distances are adjusted by the initial mask. The organic semiconductor areas were adjusted by patterned channel window areas.

(2) Fabrication process of complementary inverter.

The fabrication process of the complementary inverter is similar as single transistor device. Specifically (Figure 4.1), the first photolithography layer and sputtering were conducted for the bottom electrodes. The second layer was fabricated for the Ag/AgCl gate, and the third layer was fabricated for the top Cr/Au electrodes. After finishing the electrodes fabrication, SU-8 encapsulation, and channel window pattern, the polymers p(g2T-TT) and p($g_7NC_{10}N$) were spin coated on corresponding area. After baking at 110°C for 30 min, extra AZ5214 photoresist was lifted off. The polymer thickness was optimized to obtain well-matched transfer characteristics.

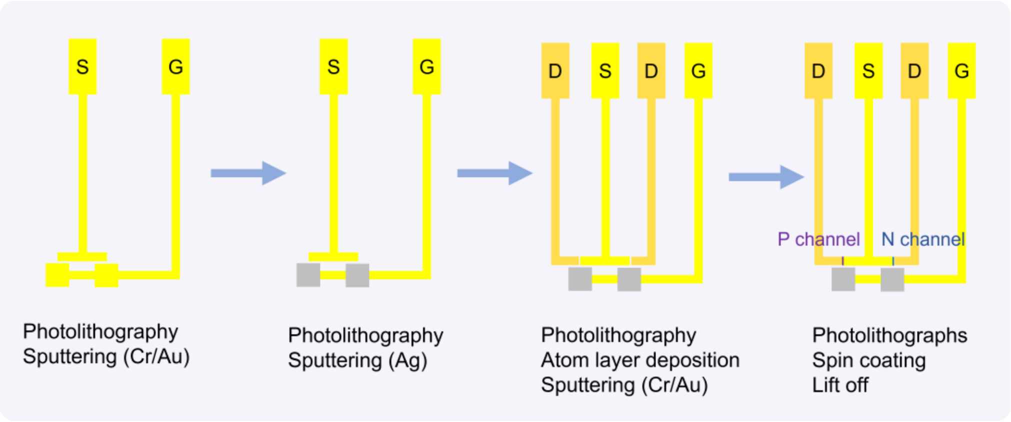

Figure 4.1 Fabrication process of OECT based complementary inverter.

4.2.3 Device characterization

(1) Electrical characterizations

The electric characteristic transfer curves of OECT devices and complementary inverters were tested by Keithley 4200A-SCS Parameter Analyzer. The response time of OECT devices was tested by an Agilent 33220A waveform generator (to apply gate voltage pulses), an SR570 low noise current preamplifier (to apply drain voltage), and a Tektronix TBS2072 digital storage oscilloscope (to convert the channel current into voltage signals). The transient response and AC amplification of inverters were tested by an Agilent 33220A waveform generator (to apply gate voltage), a Keithley 2400 source meter (to apply Vdd), and a Tektronix TBS2072 digital storage oscilloscope (to record output voltage). The thickness of polymer film was tested by Scanning Probe Microscope (Asylum MFP-3D Infinity).

(2) ECG and EOG recording

For ECG and EOG recording, the high transconductance and fast response PEDOT:PSS based devices were used. The gate voltage was applied by Keithley 2400 source meter. The human body is connected in series between the gate electrode and the Keithley 2400 source meter through two commercially available Ag/AgCl colloid electrodes. A SR570 low noise current preamplifier was used to provide a drain voltage and convert the channel current into voltage signals, which is further recorded by a Tektronix TBS2072 digital storage oscilloscope.

The waveforms of measured electrophysiology signals depend on the position of the two Ag/AgCl colloid electrodes. For ECG recording in this work, two electrodes were placed in a symmetrical position of the heart. The measured signals were filtered by a bandpass filter between 0.5 and 40 Hz. For EOG recording, two electrodes were placed on the outer corners of the eyes, or above and below the eyelids. The measured signals were filtered by a bandpass filter between 0.01 and 2 Hz.

4.3 Results and Discussion

4.3.1 Transient response of short-channel OECT

For short-channel device, it is necessary to consider whether the entire volume of polymer or only the part of the polymer near the channel affect the response speed. A schematic diagram of geometric dimensions of the short-channel OECT is shown as Figure 4.2. The Channel area A_c, channel thickness d_c, channel length L_c, and gate channel distance d_e are possible influencing factors of transient response time in short-channel OECTs. P(g2T-TT) based OECT was used to investigate the effects of geometric dimensions. The electrolyte for transient testing is 1M NaCl. It should be noted that this part of results only applies to OECT with channel lengths less than tens of nanometers, and it was not compared with long-channel (over 1 μm) devices.

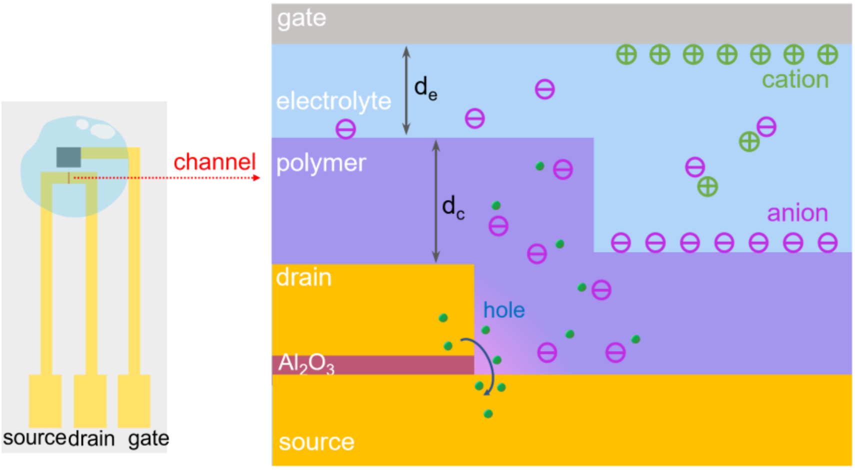

Figure 4.2 Schematic diagram of geometric dimensions of vertical short-channel OECT.

(1) Channel area factor

Firstly, devices with different channel areas A_c (5*20 μm^2, 10*20 μm^2, 20*20 μm^2, 60*20 μm^2) were fabricated, channel area images can be referred to Figure 3.12. Channel currents have no obvious variation with different channel widths. The channel length L_c is 2.4 nm, the channel thickness d_c is around 50 nm (2 mg/mL p(g2T-TT)), and the gate channel distance d_e is 30 μm. Figure 4.3 (a-d) shows the channel area dependent response time. The transient response of an OECT can be calculated by fitting an exponential to the drain current change upon the gate voltage. As the polymer area decreases, the response speed decreases obviously from 122 μs to 51 μs. Results indicate that the movement of the ions occurs throughout the whole polymer volume, not just in the area near the channel.

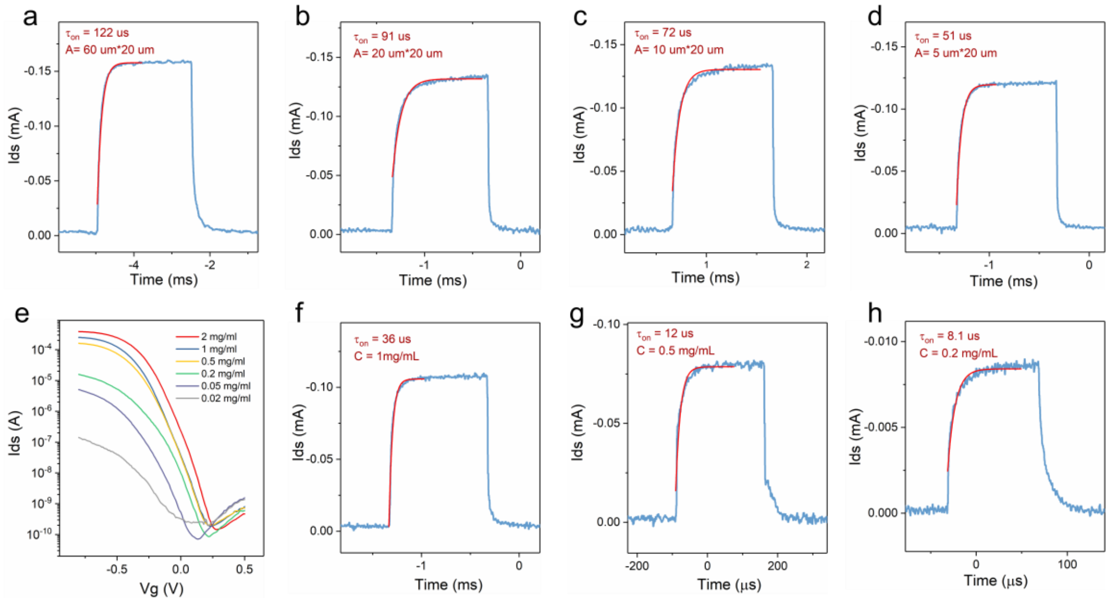

Figure 4.3 (a-d) The transient response of p(g2T-TT) OECTs with different channel areas. (e) Transfer curves of p(g2T-TT) devices with different polymer concentration. (f-h) The transient response of p(g2T-TT) OECTs with different channel thicknesses.

(2) Channel thickness factor

Secondly, the channel thickness was adjusted by different p(g2T-TT) concentration (2, 1, 0.5, 0.2 mg/mL). The channel area keeps 5*20 μm^2, the channel length keeps 2.4 nm, and the gate channel horizontal distance is 30 μm. Figure 4.3 e shows the transfer curves of p(g2T-TT) devices with different polymer concentrations. When the polymer concentration decreases from 2 mg/mL to 0.5 mg/mL, the channel current change little. When p(g2T-TT) further decreases to 0.2 mg/mL, the channel current decrease about an order of magnitude, but still have an over 10^5 on-off current ratio. Even if the concentration of polymer is diluted by a factor of 100, the gate voltage still retains its modulation capability. Short-channel vertical transistors can support thinner semiconductor films. The polymer thicknesses were tested by AFM, as shown in Figure 4.4. The channel thickness decreases rapidly as the polymer is diluted. The thickness of PEDOT:PSS and p(g2T-TT) was around 10 nm after diluting 4 times, and become discontinuous (around 3 nm) after diluting 100 times.

Transient response results were shown as Figure 4.3 (f-h). It is found that thinner film thickness can promote the transient response time, which means the ion doping still happen in whole polymer volume. Influences on response time caused by channel area and thickness were concluded in Figure 4.5a. Only when the ions and charge carriers of the whole volume polymer reach equilibrium, the device can reach steady state.

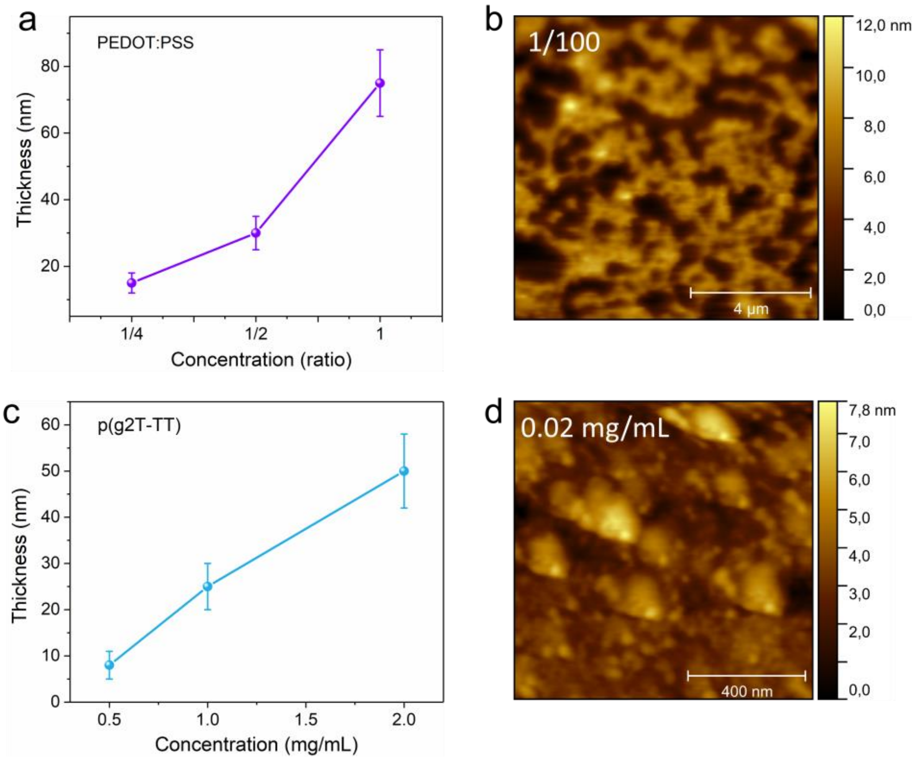

Figure 4.4 Thickness of (a) PEDOT:PSS film and (c) p(g2T-TT) film with different polymer concentrations. AFM images of (b) PEDOT:PSS film and (d) p(g2T-TT) film after dilution.

(3) Channel length and gate channel distance factors

On the other hand, the channel length was varied from 1.2 nm to 12 nm, and gate channel horizontal distance was varied from 30 μm to 0.5 mm. The polymer area keeps 5*20 μm^2, and the p(g2T-TT) concentration is 2 mg/mL. Test results are shown as Figure 4.5b, both two parameters have no obvious influence on transient response within the variation region. Reasons may be that the channel length is much shorter than the channel thickness, and the ion doping dedoping speed is slower than the carrier mobility. Therefore, when channel length scales down to nanometers, the channel length no longer affect the transient response time. As for the gate channel distance, the variation may not have much effect on electrolyte resistance.

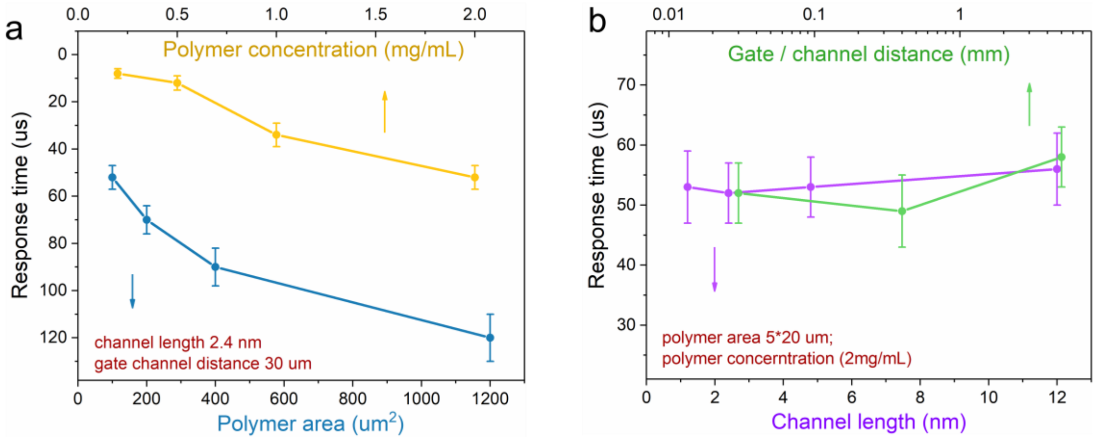

Figure 4.5 (a) Relationship between response time and channel area and channel thickness for p(g2T-TT) based OECTs. (b) Relationship between response time and channel length and gate channel distance for p(g2T-TT) based OECTs.

The response time of devices with three kinds of polymers was tested as shown in Figure 4.6(a-c). The polymer areas are 5*20 µm^2; channel length is 2.4 nm; electrolyte is 1 M NaCl; and the gate channel horizontal distance is 30 µm. P(g2T-TT) concentration is 0.2 mg/mL, PEDOT:PSS was diluted by 4 times without decreasing of channel current, and p(g$_7$NC$_{10}$N) (5 mg/mL) was not diluted for higher transconductance. The transient response time of PEDOT:PSS (0.97 µs) is much faster than p(g2T-TT) (7.6 µs) and p(g$_7$NC$_{10}$N) (0.32 ms). PEDOT:PSS device can get optimum performance because of the thin film thickness and the low capacitance. The comparison of transient response between short-channel OECT and other reported state of the art OECTs is shown in Figure 4.6(e,f). The short-channel OECTs are the record fast devices among both p-type and n-type OECTs.

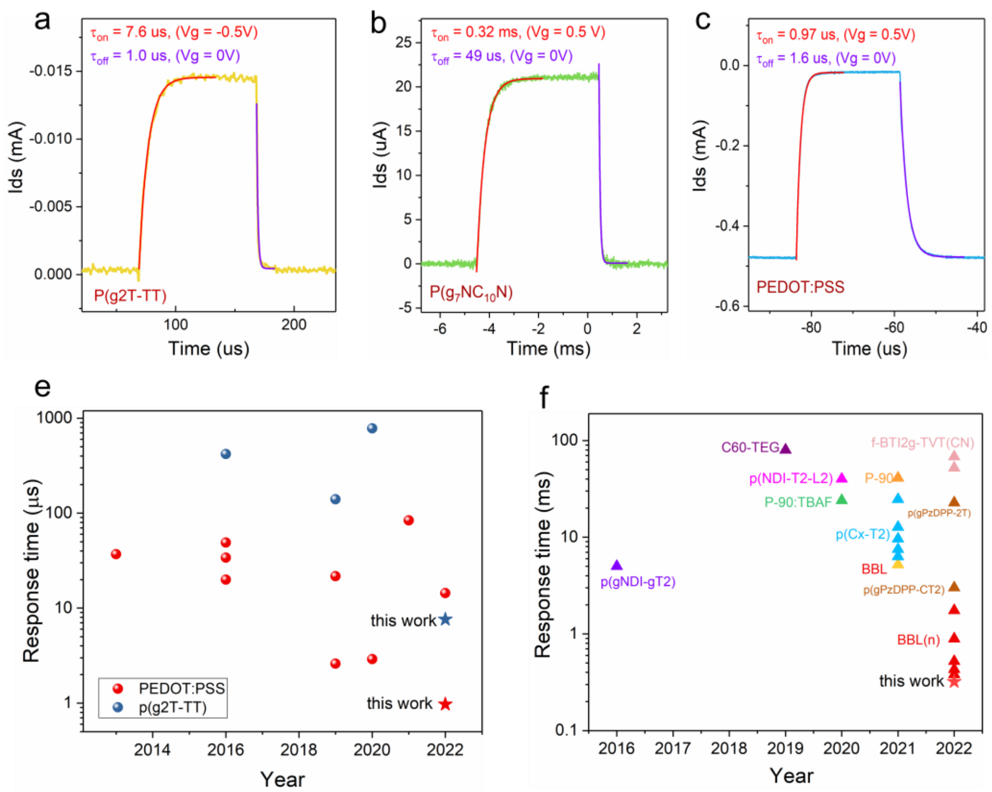

Figure 4.6 (a-c) Transient response of p(g2T-TT), p(g$_7$NC$_{10}$N), and PEDOT:PSS OECT devices. (e) Comparation of response time of PEDOT:PSS based, and p(g2T-TT) based OECTs in recent years.[34,47,52,53,87,159-161] (f) Comparation of response time of n-type OECTs in recent years, only devices faster than 100 ms were discussed.[56,81 69,72,73,76,79,92,96]

PEDOT:PSS OECT device can realize fast response speed less than 1 µs, and the response speed of p(g2T-TT) can be improved by an order of magnitude. P(g$_7$NC$_{10}$N) responds faster than other n-type polymers with even higher mobility.[56] In Bernards model[37] and Friedlein model[159], they show how to balance the gate voltage and drain voltage levels and minimize the response time of OECTs. This is also applicable to our transient response testing, and faster response time of 0.4 µs (Figure 4.7) is realized. When the channel voltage Vd is changed from negative to a positive voltage, Ids and Ig have the same current direction, which means the Ig response promotes the source drain current response speed. By setting the value of Vg or Vds, the source drain response speed can exceed the ionic speed.[159] Finally, Vd was set to +0.05 V, and the Vg pulse was set to 0.5 V / 0 V for PEDOT:PSS devices and to -0.5 V / 0 V for p(g2T-

TT) devices. The results are shown in Figure 4.7, which demonstrate that both the accumulation and depletion p-type OECT devices can achieve transient responses in the hundreds of nanoseconds range.

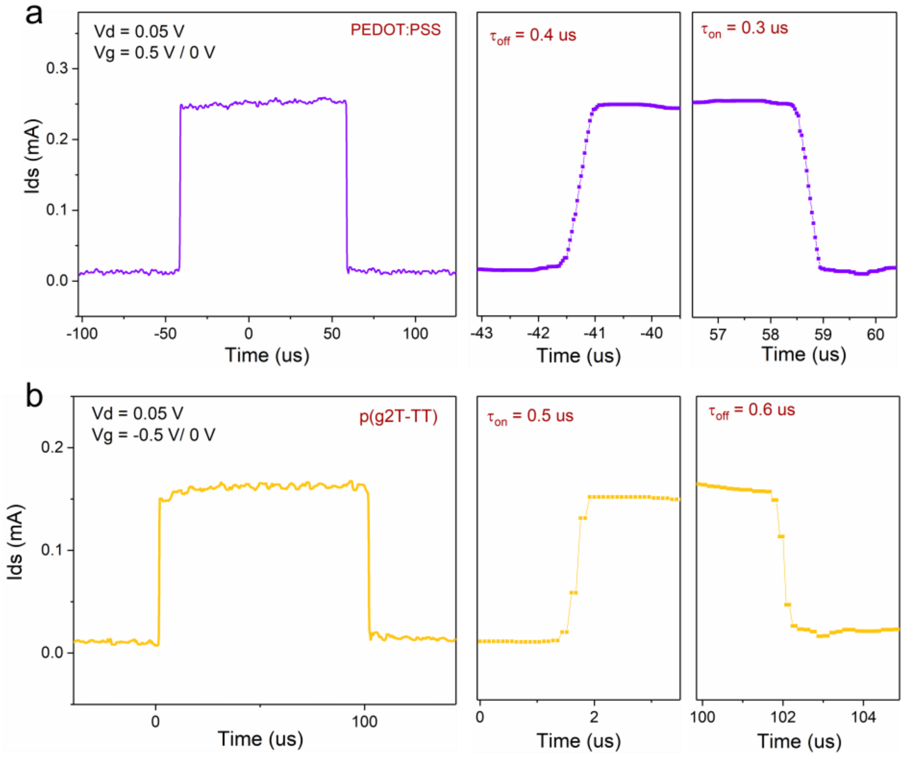

Figure 4.7 Gate voltage and channel voltage balanced response speed of (a) PEDOT:PSS and (b) p(g2T-TT) OECT devices.

4.3.2 ECG and EOG recording

(1) ECG recording

The active potential of cardiomyocytes can be transmitted to the skin surface, and recorded by equipment. By connecting the human body to the gate electrode, the active potential can induce the gate voltage variation, and further change the channel current. Transfer curve of PEDOT:PSS based short-channel OECT is shown as Figure 4.8a. For ECG recording, the gate voltage level is set at 0.35 V, which also corresponds to the value for maximum transconductance (1.3 mS). This choice is based on the fact that the gate voltage offset at this point can induce the largest variation in channel current. The device connection is shown as Figure 4.8b. The ECG signal is transmitted to the gate electrode, and the channel current variation is amplified by the current preamplifier and recorded by an oscilloscope.

Two gelatinous Ag/AgCl electrodes were positioned on the volunteer's right shoulder and left abdomen, with both electrodes being symmetrical to the heart. The waveform pattern changes depending on the specific location of the electrodes. The tested ECG is shown as Figure 4.8c, having typical waveforms of P wave, QRS complex and T wave. The heart beating period of the volunteer is 0.82 seconds (73 beats per minute), and the amplitude of the wave is around 0.8 mV. The ECG signals can be monitored for a long time by stable OECTs.

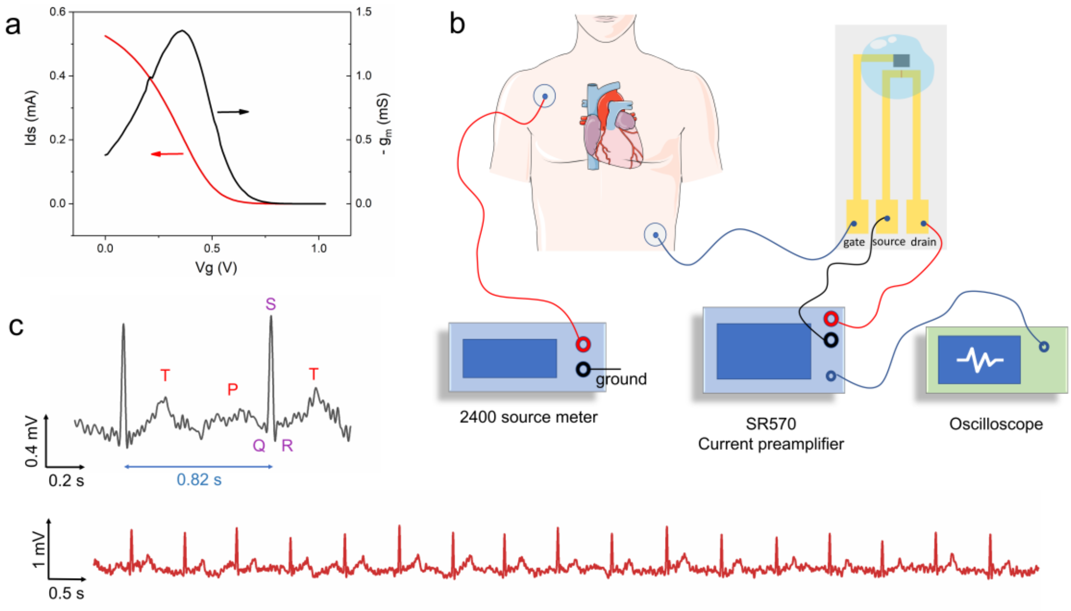

Figure 4.8 (a) Transfer curve and transconductance of PEDOT:PSS OECT device. (b) Scheme of the equipment connections and detection process of ECG recording. Vg = 0.35 V, Vd= 0.1 V, the electrolyte is 0.1 M NaCl. (c) A representative ECG waveform recorded by OECT, and longtime stable ECG monitoring.

(2) EOG recording

There is a resting potential across the retina, which changes during the eyeballs movement. Horizontal eyeballs movements can be recorded by placing electrodes in the outer corners of eyes. The up and down movement of the eyeballs can be recorded by placing electrodes above and below the eyelid. The tested EOG was shown as Figure 4.9. During the recording process, the volunteer moves their eyes in a straight-up-straight-down direction to record vertical potential changes, and in a straight-left-straight-right direction to record horizontal potential changes. According to the results, the potential changes are around 0.5 mV. This technique is useful for eye movement tracking. This technology can be applied not only in disease detection, but also in virtual reality and augmented reality.

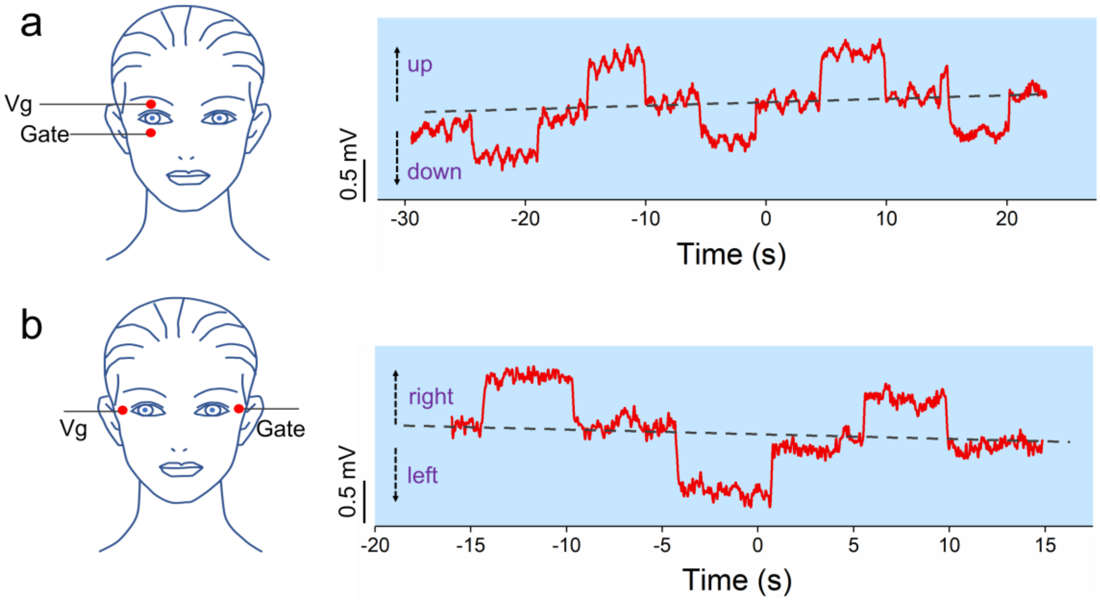

Figure 4.9 (a) Recording of the electrical activity during upward and downward movements of the eyeball. (b) Recording of the electrical activity during leftward and rightward movements of the eyeball.

4.3.3 OECT-based complementary inverter

An organic complementary circuit is built by p-type p(g2T-TT) OECT and n-type p($g_7NC_{10}N$) OECT. As the circuit diagram in Figure 4.10a, the drain electrode of the p-type OECT is connected to V_{DD}, while the source of the n-type OECT is connected to ground. Two OECTs share one Ag/AgCl gate immersed in 0.1M NaCl. To match the performance of the n-type OECTs, the thickness of p(g2T-TT) film was reduced to around 10 nm, getting a similar on current about 10 µA (Figure 4.10b). Transfer curves of two devices meets at Vd = 0.07 V, and the subthreshold slope is about 98 mV/dec for p(g2T-TT) device and 64.2 mV/dec for p($g_7NC_{10}N$) device. The channel on-off current ratio of both devices can reach 10^6-10^7. Because of the high and balanced devices performances, a record-high static voltage gain up to 456 V/V is achieved when Vdd is 0.6 V (Figure 4.10cd). The switching voltage (0.27 V) is close to the half of Vdd. Due to the low driving voltage of both OECTs, the complementary inverters show very low power consumption. The static power consumption (P_{static}) is below 0.5 nW with Vdd from 0.2 V to 0.5 V, and 1 nW at Vdd = 0.6 V. The dynamic power consumption ($P_{dynamic}$) increases from 9 nW (Vdd=0.2V) to 1.3 μW (Vdd = 0.6V) (Figure 4.10e). The parameters of reported electrolyte-gated transistor inverters were shown in Table 4.1. Only inverters with gain higher than 20 were discussed here. The inverter in this work can get highest gain at the lowest supplied voltage. P(g2T-TT) OECT has microseconds response time, therefore, the switching speed of the invert is mainly limited by the n-type OECT. The transient frequency results 1.5k HZ (Figure 4.10f), which is much higher than other inverters based on electrolyte-gated transistors.

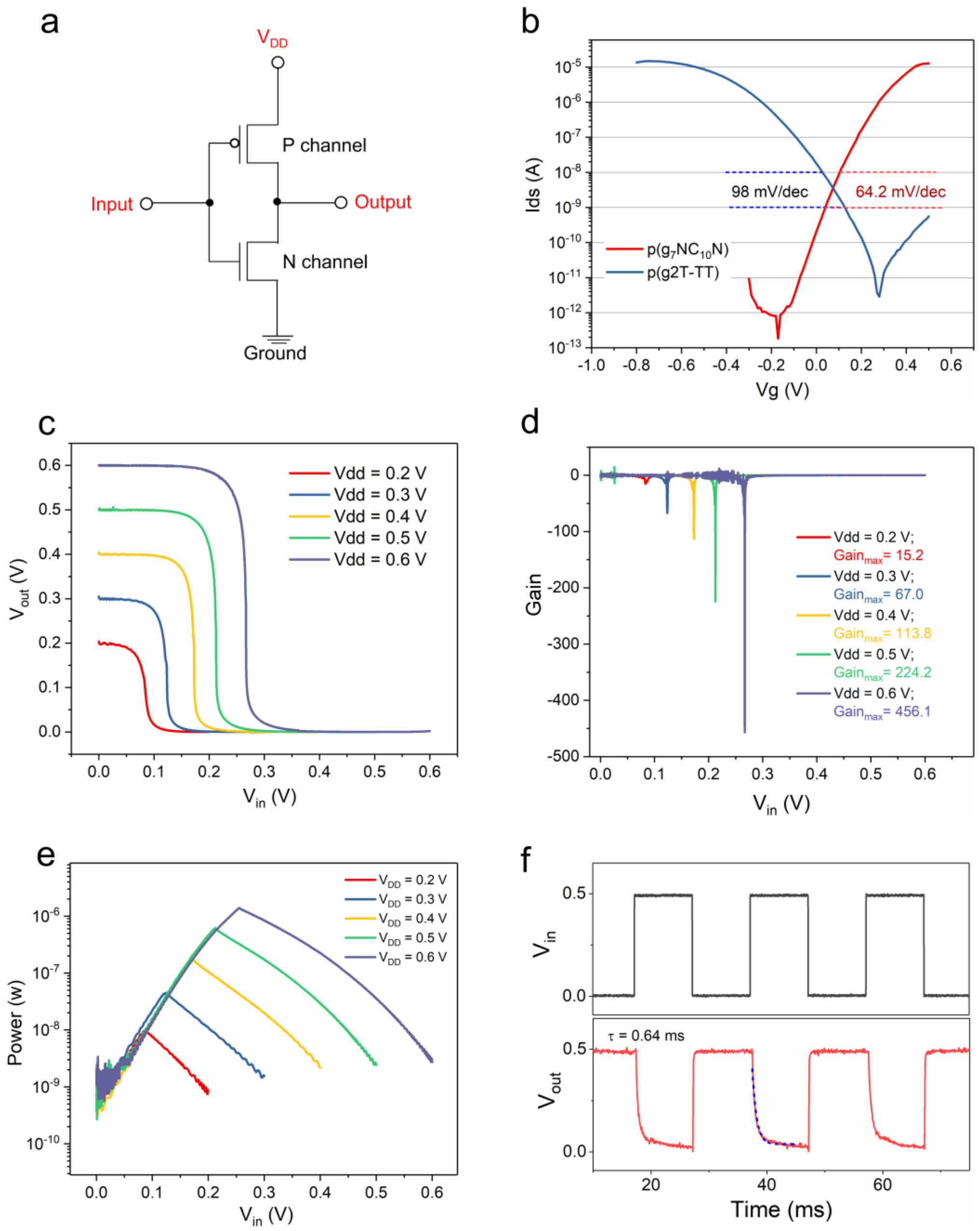

Figure 4.10 (a) Scheme of OECT-based complementary inverter. (b) Transfer curves of p-type p(g2T-TT) OECT and n-type p($g_7NC_{10}N$) OECT (Vd = 0.1 V). (c) Voltage transfer curves of the inverter with Vdd range from 0.2 V to 0.6 V, and (d) the corresponding voltage gain. (e) Power consumption of inverter under different Vdd. (f) The switching speed of the OECT-based inverter is 0.64 ms, with Vin being a 0.5 V/0 V pulse and Vdd set at 0.5 V.

OECT inverter can also be applied in alternating current amplification. The small amplitude of input voltage can induce large output voltage. Circuit scheme of the AC amplification is shown as Figure 4.11a. Vdd is 0.6 V, input voltage should be settled around the highest gain voltage. For this pair of OECTs, the Vin is a sinusoidal 10 mV AC voltage with an offset of 310 mV. The output signal is shown as Figure 4.11b with an amplitude of 352 mV and a dynamic voltage gain of 17.6 V/V.

The AC dynamic gain is Vdd independent, which is over than 20 V/V when Vdd is 0.7 V (Figure 4.11c). The AC gain is not as high as the static voltage gain in Figure 4.10. One reason for this is that the waveform generator's minimum output voltage (10 mV) is still significantly greater than the voltage sampling interval of the voltage transfer curve. Additionally, the AC gain is independent of frequency (Figure 4.11c). The Cut-off frequency is much small than DC signals.

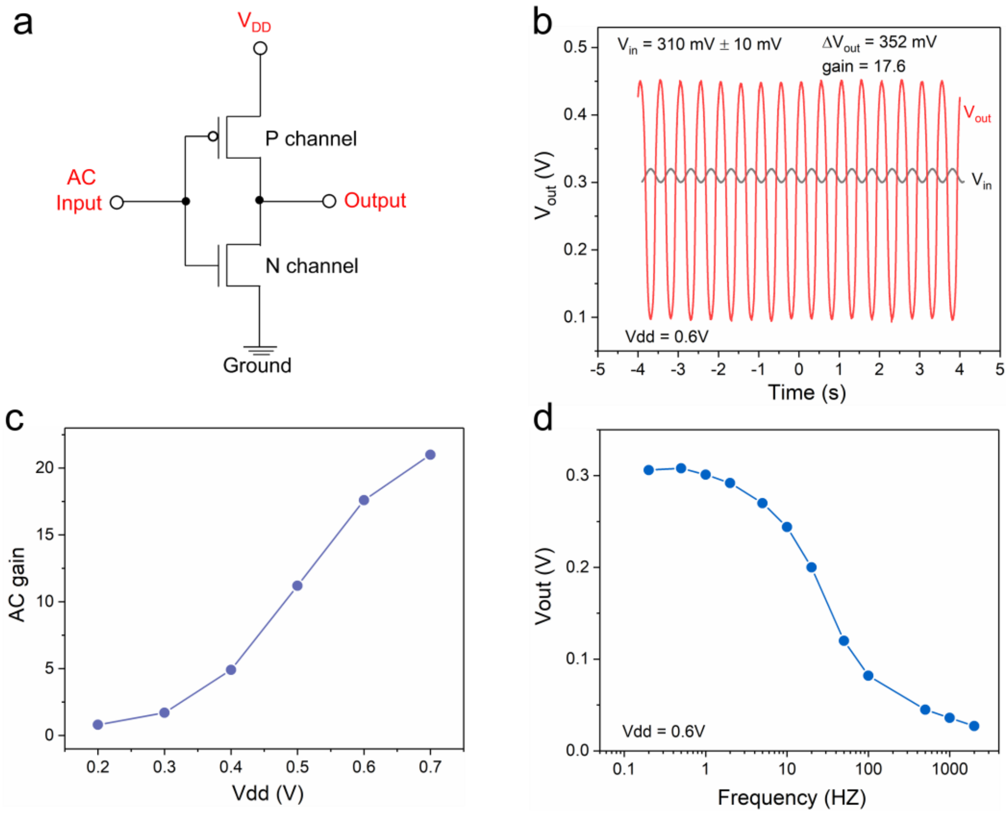

Figure 4.11 (a) Scheme of complementary inverter for AC signal amplification. (b) The inset shows a sinusoidal AC input (Vin is 10 mV with an offset of 310 mV at 2 Hz and Vdd is 0.6 V) and the corresponding amplified output. (c) The Vdd dependent voltage gain. (d) The frequency dependent output voltage amplitude (Vin is 10 mV).

Table 4.1 The parameters of electrolyte-gated inverters. Only inverters with voltage gain higher than 20 V/V are discussed here.

Transistor	Configuration	Channel material	Supply voltage (V)	Maximum gain	Static Power consumption	Dynamic power consumption	Year
OECT	Unipolar	PEDOT:PSS	0.8	26	/	/	2018[162]
OECT	Unipolar	Crys-P	0.8	107	/	/	2019[163]
OECT	Complementary	p(C_4-T_2-C_0-EG)	0.8	28	/	57.7 nW	2021[155]
OECT	Complementary	P($g_4$2T-T) BBL_{152}	0.7	100	2 nW	2.2 µW	2021[56]
OECT	Complementary	2DPP-OD-TEG	1.4	50	/	/	2021[74]
OECT	Complementary	P($g_4$2T-T) BBL	0.7	25	12 nW	2.7 µW	2022[164]
OECT	Complementary	P(g2T-TT) 2 TEG	0.6	25	/	/	2022[165]
OECT	Complementary	P(g2T-TT) p(g_7NC_{10}N)	0.6	456	1 nW	1.3 uW	This work
EG-FET	Complementary	CNT	1	20	/	/	2013[166]
EG-FET	Unipolar	ZnO	3	22	/	/	2019[167]
EG-FET	Unipolar	ZnO	2	60	/	/	2022[168]
EGT-hybrid	Complementary	(DPP-g2T) IGZO	0.7	113	15 nW	1.25 uW	2021[169]

4.4 Summary

In conclusion, adjusting the channel's geometric dimensions by reducing its area and thickness can reduce the response time to below 1 µs. However, even with this improvement, the n-type short-channel OECT still exhibits a slow transient response when compared to p-type OECTs. The fast-response short-channel OECT is used for skin surface ECG and EOG recording, as it is able to detect two types of electrophysiology with low noise. OECTs featuring high transconductance, ideal subthreshold slope, and fast response are also utilized in complementary inverters.

Inverter based on p-type p(g2T-TT) OECT and n-type p($g_7NC_{10}N$) OECT shows a record high static gain of 456 V/V when the Vdd is 0.6 V. The power consumption of inverter is as low as 1 nW, and the switching speed is 0.64 ms. AC signal can also be efficiently amplified with a voltage gain over 20 V/V. This high-performance short-channel OECT is very suitable for the application of electrophysiology recording and high gain circuits.

Chapter 5 Ultrafast, sensitive and portable detection of COVID-19 IgG using flexible organic electrochemical transistors

The outbreak of COVID-19 and its continued spread have seriously threatened the public health. Serologic assay is significant in infection diagnosis, seroepidemiological study and vaccine evaluation. However, convenient, fast and accurate antibody detection remain a challenge in this protracted fight. Here, we report an ultrafast, low cost, label-free and portable SARS-CoV-2 IgG detection platform based on organic electrochemical transistors (OECTs), which can be remotely controlled by a mobile phone. To enable a faster detection, voltage pulses are applied on the gate electrode of the OECT to accelerate the combination between the antibody and antigen. By optimizing the ion concentration and pH value of the test solutions, we can realize specific detections of SARS-CoV-2 IgG within several minutes with a detectable region from 10 fM to 100 nM in serum and saliva, which can cover those SARS-CoV-2 IgG concentrations of COVID-19 patients.

5.1 Introduction

Coronavirus disease 2019 (COVID-19) caused by severe acute respiratory syndrome coronavirus 2 (SARS-CoV-2) has been spreading globally since January 2020.[170] Even though massive efforts have been taken in the past one year, the spread of the virus remains severe in many countries. The COVID-19 has not only posed a great threat to global public health, but also caused enormous economic and social burdens on affected countries. Notably, rapid and accurate diagnosis of novel coronavirus infection plays an important role in choosing appropriate treatment methods, saving people's lives, and preventing virus transmission. At present, novel coronavirus diagnosis is mainly divided into ribonucleic acid (RNA) detection and antigen antibody detection.[171] Antibody testing plays an important role in COVID-19 in several aspects.[172] Firstly, it can be used to screen asymptomatic and RNA false-negative infections.[173,174] Secondly, it is useful in clinical health assessment.[175] Antibodies play an important role in neutralizing virus. People with low antibody levels have a risk of secondary infection, and severe patients with low levels of antibodies may be at a risk of death. Thirdly, antibody testing is important for vaccine development and evaluation.[176] In addition, it is also important for seroepidemiological study for analyzing the infection rate and population immunity rate in different areas [177,178].

At present, the detections of COVID-19 antibody mainly include enzyme-linked immunosorbent assay (ELISA)[179] and colloidal-gold lateral-flow immunoassays (LFIA)[180]. ELISA is highly accurate, while the operation process is complicated, making it difficult to achieve both portable and high-throughput detection. LFIA is easy to operate and portable, but with relatively low sensitivity, and prone to misdiagnosis. Therefore, for the detection of COVID-19 antibody, we need to develop a highly sensitive and rapid detection method, which can be easily operated for point-of care testing and large population screening. In addition to serum-based assays, SARS-CoV-2 IgG in saliva can be detected, which have advantages of noninvasive and self-collection. Because antibody concentration in human saliva is orders of magnitude lower than in serum, exquisite analytical sensitivity is needed.[181-183]

Organic electrochemical transistors (OECTs) have been recognized as high-performance transducers as well as amplifiers that can convert biological signals into electrical signals. OECT-based biosensors have the advantages of high sensitivity, low cost, easy fabrication and mechanical flexibility and are suitable for high throughput and multiplexing detections of biomarkers.[27,154,184]A typical OECT has a simple device structure that consists of three electrodes (gate, source, drain), an organic semiconductor channel between source and drain, and an electrolyte medium connecting the gate and the channel. The device has a low working voltage, good biocompatibility, and excellent stability in the electrolyte.[98] In recent years, OECTs have been successfully used in the detection of various biomolecules, including nucleic acids, proteins, metabolite, etc.[102,106,185] Here, we report OECT-based biosensors for the detection of SARS-CoV-2 IgG for the first time, which is controlled by a portable meter and a mobile phone through Bluetooth. SARS-CoV-2 spike protein is immobilized on the gate electrode through covalent binding, and SARS-CoV-2 IgG is bound with spike protein through antibody-antigen reaction during incubation, leading to a response of the device performance. Our device can detect SARS-CoV-2 IgG with an ultralow detection limit of 1 fM in aqueous solutions, and 10 fM in serum and saliva. The detection range in serum is from 10 fM to 100 nM with a good linear relationship, perfectly matching the serum specific IgG levels in COVID-19 patients. The ultralow detection limit in saliva can also satisfy the needs of exquisite analytical sensitivity.[181,182] To accelerate the testing process, we developed a novel technique by applying voltage pulses on the gate during incubation, which can decrease the incubation time of about 50%. Due to the rapid reaction of antigens and antibodies and the label-free approach, the whole test time can be completed within 5 min. Excellent selectivity of the devices for SARS-CoV-2 IgG detection is verified in our results.

5.2 Experimental Section

5.2.1 Materials

Dimethyl sulfoxide (DMSO), glycerin, N-(3-(dimethylamino)propyl)-N′-ethyl-carbodiimide hydrochloride (EDC), N-Hydroxysuccinimide (NHS), mercaptoacetic acid (MAA), bovine serum albumin (BSA), human serum IgG, hydrochloric acid (HCl), ethanolamine (MEA), human serum and phosphate buffered saline (PBS, pH 7.2) solution were all purchased from Sigma-Aldrich Co. SARS-CoV-2 spike protein (S1, His Tag; molecular weight: ~79 KD), and SARS-CoV-2 IgG (S1 RBD antibody, molecular weight: ~150 KD) were purchased from GenScript (Nanjing) Co.,Ltd. SU-8 photoresists, AZ5214 photoresists were purchased from Microchemicals GmbH. Poly(3,4-ethylenedioxythiophene)‒poly(styrenesulfonate) (PEDOT:PSS) (Clevios PH-1000) aqueous solution was purchased from Heraeus Ltd. (3-Glycidyloxypropyl) trimethoxysilane (GOPS) was purchased from International Laboratory, USA.

5.2.2 Device fabrication

The OECT device was fabricated by multilayer photolithography technology. After the first photoetching layer, Au electrode (Cr 10nm, Au 40 nm) was deposited by magnetron sputtering and the lift off process (Figure 5.1). The channel length (L) and width (W) of the devices were 30 and 120 μm respectively. Through a second layer of photoresist, the SU-8 photoresist was patterned and solidified on the Au electrode, acting as an insulating layer to protect the Au electrodes from the aqueous electrolyte. Finally, a channel window was opened by the third layer of photoresist. For preparation of the PEDOT:PSS channel layer, (Clevios PH-1000) was mixed with dimethyl sulfoxide (DMSO) and glycerin (both with a volume ratio of 5%) for improving the conductivity and stability of organic channel. In addition, the cross-linker (3-glycidyloxypropyl) trimethoxysilane (GOPS) was added to the above solution to prohibit PEDOT:PSS dissolution. PEDOT:PSS was then spin-coated on the patterned photoresist and annealed at 110 °C for 20 min. Another lift off process was conducted for removing the redundant PEDOT:PSS film.

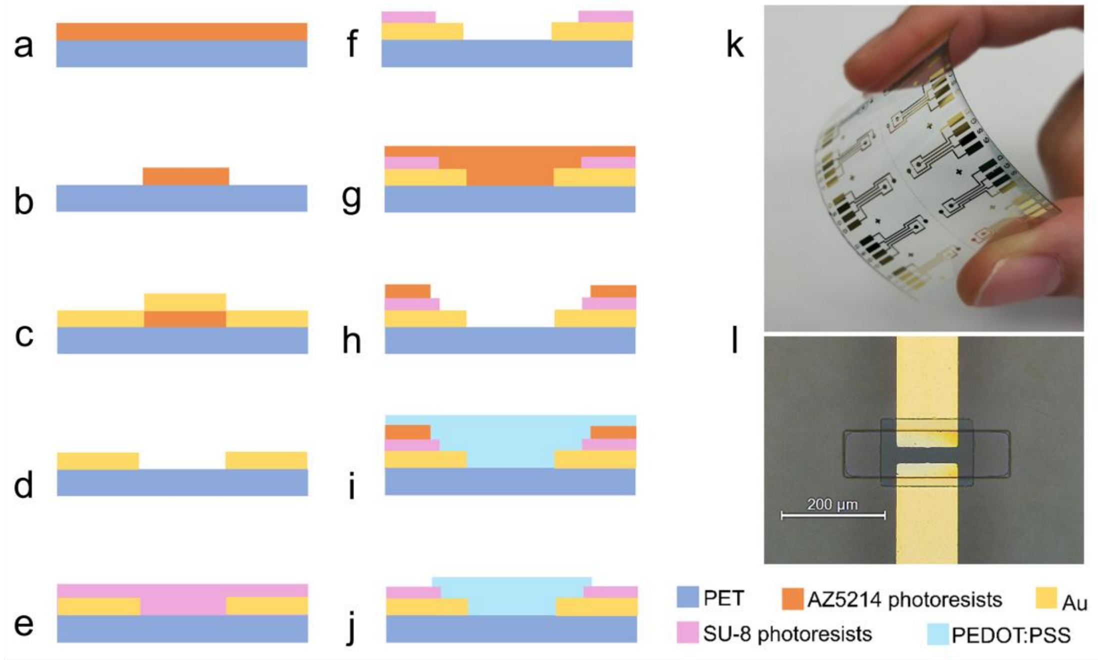

Figure 5.1 Device fabrication process. (a-d) Au electrodes deposition on PET substrate. (e-f) SU-8 photoresist as an insulating layer. (g-j) Patterning of PEDOT:PSS film between source and drain electrode. (k) Images of multiple devices on one PET substrate. (l) Microscope image of device channel.

5.2.3 Gate bio-functionalization

To get a clean gate electrode surface, Au electrodes (D = 0.6 mm) were treated with piranha solution (H_2O_2/H_2SO_4, V/V = 3/7) for 5 min, followed with a regular clean process. The cleaned gold electrode was immersed in the MAA (50 mM) solution in dark overnight to give carboxylic groups, which were activated afterwards in a mix-solution of EDC (20 mg/mL) and NHS (10 mg/mL) aqueous solution for 1 h at 25 °C. After immersing the gate electrode in SARS-CoV-2 spike protein solution (1 µM in 10 mM PBS solution, 2 µL) for 2 h at 25 °C, the antigen capturing SAM was formed by conjugation between the amine groups of the antigen and the activated carboxylic groups on the gate surface. Afterwards, the gates were treated with ethanolamine (MEA) (1 M, in 10 mM PBS solution) for one hour to eliminate the unreacted carboxylic groups. BSA solution (0.1 mg/mL) was further added for 1 hour to block the remaining nonspecific binding sites of the Au electrode. Finally, 5 µL SARS-CoV-2 IgG with a certain concentration (diluted by PBS/ serum/ saliva) was added to bind with SARS-

CoV-2 spike protein for several minutes at 25 °C. During the IgG incubation, voltage pulses were applied to accelerate the antigen antibody binding. After each step of the functionalization, the gate electrodes were rinsed thoroughly in water to remove possible residues.

5.2.4 Serum and saliva sample preparation

Serum sample was purchased from Sigma-Aldrich, which was from human male AB plasma, USA origin, sterile-filtered. Saliva sample was taking from a healthy female volunteer by putting a sterilized cotton ball underside of her tongue for 5 min. The saliva was squeezed from the cotton inside a syringe and injected into a sterile glass bottle. Then the saliva sample was diluted for 5 times by 10 mM PBS to decrease the viscosity for further use. For IgG detection in serum and saliva, 1 µM IgG in 10 mM PBS were serial diluted with serum and saliva, respectively.

5.2.5 Device characterization

The transfer characteristics of the devices were measured by a portable meter that is controlled by a mobile phone through Bluetooth. After each step of the immobilization, the gate electrodes were rinsed thoroughly in water, and tested in electrolyte. Transfer characteristics were taken with V_G = 0~1 V, V_{DS} = 0.05 V, and the relative change of the gate voltage ΔV_G was calculated after the antigen antibody reaction. Electrolyte with different concentrations were obtained by diluting the standard PBS solution with deionized water, and hydrochloric acid was added to adjust the pH value. The voltage pulses (frequency: 10^4 Hz, voltage: -0.5 V, pulse width: 10 µs, rise/fall time: 5 ns) was generated by a 20 MHz function/arbitrary waveform generator (Agilent 33220A). The atomic force microscopy (AFM) was taken by Scanning Probe Microscope (Bruker NanoScope 8). The Fourier transform infrared spectroscopy (FTIR) was taken by the Bruker Vertex-70 FTIR. Electrochemical impedance spectroscopy (EIS) measurements were carried out with a three-electrode system using a Zahner Zennium pro electrochemical workstation, with platinum gauze counter electrode, and Ag/AgCl reference electrode. The electrolyte is 10 mM PBS (pH = 7.2).

5.2.6 Design and fabrication of wireless portable meter

The meter can be divided into three main components (Figure 5.2), which include microcontroller, OECT-based sensor, and a Bluetooth transmission system. The meter can operate and read data from a mobile phone via Bluetooth. Details about the design of the portable meter can be found in supplementary materials.

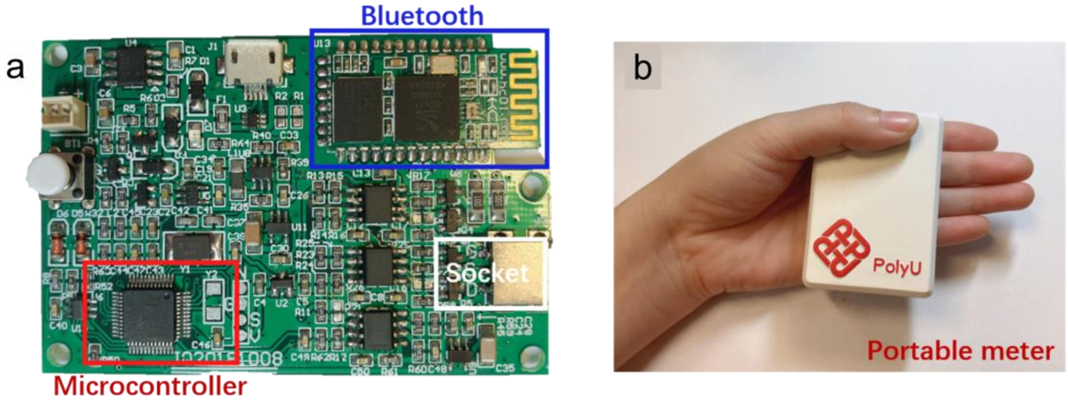

Figure 5.2 Photographs of the portable meter. (a) The circuit board of the detection system, including a microcontroller, a Bluetooth transmission component and a socket for the insertion of the OECT chip. (b) The appearance of portable meter in small size. The wireless portable IgG detection platform include a OECT-based sensor, a readout circuit and a user application program.[100] The readout circuit have a low-power microcontroller (STM8L152C6), a high performance DAC (MCU built in 12-bit DAC with output buffer), a ADC (16-bit ADC (ADS 1110) module via I2C communication). The circuit board was powered by 3.7 V lithium battery with power management module.

5.3 Results and Discussion

5.3.1 Design of the device and portable measurement system

OECTs are fabricated on a plastic PET substrate by photolithography (Figure 5.1), in which Au source, drain and gate electrodes are deposited by magnetron sputtering and an organic channel made of Poly(3,4-ethylenedioxythiophene)−poly(styrenesulfonate) (PEDOT:PSS) is prepared by spin coating.[186] The patterned PEDOT:PSS channel is between the source and drain electrodes and an insulating layer (SU8 photoresist) is in the left area for electrode encapsulation. The device is connected to a portable meter (Figure 5.3) that is controlled by a mobile phone through Bluetooth. The device performance is measured by dripping a small volume (5 µL) of aqueous solution (e.g. phosphate-buffered saline (PBS) solution) on the surface. Under optimum fabrication conditions, the device shows very stable performance in PBS solution and a fast response of channel current to a change of gate voltage (Figure 5.4).

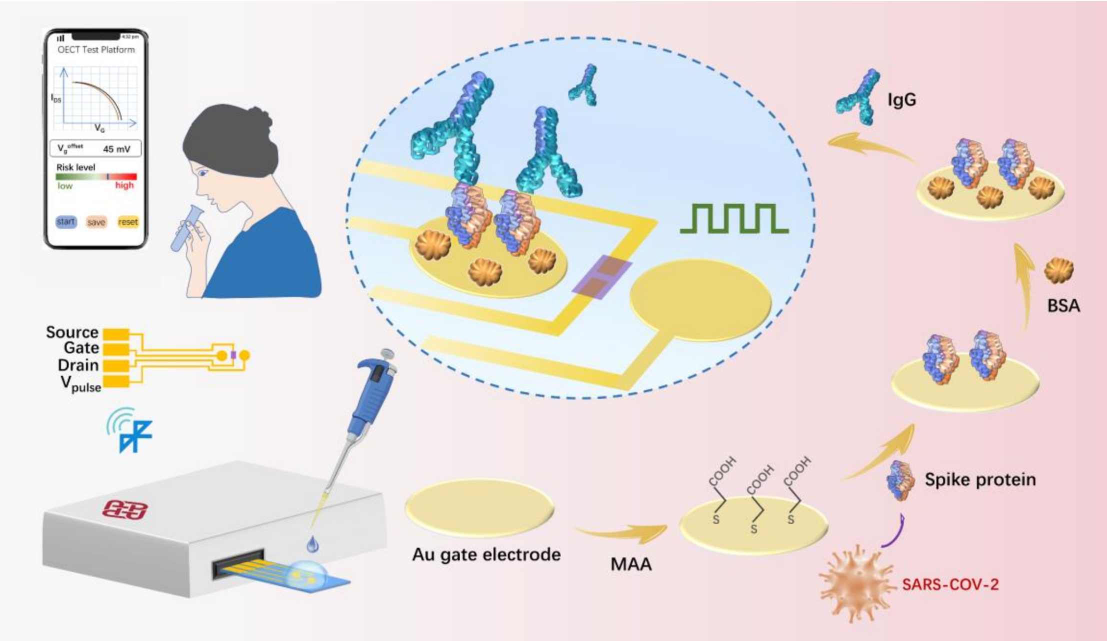

Figure 5.3 Scheme of the portable sensing system and the gate modification processes of the IgG sensor. The device is connected to a portable meter that is controlled by a mobile phone through Bluetooth. The biological modification on a gate electrode is carried out with several steps.

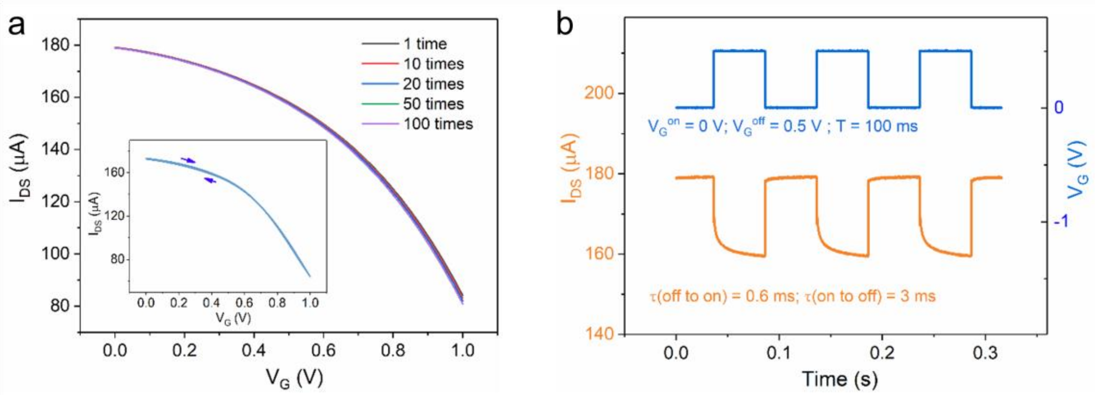

Figure 5.4 Stability and respond speed of OECT devices. (a) The transfer characteristics (I_{DS} versus V_G, V_{DS} = 0.05 V) of an OECT measured in a PBS solution after multiple tests. Inset is the forward to backward full sweep. (b) Transient response of an OECT measured in PBS solution, the response times of τ(off-to-on) and τ(on-to-off) are 0.6 ms and 3 ms respectively.

The Au gate can be conveniently modified with biomolecules on the surface and used for sensing SARS-CoV-2 IgG (Figure 5.3). The clean Au electrode is firstly modified with a chemical self-assembled monolayer (SAM) of mercaptoacetic acid (MAA) through gold–thiol binding.[187] After the chemical activation of the carboxylic groups, the antigen (SARS-CoV-2 spike protein) is conjugated to the chem-SAM layer through the covalent bond between carboxyl and amino group. Bovine serum albumin (BSA) is added afterwards to fill the vacancy left and minimize non-specific bindings. Subsequently, 5 μL solution of target SARS-CoV-2 IgG is incubated on the gate electrode for a certain period of time (≤30 min). The receptor-binding domain (RBD) of spike protein can specifically bind with SARS-CoV-2 IgG. The device is rinsed by deionized (DI) water after each step. Finally, the device is measured by the meter after dripping 5 μL electrolyte on the device surface. SARS-CoV-2 IgG solutions with different concentrations are tested with the OECT sensors to obtain the relationship between the device response and the IgG concentration.

Atomic force microscopy (AFM) was used to confirm effective antigen and antibody immobilization on the gate electrode (Figure 5.5). The stepwise modification images were presented with different image color bars for better observation (Figure 5.5 ab).

The Gaussian fits to the height histograms (Figure 5.5c) can visualize the gradual increase in height. Before the immobilization of spike protein, the gold gate electrode exhibits a smooth surface, and the root mean square (RMS) roughness is 0.32 nm. The height of the Au grains on the gate electrode is 1.87 ± 0.66 nm. After the immobilization of spike protein, massive particles can be observed on the surface of the gold electrode. The average size of the spike protein is 10-20 nm, and the feature height of particles after BSA blocking is 4.59 ± 1.75 nm. The RMS roughness is increased to 0.798 nm. Furthermore, with the binding of SARS-CoV-2 IgG to spike protein, a significant increase in particle size can be observed. The particle radius is 20-30 nm, and the RMS roughness is further increased to 0.885 nm. The height of protein particles is increased to 8.17 ± 1.77 nm, verifying the binding of antibody with antigen. The height of antigen and antibody complex is around 6.3 nm, which is similar with those previously reported.[188,189]

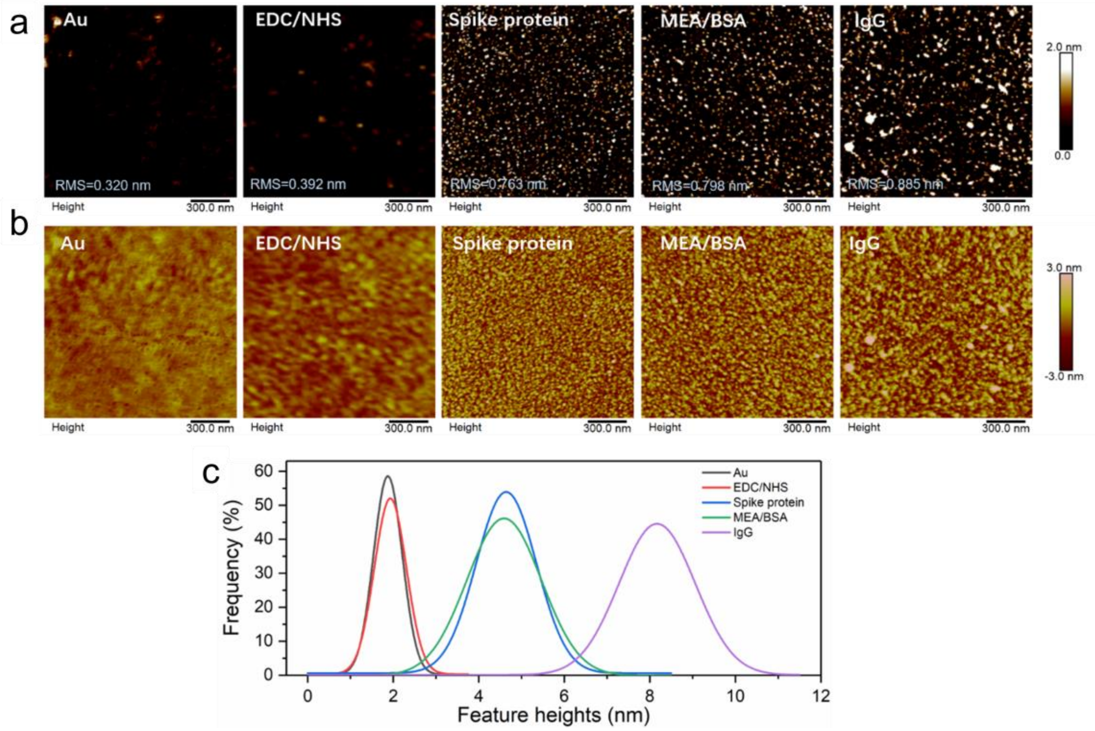

Figure 5.5 (a, b)AFM images of the Au gate electrode after step by step modifications. (c) The gaussian fits of the height histograms after stepwise modification. (a) and (b) are same images with different color scales.

The successful immobilization of protein on the gate surface is also confirmed by

Fourier transform infrared spectroscopy (FTIR) (Figure 5.6). Two prominent vibrational bands of the protein backbone can be observed after the immobilization of antigen and antibody.[190,191] Figure 5.6 shows the Fourier transform infrared spectroscopy (FTIR) test result before and after the protein immobilization. A control experiment was conducted through immobilize a high density of BSA film. Compared with the transmission spectrum of Au film, there were two distinct vibrational bands around 1657 cm^{-1} and 1548 cm^{-1} after the immobilization of spike protein. The two bands correspond to the amide I (1600−1690 cm^{-1}) and amide II (1480−1575 cm^{-1}) bands, which are the two prominent vibrational bands of the protein backbone.[190,191] The amide I band is attribute to the C=O stretch vibrations of the peptide linkages, and the amide II band is mainly caused by N-H and C-N stretching vibration.[191] After further immobilization of BSA and SARS-CoV-2 IgG, two prominent vibrational bands were retained and slightly enhanced. Because the quantity of antigens and antibodies immobilized on the gate electrode were much less than that of the BSA film, the peak intensity of antigens and antibodies is not as obvious as the BSA film, but the positions of the two are consistent. Peaks between 2000 cm^{-1} and 2500 cm^{-1} are caused by background noise. The peak around 2350 cm^{-1} is caused by carbon dioxide.

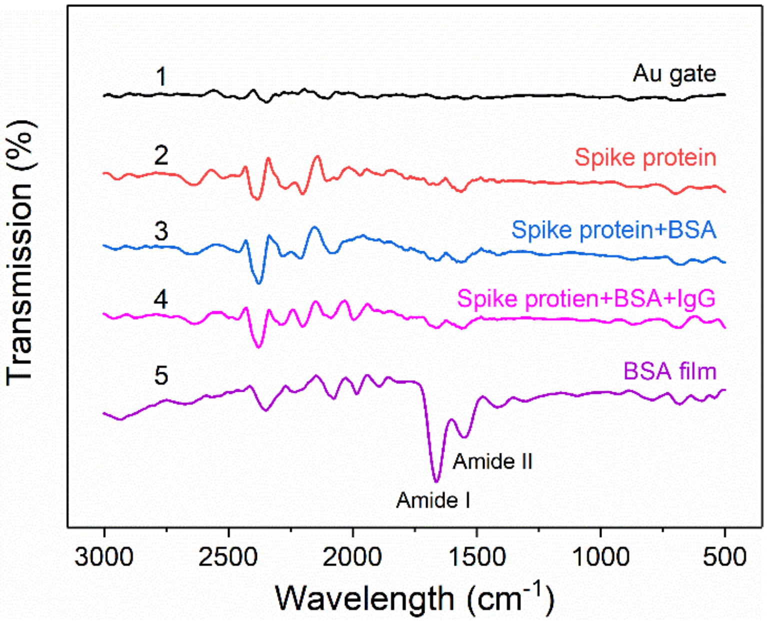

Figure 5.6 Fourier Transform Infrared Spectroscopy (FTIR) of the gate electrodes. Transmittance spectrum of clean Au gate (line 1); Au gate with spike protein (line 2);

Au gate with spike protein and BSA (line 3); Au gate with spike protein, BSA and IgG (line 4); and Au gate with BSA film in high density (line 5) are shown.

5.3.2 SARS-CoV-2 IgG detection

The detection process of IgG includes the following three steps. (1) To incubate IgG solution on the gate modified with spike protein for a certain period of time. (2) To remove IgG solution and physically absorbed biomolecules on the gate by rinsing DI water. (3) To characterize the device performance in a separate electrolyte. The electrolyte properties such as the ion concentration and pH values can be optimized to get the biggest device response. Transfer curves (I_{DS} vs V_G) of OECTs are tested before and after the immobilization of SARS-CoV-2 IgG (Figure 5.7a). At the beginning, the electrolyte used for testing is 10 mM PBS solution with a pH value of 7.2, which is regarded as the commonly used test environment. With the increase of SARS-CoV-2 IgG concentration, the transfer curves gradually shift towards more negative gate voltages. The inset is the enlarged graph of the transfer curves. 72 mV gate voltage shift ΔV_G is observed with 100 nM SARS-CoV-2 IgG incubated on the gate electrode for 10 minutes. The detection limit is 10 pM, corresponding to a gate voltage shift ΔV_G of 12 mV (Figure 5.7b). The voltage shift can meet the requirement of signal to noise ratio (S/N) higher than 3 for the detection limit.[192] All tests were repeated at least three times.

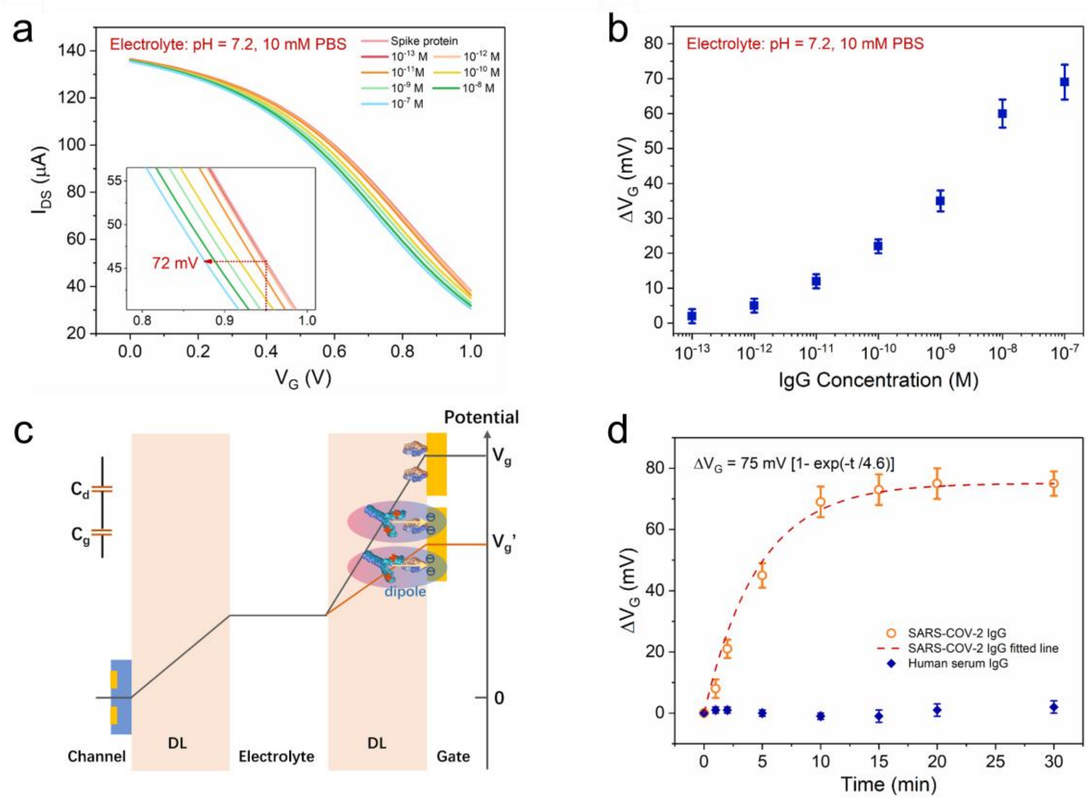

Figure 5.7 Detection of SARS-CoV-2 IgG using OECTs operated in PBS solution. (a) The transfer characteristics of OECTs after incubation of SARS-CoV-2 IgG solutions with different concentrations in sequence. (b) Relative change of the gate voltage ΔV_G as a function of IgG concentration. (c) Schematic diagram for protein dipole and potential drops in the two double layers. (d) Relative change of the gate voltage ΔV_G as a function of incubation time. (All tests were conducted in electrolyte: 10 mM PBS, pH = 7.2)

Proteins are made up of zwitterionic amino acid compounds, which can be positively or negatively charged depending on the isoelectric point (pI) and pH value of the electrolyte.[193] The SARS-CoV-2 IgG is positively charged in PBS solution (pH = 7.2) since its isoelectric point is calculated to be 8.2 by on-line bioinformatics resource Expasy. The surface potential of the gate electrode can be influenced by charged molecules and change the effective gate voltage of the transistor. The positive charge of protein induces an electric dipole and a potential barrier across the electric double layer (EDL) on the gate/electrolyte interface (Figure 5.7c).

The channel current I_{DS} of an OECT is given by the following equations: [37]

$$I_{DS} = \frac{W\mu C_i}{L}\left(V_P - V_g^{eff} + \frac{V_{DS}}{2}\right)V_{DS} \quad (when\ |V_{DS}| \ll |V_p - V_g^{eff}|)$$

$$V_P = qp_0\, t/C_i$$

$$V_{\mathrm{g}}^{eff} = V_G + V_{\mathrm{offset}} \quad , \tag{5.1}$$

where W is the channel width, L the channel length, μ the hole mobility, C_i the effective capacitance per unit area of the transistor, V_p the pinch-off voltage, V_g^{eff} the effective gate voltage, q electronic charge, p_0 the initial hole density in the organic semiconductor before the application of a gate voltage, t the thickness of the organic semiconductor film, and V_{offset} is the offset voltage related to the potential drop at the two EDL interfaces.[194] C_i is equal to the total capacitance of the two interfacial capacitors connected in series, which is given by:[194]

$$C_i = \frac{C_g C_d}{(C_g + C_d)S} \quad , \tag{5.2}$$

where C_d and C_g are the capacitances of the interfaces between the electrolyte and PEDOT:PSS and between the electrolyte and Au gate, respectively. S is the area of active layer.

After the immobilization of SARS-CoV-2 IgG on the gate surface, an electric dipole is formed on the gate surface. The induced potential change on the Au gate electrode can be expressed by[195]:

$$\Delta\varphi = \frac{nQ_{IgG}}{\varepsilon_0 \varepsilon_r} t_{IgG} \quad , \tag{5.3}$$

where n is the coverage of protein molecules on the surface of gate electrode, which is related to the concentration SARS-CoV-2 IgG; Q_{IgG} is the net charge for one IgG molecule, which is related to the pH value of the test environment; ε_0 is the dielectric permittivity of the free space; ε_r is the relative dielectric constant of IgG layer; and t_{IgG} is the effective interaction thickness related to the Debye length in the electrolyte, which will be discussed later. Thus, the positively charged protein on the gate surface can change the surface potential of the Au gate, leading to a shift of the transfer curve to a lower gate voltage.

The immobilization of SARS-CoV-2 IgG on the gate electrode shows little effect on the capacitance of the gate electrode C_g (Figure 5.8). The typical dielectric constant ε_r of a protein is about 3[196], and the total height of antigen and antibody (d) is around 6.3 nm (Figure 5.5). According to $C = \varepsilon_r\varepsilon_0/d$, the capacitance of protein layer is around 0.42 μF/cm^2 if the electrode is fully covered with the protein. However, the actual value of the gate capacitance is much higher than that of a pure protein layer, indicating that the gate capacitance is mainly determined by the EDL and SAM layer on the Au gate surface.

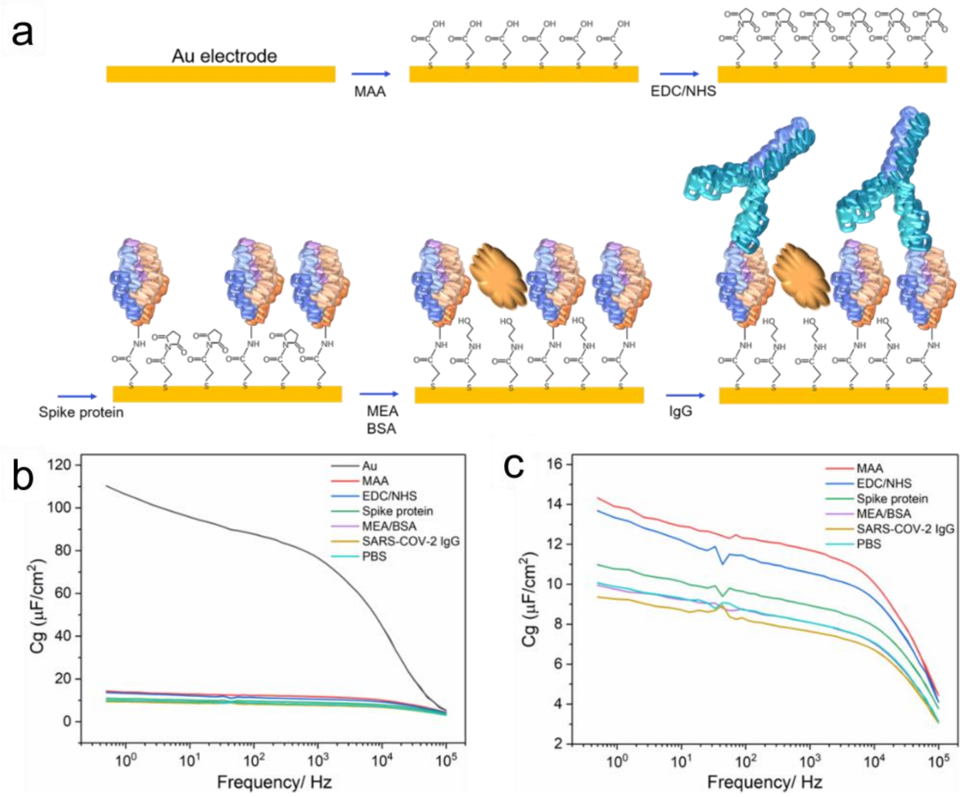

Figure 5.8 Frequency dependent capacitances of an Au gate electrodes after stepwise modifications. (a) Scheme of the detail gate electrode modification process. (b) The capacitance variation of gate electrodes after reactions with chemicals and biomolecules. (c) The detail of Figure 5.8a. SARS-CoV-2 IgG (100 nM) was incubated for 10 minutes on gate electrode after previous modification. The last curve (PBS) means that PBS was incubated for 10 minutes on the gate electrode after previous modification.

Rapid detection is very important in the diagnosis of COVID-19 for continuous large numbers of infections.[197] Notably, the devices are label-free and can be measured very quickly with a portable meter, thus the test time is mainly limited by the incubation time of IgG on the sensor. Hence, we have tried to optimize the incubation time in the following experiments. SARS-CoV-2 IgG solution with a concentration of 100 nM was dripped on the gate area for a certain period of time for incubation and then the transfer curve of the device was measured in 10 mM PBS. This process on the same device was repeated for several times and the device performance as a function of accumulated incubation periods was obtained (Figure 5.9). Therefore, we can obtain the correlation between the gate voltage shift ΔV_G of the device and incubation periods (Figure 5.7d). The offset of the transfer characteristic gradually increases, and a significant response can be found even after 2 min incubation. The relationship can be fitted with an exponential function $\Delta V_G = A[1-\exp(-t/\tau)]$, where $\tau = 4.6$ min is a time constant and $A = 75$ mV is the saturation value of ΔV_G. Notably, the response of the device can reach 89% of the maximum shift after 10 min incubation and saturate after 20 min.

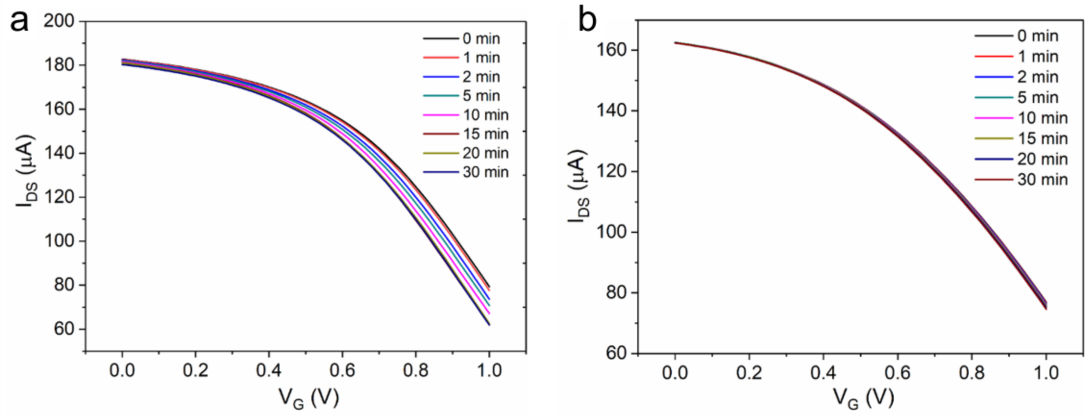

Figure 5.9 The transfer characteristics after the incubation of IgG (100 nM) with different periods. (a) SARS-CoV-2 IgG, and (b) Human serum IgG are demonstrated respectively. (Electrolyte: 10 mM PBS, pH = 7.2).

To confirm the specificity of the sensor in detecting SARS-CoV-2 IgG, IgG purified from normal human serum was tested with the same condition (Figure 5.10). The transfer curve of the device shows negligible shift after incubation in the human serum IgG for 10 min while an obvious shift induced by SARS-CoV-2 IgG can be found at the same measurement condition (Figure 5.10a). The incubation of the sensor in pure BSA solution did not lead to any response in its transfer curve, indicating an excellent stability of the device in the aqueous solutions. In addition, the device was tested in the normal human serum IgG solution with different incubation periods and no obvious signal was observed in the whole region, indicating excellent selectivity of the device (Figure 5.7d). Furthermore, different concentrations of SARS-CoV-2 IgG mixed with 100 nM human serum IgG were tested by the device (Figure 5.10b). The device response to the SARS-CoV-2 IgG was not influenced by the serum IgG, indicating that the device could selectively detect the target antibody without any interference from other antibodies from serum.

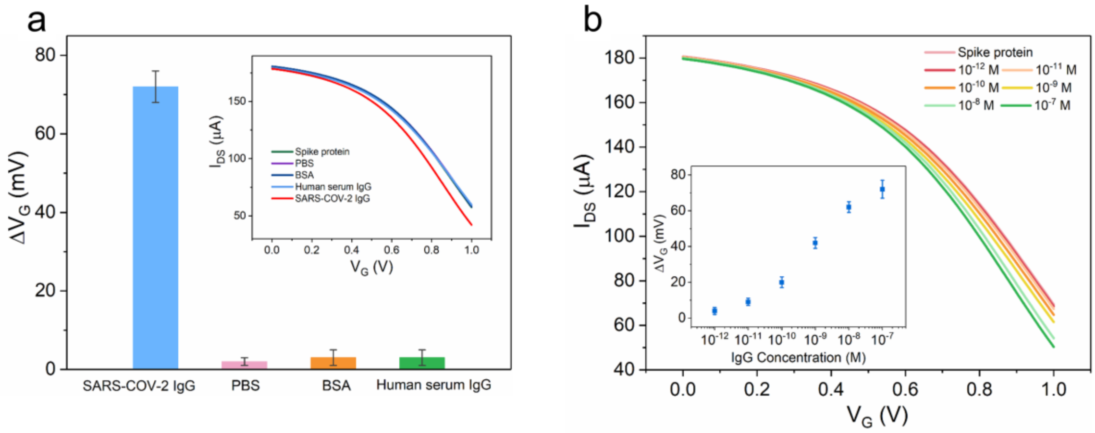

Figure 5.10 The selectivity of OECT-based SARS-CoV-2 IgG biosensor. (Electrolyte: 10 mM PBS, pH = 7.2). (a) The gate voltage shifts (ΔV_G) after incubations in SARS-CoV-2 IgG (100 nM), PBS, BSA (0.1 mg/mL), and human serum IgG (100 nM) solutions. The inset is the corresponding transfer curves. (b) The transfer curves after incubations of different concentrations of SARS-CoV-2 IgG together with 100 nM human serum IgG. Inset is the gate voltage shifting ΔV_G as a function of SARS-CoV-2 IgG concentration.

5.3.3 Sensitivity enhancement by increasing Debye length

In an electrolyte, a positively charged protein is surrounded by anions due to electrostatic interaction and its surface charge can be screened within the Debye length of the EDL.[198] Therefore, a protein with a distance to the gate longer than the Debye length should have little influence on the gate potential. Consequently, the Debye length, which is related to the ion concentration of an electrolyte, will dramatically influence the performance of our IgG sensor. The Debye length in an electrolyte solution is given by:[199]

$$\lambda_D = \sqrt{\frac{\varepsilon k T}{2 N_A q^2 I}} \quad , \qquad (5.4)$$

where ε is the absolute permittivity of the electrolyte, k is Boltzmann's constant, T is the temperature, N_A is Avogadro's number, and I is the ionic strength of the solution.

To test the effect of Debye length on the device performance, the PBS electrolyte was diluted at different concentrations (10 mM, 1 mM, 100 μM, 10 μM and 1 μM) and used in the detections of SARS-CoV-2 IgG. The shifts of the transfer curves measured in 10 μM PBS (Figure 5.11a) are more pronounced in comparison with the responses obtained in 10 mM PBS solution. Notably, the maximum gate voltage offset ΔV_G corresponding to 100 nM IgG is increased from 72 mV to 127 mV. Figure 5.11b shows the shifts of the transfer curves induced by IgG measured in PBS solutions with different concentrations. With the decrease of PBS concentration, the sensitivity of the IgG sensors gradually increases, and the detection limit is decreased from 10 pM to 100 fM.

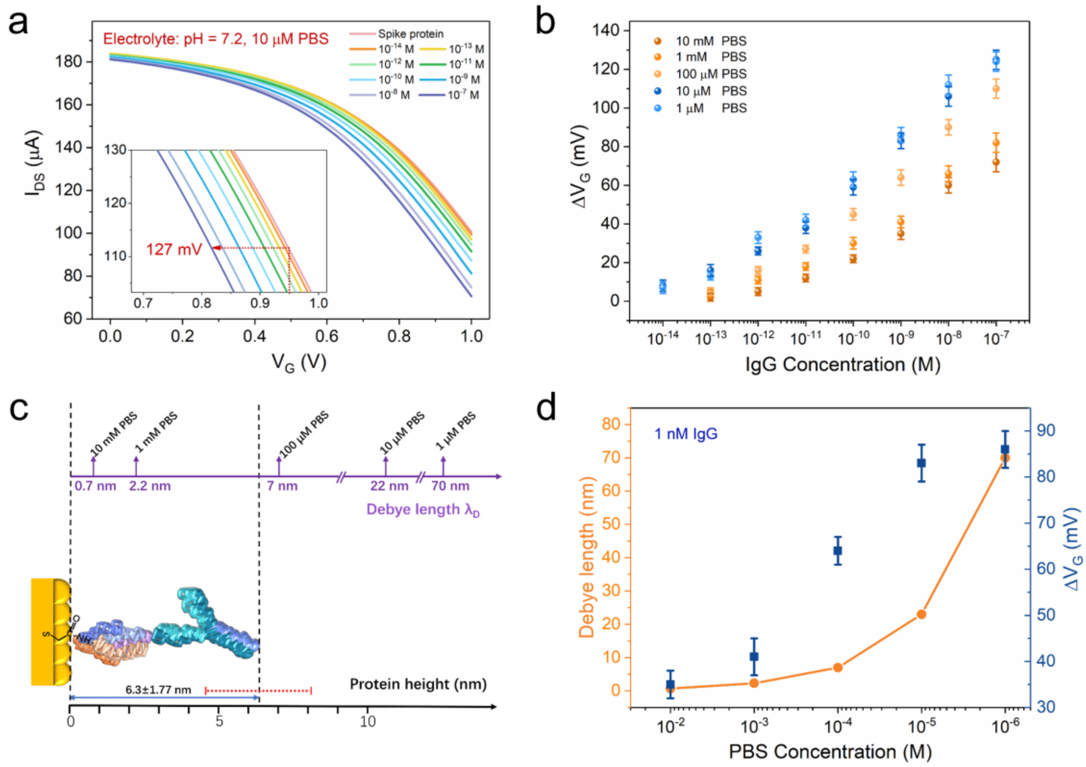

Figure 5.11 Detection of SARS-CoV-2 IgG in diluted PBS solutions. (a) The transfer characteristics of OECTs after incubation of SARS-CoV-2 IgG with different concentrations in sequence. (Electrolyte: 10 μM PBS, pH=7.2) (b) Relative change of the gate voltage ΔV_G as a function of IgG concentration. (Electrolyte: PBS with different concentration from 10 mM to 1 μM, pH = 7.2) (c) The comparation of Debye lengths of PBS solutions and protein height. (d) The variation of gate voltage ΔV_G and Debye length with the change of PBS concentration. The concentration of SARS-CoV-2 IgG solution detected by the device is set to be 1 nM.

To better understand the Debye length effect on the device performance, we calculated the Debye length at different PBS concentrations (Figure 5.11c). Here, the total height of antigen-antibody complex is 6.3 ±1.77 nm. When the ion concentration of PBS is higher than 1 mM, the Debye length is less than the distance between IgG and the gate and thus the positive charges on the protein will be screened by anions and cannot form a dipole with the gate. When the concentration of PBS solution is 10 μM or less, the Debye length is increased to over 22 nm, which is much bigger than the size of the proteins. Therefore, the whole positively charged protein can form a dipole with the gate at this condition and consequently the most pronounced effect can be obtained. Indeed, we can find the lowest detection limit (100 fM) of the IgG sensor when the PBS concentrations are 10 and 1 μM. The relationships between gate voltage shifts and IgG concentrations obtained in 10 μM and 1 μM PBS solutions are very similar (Figure 5.11b), indicating that further increase of the Debye length will not improve the device performance anymore. For the same concentration of IgG while different PBS concentrations used in device characterization (Figure 5.11d), we can find that the device responses are also dependent on the PBS concentration. With the decrease of PBS concentration, the shift of the transfer curve increases and saturates at the concentrations around 10 μM.

5.3.4 Sensitivity enhancement by increasing net charge of IgG

Another possible approach to improving the sensitivity of the IgG sensor is to increase the surface charge of IgG in solutions. It has been reported that the surface charge of proteins is influenced by the pH value of the solution.[200] Actually, the surface charge is related to the difference between the isoelectric point (pI) of the proteins and the pH value of the solution. When pI is identical to the pH value of the solution, no surface charge can be found on the proteins. Considering that SARS-CoV-2 IgG has an isoelectric point of 8.2, the protein is more positively charged when it is tested in solutions with lower pH values.

To enhance the surface charge of IgG, the devices were tested in acidic environment with different pH values (from 7.2 to 4.0). When pH value is 5.0, the device response (ΔV_G) to 100 nM SARS-CoV-2 IgG tested in 10 μM electrolyte is increased to 163 mV (Figure 5.12a). The device responses to IgG at different pH values are shown in Figure 5.12b. Notably, when the pH value of the electrolyte is 5.0, the detection limit is as low as 1 fM. However, the device responses to IgG are decreased when the pH value is further decreased to 4.0. This effect may be related to the weak dissociation of antigen antibody complex in acidic environment.[201] In this case, the binding of antigens and antibodies is weakened. Thus, it is reasonable to study the effect of pH between 7.2 and 5.0 on the device performance.

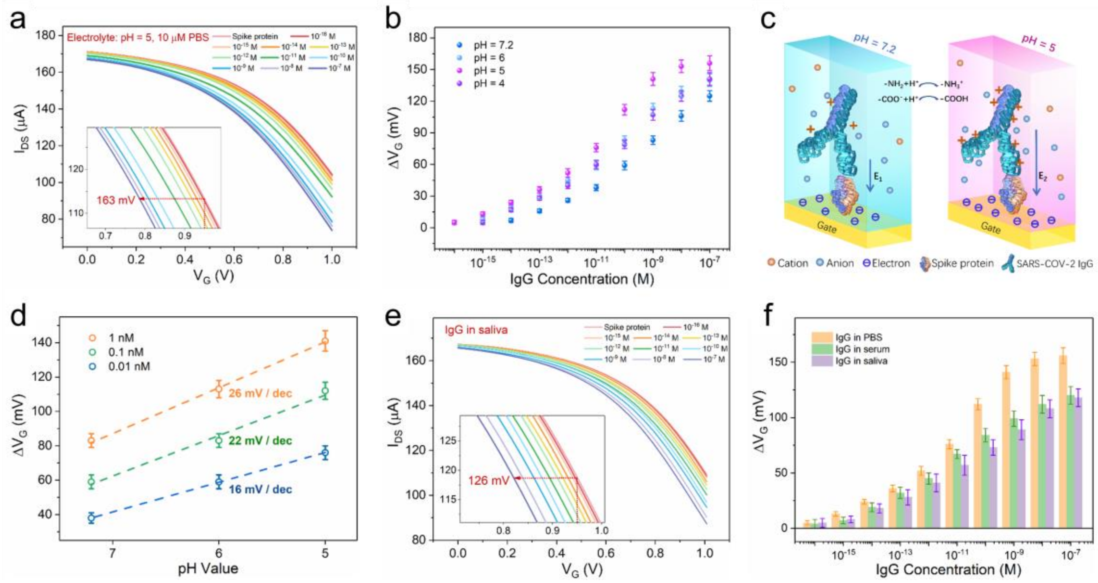

Figure 5.12 Detection of SARS-CoV-2 IgG by measuring OECTs in electrolytes with different pH values. (a)The transfer characteristics of OECTs after incubation of SARS-CoV-2 IgG with different concentrations in sequence. (Electrolyte: 10 μM PBS, pH = 5.0) (b) Relative change of the gate voltage ΔV_G as a function of IgG concentration measured in electrolytes with different pH values. (c) The scheme of net charge variation of a protein in electrolytes with different pH values (pH = 7.2 and 5.0). (d) Relative changes of the gate voltage ΔV_G for different IgG concentrations (1, 0.1 and 0.01 nM) as a function of pH values of the electrolytes on the OECT. (e) The transfer characteristics of OECTs after incubation of SARS-CoV-2 IgG (in saliva) with different concentrations in sequence. (f) The comparation of device responds at different IgG concentrations in detecting SARS-CoV-2 IgG in PBS, serum, and saliva. (Electrolyte: 10 μM PBS, pH = 5.0)

According to site-binding theory, the potential drop Δφ at the interface between protein and the electrolyte is given by:[202,203]

$$\Delta\varphi = 2.3\frac{KT}{q}\alpha\frac{\beta}{\beta+1}(pI - pH) \quad , \qquad (5)$$

where pI is the pH value at the point of zero charge of the protein (isoelectric point), pH is the pH value of the electrolyte. α represents the antibody coverage on the electrode surface, mainly related to the concentration of the protein. β can be expressed by the acidic equilibrium constants of the related amino acids reactions.[202] Thus, $\Delta\varphi$ is the maximum potential drop that can be obtained between the protein and the gate electrode.

As shown in the scheme (Figure 5.12 c), positively charged antibodies can form an electric dipole on the gate electrode surface. The more net charge the protein carries, the stronger the electric field is created (E_2>E_1, E_1 and E_2 are the electrostatic fields formed in gate electrolyte interface with pH=7.2 and 5, respectively). Thus, the potential change $\Delta\varphi$ increases with the decrease of pH value. The relationship between gate voltage shift and pH value was shown (Figure 5.12 d). The pH sensitivity is 16-26 mV/pH for different IgG concentrations, which are much smaller than the ideal value at room temperature (59 mV/pH).[203] This can be attributed to an incomplete protein coverage on the electrode surface. We can find that the pH sensitivity gradually decreases with the decrease of IgG concentration, which further confirms that less coverage of protein can decrease the pH sensitivity. In addition, we have tried to further optimize the concentration of spike protein solution on the gate modification and found that the device response saturates when the concentration is higher than 0.5 µM. Hence, the modification condition of the spike protein (1 µM) on the gate is not necessary to be changed (Figure 5.13).

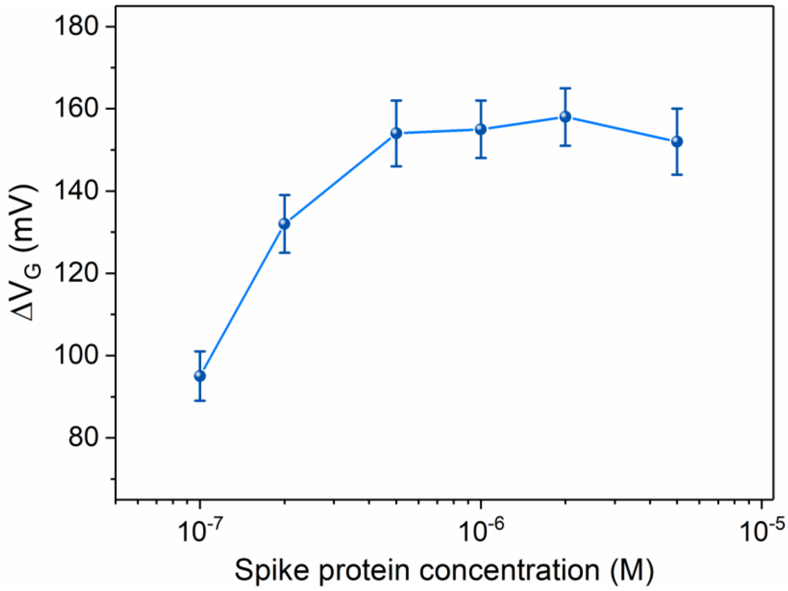

Figure 5.13 Results of effective gate voltage shifting with different spike protein concentration. Different concentration of spike protein (0.1 µM, 0.2 µM, 0.5 µM, 1 µM, 2 µM, 5 µM) were modified on the gate electrode for the detection of SARS-CoV-2 IgG. The tests were conducted in optimized electrolyte (10 µM PBS, pH =5). Results shows that spike protein concentration higher than 0.5 µM can get similar high signals.

5.3.5 SARS-CoV-2 IgG detection in serum and saliva samples

Since the actual detection environment is much more complicated than a PBS solution, we diluted the SARS-CoV-2 IgG in serum and saliva and incubated on gate electrodes for 10 minutes. After IgG (in diluted saliva) incubation, the transfer curves shift to negative voltage positions (Figure 5.12e), which is consistent with the result in PBS solution while the resultant variations are relatively lower. Figure 5.12f shows device responses in different detection environments. For 10 fM IgG concentration, the devices show average responds of 19 mV and 18 mV in serum and saliva samples, respectively, which can meet the requirement of signal to noise ratio higher than 3. Thus, the detection limits of the devices in measuring IgG in saliva and serum samples are 10 fM. SARS-CoV-2 IgG detections in saliva and serum both show good linear relationship in their concentration range (Figure 5.14). The detection range in serum is from 10 fM to 100 nM, perfectly matching the serum specific IgG levels in COVID-19 patients.[204] High sensitivity in saliva sample can also settle the problem of a low antibody level in saliva, which is normally 2-4 order of magnitude lower than that in serum [181,182].

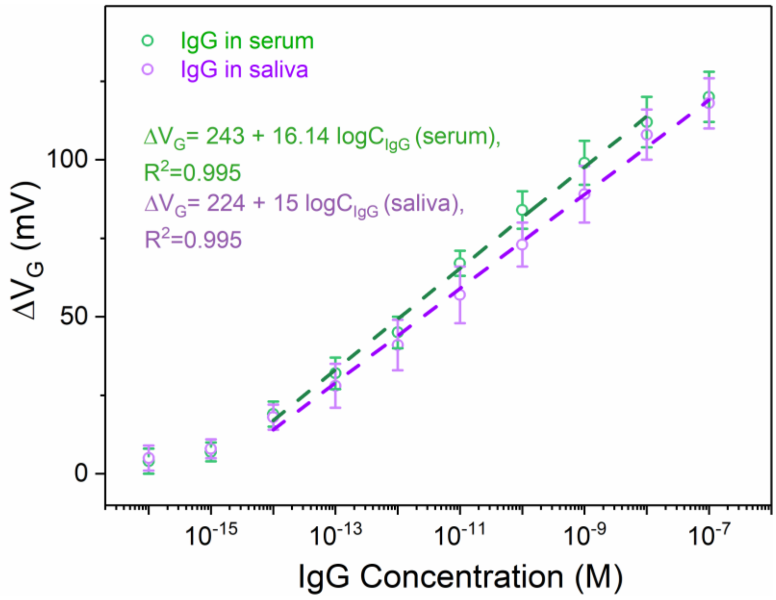

Figure 5.14 The linear relationship for IgG detection in serum and saliva. IgG detection in serum have good linear range between 10 fM and 10 nM with a coefficient of determination R^2 of 0.995, and IgG detection in saliva have good linear range between 10 fM and 100 nM with a R^2 of 0.995. (Test electrolyte: 10 μM PBS, pH = 5.0)

5.3.6 Enhanced testing speed by voltage pulses

As shown in Figure 5.15a, to further reduce the IgG incubation time, voltage pulses (frequency: 10^4 Hz, voltage: -0.5 V, pulse width: 10 μs, rise/fall time: 5 ns) were applied between the gate and another electrode during incubation. The positively charged IgG molecules can be driven by the electric field to the gate in the solution and an enhanced antigen and antibody binding efficiency is expected to be achieved.[205,206] The effect of voltage pulses on the binding efficiency of antigens and antibodies was tested under optimized conditions (electrolyte: 10 μM PBS, pH = 5; SARS-CoV-2 IgG 100 nM). The device responses (ΔV_G) versus incubation time (t) can be fitted with an exponential function $\Delta V_G = A\ [1-\exp(-t/\tau)]$ (Figure 5.15b). With voltage pulses during incubation, the time constant τ is 2.5 min, while the control device without voltage pulse shows the time constant of 4.6 min. Notably, the response of the device can reach 55% after 2 min incubation. For the detection of different concentrations of IgG, the effects of incubation time (with pulse) are shown in Figure 5.15c.

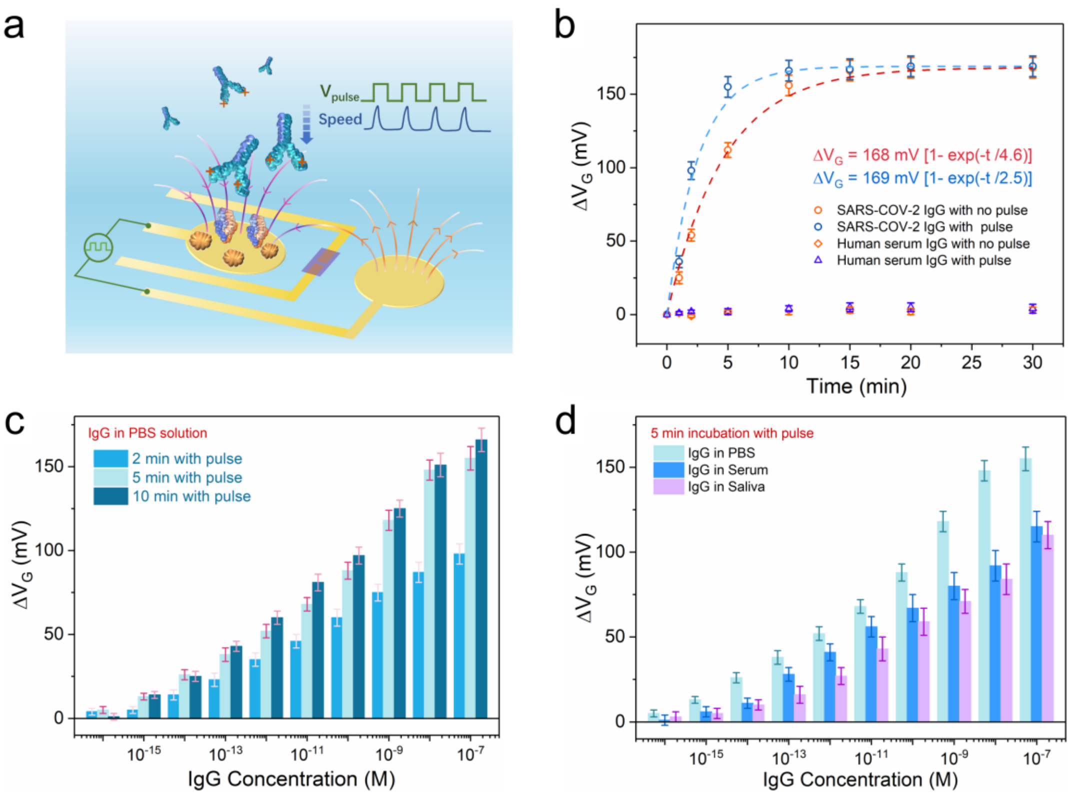

Figure 5.15 Detection of SARS-CoV-2 IgG after applying voltage pulses on gate electrode during IgG incubation. (a) The scheme of IgG migration under voltage pulses between two electrodes during incubation process. (b) Relative change of the gate voltage ΔV_G of OECTs as a function of incubation time. (Electrolyte: 10 μM PBS, pH = 5.0). The control tests were conducted by detecting human serum IgG with the same conditions. (c) Relative change of the gate voltage ΔV_G as a function of IgG concentration in PBS solution with different incubation time. (d) Device responses to IgG in PBS, serum, and saliva samples with 5 min incubation under voltage pulses.

The transfer characteristics measured at different conditions are presented in Figure 5.16. Hence, 2 min incubation under voltage pulse can lead to a detection limit of 1 fM in PBS. To ensure that the voltage pulse effect can be applied in practical applications, we added the voltage pulses in the serum and saliva samples. The device responses as a function of incubation time of serum and saliva samples under voltage pulses are shown in Figure 5.17. The time constant τ was decrease from 5.4 min to 3.2 min in serum sample, and from 5.3 min to 3.5 min in saliva samples, which further indicates that the voltage pulse can accelerate the IgG detection of our devices. In addition, the non-specific binding from pure serum and saliva is found to be negligible (Figure 5.17).

The relatively longer time constants for the tests in saliva and serum than that in PBS can be attributed to the complexity and high viscosity of the saliva and serum samples. The device responses at different IgG concentrations of the three type samples was tested with an incubation time of 5 min and a detection limit of 10 fM IgG can be achieved in saliva and serum samples (Figure 5.15d).

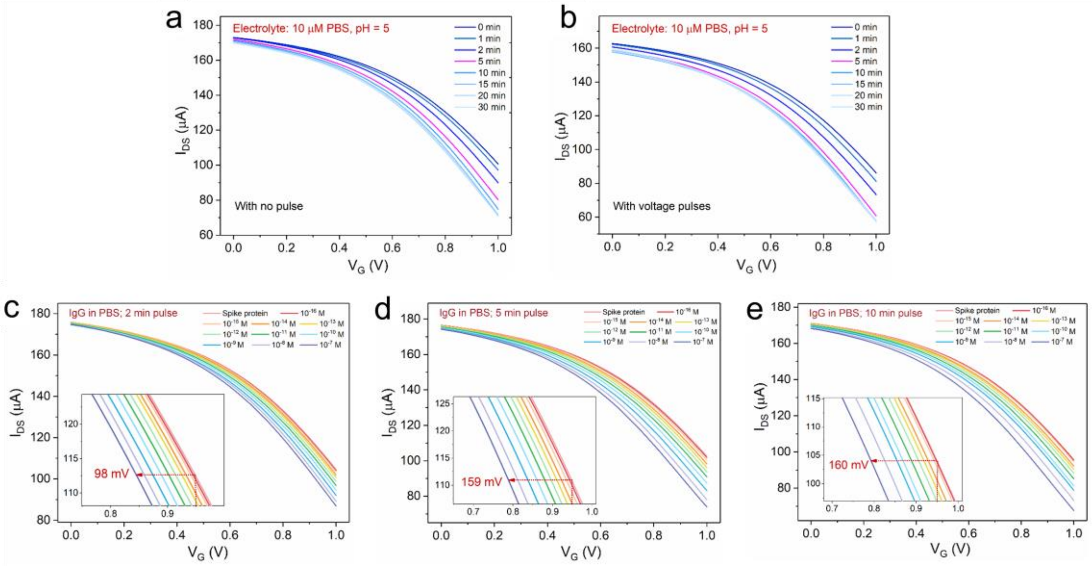

Figure 5.16 The transfer characteristics were measured after incubating IgG at different periods with and without voltage pulses under an electrolyte of 10 μM PBS with pH=5.0. (a) IgG (100 nM) was incubated without voltage pulses. (b) IgG (100 nM) was incubated with voltage pulses. Transfer characteristics were also measured after IgG incubation with different concentrations for (c) 2 minutes with pulses, (d) 5 minutes with pulses, and (e) 10 minutes with pulses.

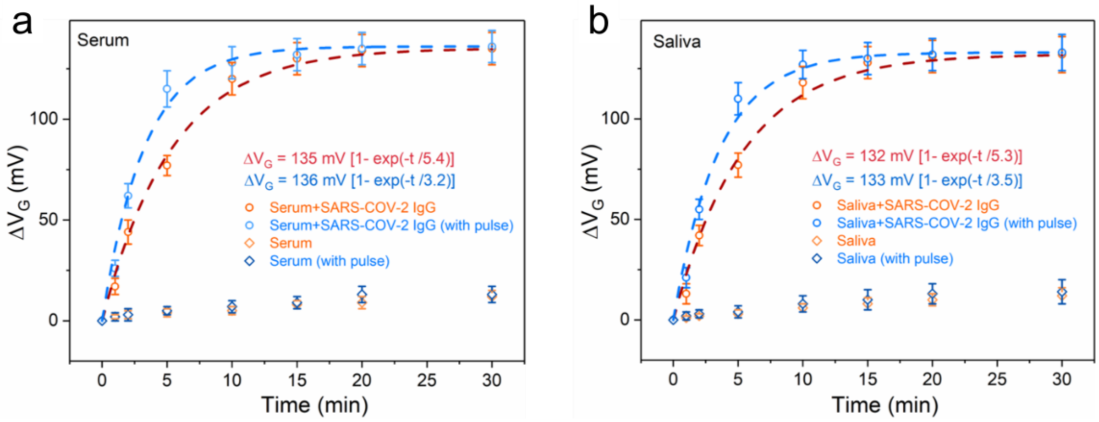

Figure 5.17 The relative change of the gate voltage (ΔVG) was measured as a function of the incubation time for (a) serum sample and (b) saliva sample under an electrolyte

of 10 µM PBS with pH=5.0. The background signal of the serum and saliva was detected, which was much lower than the specific SARS-CoV-2 IgG signal.

Table 5.1 Comparison of the SARS-CoV-2 IgG detection results of different techniques.

Target analyte	Methods	Detection limit	Time needed	Portable (Y/N)	Label free (Y/N)	References
IgG	OECT	1 fM (150 fg/mL)	2 min in PBS; 5 min in saliva and serum	Y	Y	Our work
IgG IgM CRP N protein	Electrochemical platform, ELISA	250 ng/mL (IgG) 250 ng/mL (IgM) 50 ng/mL (CRP) 500 pg/mL (N protein)	Within 10 min	Y	N	207
IgG	LSPR	0.5 pM (0.08 ng/mL)	Within 30 min	N	Y	208
IgG S protein N protein	ELISA	2 ng/mL (IgG) 4 pg/mL (S protein) 62 pg/mL (N protein)	15 min (IgG); 40 min (Antigens)	Y	N	209
IgG IgM	LFIA	5 ng/mL (IgG) 20 ng/mL (IgM)	10 min	Y	N	210
IgG IgM	Fluorescence immunoassay	-	15 min	Y	N	211
IgG IgM	LFIA	-	15 min	Y	N	212

OECT: organic electrochemical transistor
CRP: C-reactive protein
ELISA: enzyme-linked immunosorbent assay
LSPR: localized surface plasmon resonance
LFIA: lateral flow immunoassay

5.4 Summary

In conclusion, we have developed portable, label-free and low-cost biosensors based on OECTs for rapid and highly sensitive detections of SARS-CoV-2 IgG. The gate electrodes of the OECTs are modified with SARS-CoV-2 spike protein that can selectively capture the IgG through the specific antibody-antigen reaction. The positively charged IgG molecules in aqueous solutions form electrical dipoles on gate surfaces and modulate the channel currents of the OECTs. By optimizing the measurement conditions, including electrolyte ion concentration and pH value, high device sensitivity has been achieved. The detection limits of the devices can reach 1 fM in aqueous solutions and 10 fM in saliva and serum samples, which are much better than many existing electrochemical methods (See Table 5.1).[207-212] Notably, the detectable region can cover the concentrations of the specific antibody in the serum and saliva of COVID-19 patients, promising a high potential for practical applications. More importantly, faster detection of IgG has been realized by applying voltage pulses on the gates of OECTs during incubation and stable signal can be obtained within 5 min. The testing process has been remotely operated with a mobile phone by controlling a portable meter via Bluetooth, which can meet the requirement of fast and point-of-care detection of COVID-19 antibody. It is expected that the biosensor can also be used in the fast detections of many other diseases that may generate antibodies.

Chapter 6 Conclusions and Perspectives

6.1 Conclusions

This thesis is focused on the developing of high-performance short-channel OECTs, and their application in biosensing and integrated circuits. In the literature review section, the OECT device physics, performance parameters, and channel materials are summarized. The biosensing strategies and electrophysiology recording methods are comprehensively introduced. Currently, the electrolyte-gated organic thin film transistors are almost all planar structures, in which the channel length is limited by the photolithography technique (over 50 nm). In vertical OECT, the source and drain electrodes can be spaced by a dielectric layer, and the channel length is determined by oxide spacer thickness. The low source drain tunneling current lead to high-performance OECTs even with 1 nm channel length, which overcome the short-channel effect. Short-channel OECTs are further applied in electrophysiology recoding and complementary inverter. For the current COVID-19 pandemic, the OECTs are applied for the highly sensitive and portable COVID-19 antibody detection. The specific contents are as follows.

Firstly, short-channel vertical OECTs are fabricated with Al_2O_3 as channel spacer. Small electrodes overlap area and low voltage bias lead to low source drain tunneling currents. The minimal channel length of OECT can reach 0.86 nm, which shows an on-off ratio of 476 in the channel current. Devices performances of three kinds of channel materials PEDOT:PSS, p(g2T-TT), and p($g_7NC_{10}N$) are tested. When channel length is larger than 1.8 nm, both p-type and n-type OECT devices can realize more than 10^6 on-off ratio in channel currents, and an ideal subthreshold slope of 60 mV/dec. The conductive performance is limited by the parasitic resistance, which can be improved by increasing the thickness of source drain electrodes. High transconductances of 19.8

mS and 19.1 mS were achieved for p(g2T-TT) devices and PEDOT:PSS devices, respectively, despite having a channel width of only 5 μm. Short-channel OECTs can work steadily with over 10000 gate voltage pulses. This vertical structure may also be applicable for other solution-gated transistors.

Four factors that could potentially impact the transient response time of short-channel OECTs were examined: channel area, channel thickness, channel length, and gate-channel distance. Results indicate that decreasing channel area and thickness can lead to improved transient response. Finally, the response time of p-type PEDOT:PSS-based OECT is 0.97 μs, and the response time of n-type p(g_7NC_{10}N)-based OECT is 0.32 ms. The response time of p-type PEDOT:PSS-based OECT is 0.97 μs, while the response time of n-type p(g7NC10N)-based OECT is 0.32 ms. These figures represent the fastest response times recorded among both p-type and n-type OECTs. The fast response and high transconductance OECTs are successfully applied in ECG and EOG recording. Complementary inverter based on p-type OECTs and n-type OECTs are fabricated. The two OECTs displayed low subthreshold slope and a comparable on-current level. The resulting inverter shows a record high gain of 456 V/V. Additionally, the inverter proved effective for amplifying AC signals, boasting a voltage gain of 21 V/V. Such high-performance vertical short-channel OECTs hold significant potential for widespread application in biosensing and integrated circuits.

Thirdly, the ultrafast, sensitive and portable detection of COVID-19 IgG is realized using flexible OECTs. The spike protein is modified on the gate surface to selectively bind with antibodies. Positively charged IgG can form an electrical dipole on the gate interface and change the effective gate voltage. A portable meter is designed to apply voltages and detect electrical signals. The sensitivity is promoted by increasing Debye length and protein net charges. A voltage pulse is added during the antibody incubation process to reduce the incubation time. Finally, the OECT based biosensor can detect 1fM COVID-19 IgG in PBS samples, and 10 fM COVID-19 IgG in serum and saliva samples. Only 5 min incubation time is needed under the pulse acceleration. This platform shows good selectivity by differentiating from other human serum antibodies. This platform is also applicable for the detection of other protein biomarkers, and for testing and screening of large-scale infectious diseases.

6.2 Perspectives

Currently, the theoretical mechanism underlying short-channel vertical OECTs is yet to be studied. Although studies have shown that short-channel OECTs exhibit low source-drain tunnelling and gate leakage currents, the theoretical models for these aspects need to be established. The development of such models can serve as a reference for future studies, such as exploring the replacement of aluminum oxide with other oxides having higher dielectric constants, using metal electrodes with different work functions, and determining if shorter channels can be achieved with smaller overlap areas. Additionally, it is worth investigating the proportion of gate leakage in the channel current to assess if better device performance can be achieved with lower gate leakage current.

In this thesis, the transient response time of the n-type OECT lags behind, possibly due to the higher material capacitance and film thickness. Further testing is required to confirm the relationship between the type of material and response speed. Additionally, the transient response of the OECT-based complementary inverter is limited by the n-type OECT, which could be replaced by other high mobility and low capacitance n-type materials. Furthermore, the complementary inverter could be utilized for ECG and EOG testing to achieve a higher signal-to-noise ratio.

To facilitate the practical application and commercialization of OECT-based COVID-19 antibody detection, clinical trials are necessary. Additionally, there is a need to consider the fabrication of low-cost, large-area OECT devices. To achieve this, the expensive photolithography and deposition techniques can be replaced by printing technology, which enables the production of a large number of transistors on flexible substrates. Furthermore, OECT can be utilized in the detection of other biomarkers, such as influenza A virus and cancer biomarkers.

References:

(1) Geffroy, B.; Le Roy, P.; Prat, C. Organic light-emitting diode (OLED) technology: materials, devices and display technologies. *Polym. Int.* **2006,** *55* (6), 572.

(2) Klauk, H. Organic thin-film transistors. *Chem. Soc. Rev.* **2010,** *39* (7), 2643.

(3) Günes, S.; Neugebauer, H.; Sariciftci, N. S. Conjugated polymer-based organic solar cells. *Chem. Rev.* **2007,** *107* (4), 1324.

(4) Simon-Yarza, T.; Mielcarek, A.; Couvreur, P.; Serre, C. Nanoparticles of metal-organic frameworks: on the road to in vivo efficacy in biomedicine. *Adv. Mater.* **2018,** *30* (37), 1707365.

(5) Fahlman, M.; Fabiano, S.; Gueskine, V.; Simon, D.; Berggren, M.; Crispin, X. Interfaces in organic electronics. *Nat. Rev. Mater.* **2019,** *4* (10), 627.

(6) Forrest, S. R.; Thompson, M. E. Introduction: Organic electronics and optoelectronics. *Chem. Rev.* **2007,** *107* (4), 923.

(7) Zhang, M. L.; Tang, Z. J.; Liu, X. L.; van der Spiegel, J. Electronic neural interfaces. *Nat Electron* **2020,** *3* (4), 191.

(8) Fattahi, P.; Yang, G.; Kim, G.; Abidian, M. R. A review of organic and inorganic biomaterials for neural interfaces. *Adv. Mater.* **2014,** *26* (12), 1846.

(9) Lanzani, G. Materials for bioelectronics: organic electronics meets biology. *Nat. Mater.* **2014,** *13* (8), 775.

(10) Nezakati, T.; Seifalian, A.; Tan, A.; Seifalian, A. M. Conductive Polymers: Opportunities and Challenges in Biomedical Applications. *Chem. Rev.* **2018,** *118* (14), 6766.

(11) Ul Ahad, I.; Bartnik, A.; Fiedorowicz, H.; Kostecki, J.; Korczyc, B.; Ciach, T.; Brabazon, D. Surface modification of polymers for biocompatibility via exposure to extreme ultraviolet radiation. *J. Biomed. Mater. Res., Part A* **2014,** *102* (9), 3298.

(12) Chortos, A.; Liu, J.; Bao, Z. Pursuing prosthetic electronic skin. *Nat Mater* **2016,**

15 (9), 937.

(13) Wagner, S.; Bauer, S. Materials for stretchable electronics. *MRS Bull.* **2012,** *37* (3), 207.

(14) Hong, S. Y.; Lee, Y. H.; Park, H.; Jin, S. W.; Jeong, Y. R.; Yun, J.; You, I.; Zi, G.; Ha, J. S. Stretchable Active Matrix Temperature Sensor Array of Polyaniline Nanofibers for Electronic Skin. *Adv. Mater.* **2016,** *28* (5), 930.

(15) Zhou, Y.; He, J.; Wang, H.; Qi, K.; Nan, N.; You, X.; Shao, W.; Wang, L.; Ding, B.; Cui, S. Highly sensitive, self-powered and wearable electronic skin based on pressure-sensitive nanofiber woven fabric sensor. *Sci Rep* **2017,** *7* (1), 12949.

(16) Lee, W. W.; Tan, Y. J.; Yao, H.; Li, S.; See, H. H.; Hon, M.; Ng, K. A.; Xiong, B.; Ho, J. S.; Tee, B. C. K. A neuro-inspired artificial peripheral nervous system for scalable electronic skins. *Sci Robot* **2019,** *4* (32), eaax2198.

(17) Simon, D. T.; Gabrielsson, E. O.; Tybrandt, K.; Berggren, M. Organic Bioelectronics: Bridging the Signaling Gap between Biology and Technology. *Chem. Rev.* **2016,** *116* (21), 13009.

(18) Wang, S.; Xu, J.; Wang, W.; Wang, G. N.; Rastak, R.; Molina-Lopez, F.; Chung, J. W.; Niu, S.; Feig, V. R.; Lopez, J.et al. Skin electronics from scalable fabrication of an intrinsically stretchable transistor array. *Nature* **2018,** *555* (7694), 83.

(19) Ohayon, D.; Nikiforidis, G.; Savva, A.; Giugni, A.; Wustoni, S.; Palanisamy, T.; Chen, X.; Maria, I. P.; Di Fabrizio, E.; Costa, P.et al. Biofuel powered glucose detection in bodily fluids with an n-type conjugated polymer. *Nat Mater* **2020,** *19* (4), 456.

(20) Lee, W.; Kobayashi, S.; Nagase, M.; Jimbo, Y.; Saito, I.; Inoue, Y.; Yambe, T.; Sekino, M.; Malliaras, G. G.; Yokota, T.et al. Nonthrombogenic, stretchable, active multielectrode array for electroanatomical mapping. *Sci Adv* **2018,** *4* (10), eaau2426.

(21) Venkatraman, V.; Friedlein, J. T.; Giovannitti, A.; Maria, I. P.; McCulloch, I.; McLeod, R. R.; Rivnay, J. Subthreshold Operation of Organic Electrochemical

Transistors for Biosignal Amplification. *Adv. Sci.* **2018,** *5* (8), 1800453.

(22) Guo, K.; Wustoni, S.; Koklu, A.; Diaz-Galicia, E.; Moser, M.; Hama, A.; Alqahtani, A. A.; Ahmad, A. N.; Alhamlan, F. S.; Shuaib, M.et al. Rapid single-molecule detection of COVID-19 and MERS antigens via nanobody-functionalized organic electrochemical transistors. *Nat Biomed Eng* **2021,** *5* (7), 666.

(23) Cinquin, P.; Gondran, C.; Giroud, F.; Mazabrard, S.; Pellissier, A.; Boucher, F.; Alcaraz, J. P.; Gorgy, K.; Lenouvel, F.; Mathe, S.et al. A glucose biofuel cell implanted in rats. *PLoS One* **2010,** *5* (5), e10476.

(24) Yu, Y.; Nassar, J.; Xu, C.; Min, J.; Yang, Y.; Dai, A.; Doshi, R.; Huang, A.; Song, Y.; Gehlhar, R.et al. Biofuel-powered soft electronic skin with multiplexed and wireless sensing for human-machine interfaces. *Sci Robot* **2020,** *5* (41), eaaz7946.

(25) Kergoat, L.; Piro, B.; Berggren, M.; Horowitz, G.; Pham, M. C. Advances in organic transistor-based biosensors: from organic electrochemical transistors to electrolyte-gated organic field-effect transistors. *Anal. Bioanal. Chem.* **2012,** *402* (5), 1813.

(26) Tang, H.; Yan, F.; Lin, P.; Xu, J. B.; Chan, H. L. W. Highly Sensitive Glucose Biosensors Based on Organic Electrochemical Transistors Using Platinum Gate Electrodes Modified with Enzyme and Nanomaterials. *Adv. Funct. Mater.* **2011,** *21* (12), 2264.

(27) Macchia, E.; Manoli, K.; Holzer, B.; Di Franco, C.; Ghittorelli, M.; Torricelli, F.; Alberga, D.; Mangiatordi, G. F.; Palazzo, G.; Scamarcio, G.et al. Single-molecule detection with a millimetre-sized transistor. *Nat. Commun.* **2018,** *9* (1), 3223.

(28) Marks, A.; Griggs, S.; Gasparini, N.; Moser, M. Organic Electrochemical Transistors: An Emerging Technology for Biosensing. *Adv Mater Interfaces* **2022,** *9* (6), 2102039.

(29) Meyer, A. F.; Poort, J.; O'Keefe, J.; Sahani, M.; Linden, J. F. A Head-Mounted

Camera System Integrates Detailed Behavioral Monitoring with Multichannel Electrophysiology in Freely Moving Mice. *Neuron* **2018,** *100* (1), 46.

(30) Ehrlich, J. R.; Cha, T. J.; Zhang, L.; Chartier, D.; Melnyk, P.; Hohnloser, S. H.; Nattel, S. Cellular electrophysiology of canine pulmonary vein cardiomyocytes: action potential and ionic current properties. *J Physiol* **2003,** *551* (Pt 3), 801.

(31) Reilly, R. B.; Lee, T. C. Electrograms (ECG, EEG, EMG, EOG). *Technol. Health Care* **2010,** *18* (6), 443.

(32) McCulloch, I. Thin films: rolling out organic electronics. *Nat Mater* **2005,** *4* (8), 583.

(33) Zeglio, E.; Inganas, O. Active Materials for Organic Electrochemical Transistors. *Adv. Mater.* **2018,** *30* (44), e1800941.

(34) Khodagholy, D.; Doublet, T.; Quilichini, P.; Gurfinkel, M.; Leleux, P.; Ghestem, A.; Ismailova, E.; Herve, T.; Sanaur, S.; Bernard, C.et al. In vivo recordings of brain activity using organic transistors. *Nat Commun* **2013,** *4* (1), 1575.

(35) Bontapalle, S.; Na, M.; Park, H.; Sim, K. Fully soft organic electrochemical transistor enabling direct skin-mountable electrophysiological signal amplification. *Chem Commun (Camb)* **2022,** *58* (9), 1298.

(36) White, H. S.; Kittlesen, G. P.; Wrighton, M. S. Chemical derivatization of an array of three gold microelectrodes with polypyrrole: fabrication of a molecule-based transistor. *J. Am. Chem. Soc.* **1984,** *106* (18), 5375.

(37) Bernards, D. A.; Malliaras, G. G. Steady-state and transient behavior of organic electrochemical transistors. *Adv. Funct. Mater.* **2007,** *17* (17), 3538.

(38) Braga, D.; Horowitz, G. High-Performance Organic Field-Effect Transistors. *Adv. Mater.* **2009,** *21* (14-15), 1473.

(39) Panzer, M. J.; Frisbie, C. D. Exploiting ionic coupling in electronic devices: Electrolyte-gated organic field-effect transistors. *Adv. Mater.* **2008,** *20* (16), 3177.

(40) Schmode, P.; Ohayon, D.; Reichstein, P. M.; Savva, A.; Inal, S.; Thelakkat, M. High-Performance Organic Electrochemical Transistors Based on Conjugated

Polyelectrolyte Copolymers. *Chem. Mater.* **2019,** *31* (14), 5286.

(41) Khodagholy, D.; Rivnay, J.; Sessolo, M.; Gurfinkel, M.; Leleux, P.; Jimison, L. H.; Stavrinidou, E.; Herve, T.; Sanaur, S.; Owens, R. M.et al. High transconductance organic electrochemical transistors. *Nat Commun* **2013,** *4* (1), 2133.

(42) Rivnay, J.; Leleux, P.; Sessolo, M.; Khodagholy, D.; Herve, T.; Fiocchi, M.; Malliaras, G. G. Organic electrochemical transistors with maximum transconductance at zero gate bias. *Adv. Mater.* **2013,** *25* (48), 7010.

(43) Tarabella, G.; Santato, C.; Yang, S. Y.; Iannotta, S.; Malliaras, G. G.; Cicoira, F. Effect of the gate electrode on the response of organic electrochemical transistors. *Appl. Phys. Lett.* **2010,** *97* (12), 205.

(44) Rivnay, J.; Leleux, P.; Ferro, M.; Sessolo, M.; Williamson, A.; Koutsouras, D. A.; Khodagholy, D.; Ramuz, M.; Strakosas, X.; Owens, R. M.et al. High-performance transistors for bioelectronics through tuning of channel thickness. *Sci Adv* **2015,** *1* (4), e1400251.

(45) Cendra, C.; Giovannitti, A.; Savva, A.; Venkatraman, V.; McCulloch, I.; Salleo, A.; Inal, S.; Rivnay, J. Role of the Anion on the Transport and Structure of Organic Mixed Conductors. *Adv. Funct. Mater.* **2019,** *29* (5), 1807034.

(46) Yan, Y.; Chen, Q.; Wu, X.; Wang, X.; Li, E.; Ke, Y.; Liu, Y.; Chen, H.; Guo, T. High-Performance Organic Electrochemical Transistors with Nanoscale Channel Length and Their Application to Artificial Synapse. *Acs Appl. Mater. Inter.* **2020,** *12* (44), 49915.

(47) Cea, C.; Spyropoulos, G. D.; Jastrzebska-Perfect, P.; Ferrero, J. J.; Gelinas, J. N.; Khodagholy, D. Enhancement-mode ion-based transistor as a comprehensive interface and real-time processing unit for in vivo electrophysiology. *Nat Mater* **2020,** *19* (6), 679.

(48) Yamamoto, S.; Polyravas, A. G.; Han, S.; Malliaras, G. G. Correlation between Transient Response and Neuromorphic Behavior in Organic Electrochemical Transistors. *Adv. Electron. Mater.* **2022,** *8* (4), 2101186.

(49) Tyrrell, J. E.; Boutelle, M. G.; Campbell, A. Measurement of Electrophysiological Signals In Vitro Using High-Performance Organic Electrochemical Transistors. *Adv. Funct. Mater.* **2021,** *31* (1), 2007086.

(50) Friedlein, J. T.; McLeod, R. R.; Rivnay, J. Device physics of organic electrochemical transistors. *Org. Electron.* **2018,** *63*, 398.

(51) Wu, X.; Surendran, A.; Moser, M.; Chen, S.; Muhammad, B. T.; Maria, I. P.; McCulloch, I.; Leong, W. L. Universal Spray-Deposition Process for Scalable, High-Performance, and Stable Organic Electrochemical Transistors. *Acs Appl. Mater. Inter.* **2020,** *12* (18), 20757.

(52) Savva, A.; Cendra, C.; Giugni, A.; Torre, B.; Surgailis, J.; Ohayon, D.; Giovannitti, A.; McCulloch, I.; Di Fabrizio, E.; Salleo, A.et al. Influence of Water on the Performance of Organic Electrochemical Transistors. *Chem. Mater.* **2019,** *31* (3), 927.

(53) Wu, X. H.; Stephen, M.; Hidalgo, T. C.; Salim, T.; Surgailis, J.; Surendran, A.; Su, X. Q.; Li, T.; Inal, S.; Leong, W. L. Ionic-Liquid Induced Morphology Tuning of PEDOT:PSS for High-Performance Organic Electrochemical Transistors. *Adv. Funct. Mater.* **2022,** *32* (1), 2108510.

(54) Friedlein, J. T.; Donahue, M. J.; Shaheen, S. E.; Malliaras, G. G.; McLeod, R. R. Microsecond Response in Organic Electrochemical Transistors: Exceeding the Ionic Speed Limit. *Adv. Mater.* **2016,** *28* (38), 8398.

(55) Spyropoulos, G. D.; Gelinas, J. N.; Khodagholy, D. Internal ion-gated organic electrochemical transistor: A building block for integrated bioelectronics. *Sci Adv* **2019,** *5* (2), eaau7378.

(56) Wu, H. Y.; Yang, C. Y.; Li, Q.; Kolhe, N. B.; Strakosas, X.; Stoeckel, M. A.; Wu, Z.; Jin, W.; Savvakis, M.; Kroon, R. Influence of Molecular Weight on the Organic Electrochemical Transistor Performance of Ladder-Type Conjugated Polymers. *Adv. Mater.* **2022,** *34* (4), 2106235.

(57) Weissbach, A.; Bongartz, L. M.; Cucchi, M.; Tseng, H.; Leo, K.; Kleemann, H. Photopatternable solid electrolyte for integrable organic electrochemical

transistors: operation and hysteresis. *J. Mater. Chem. C* **2022,** *10* (7), 2656.

(58) Inal, S.; Rivnay, J.; Hofmann, A. I.; Uguz, I.; Mumtaz, M.; Katsigiannopoulos, D.; Brochon, C.; Cloutet, E.; Hadziioannou, G.; Malliaras, G. G. Organic Electrochemical Transistors Based on PEDOT with Different Anionic Polyelectrolyte Dopants. *J Polym Sci Pol Phys* **2016,** *54* (2), 147.

(59) Jimison, L. H.; Hama, A.; Strakosas, X.; Armel, V.; Khodagholy, D.; Ismailova, E.; Malliaras, G. G.; Winther-Jensen, B.; Owens, R. M. PEDOT:TOS with PEG: a biofunctional surface with improved electronic characteristics. *J. Mater. Chem.* **2012,** *22* (37), 19498.

(60) Karlsson, R. H.; Herland, A.; Hamedi, M.; Wigenius, J. A.; Aslund, A.; Liu, X. J.; Fahlman, M.; Inganas, O.; Konradsson, P. Iron-Catalyzed Polymerization of Alkoxysulfonate-Functionalized 3,4-Ethylenedioxythiophene Gives Water-Soluble Poly(3,4-ethylenedioxythiophene) of High Conductivity. *Chem. Mater.* **2009,** *21* (9), 1815.

(61) Inal, S.; Rivnay, J.; Leleux, P.; Ferro, M.; Ramuz, M.; Brendel, J. C.; Schmidt, M. M.; Thelakkat, M.; Malliaras, G. G. A high transconductance accumulation mode electrochemical transistor. *Adv. Mater.* **2014,** *26* (44), 7450.

(62) Wang, L.; Sun, Q. Z.; Zhang, L. R.; Wang, J.; Ren, G. Z.; Yu, L. Y. Z.; Wang, K. L.; Zhu, Y. M.; Lu, G.; Yu, H. D. Realizing Ultrahigh Transconductance in Organic Electrochemical Transistor by Co-Doping PEDOT:PSS with Ionic Liquid and Dodecylbenzenesulfonate. *Macromol. Rapid Commun.* **2022,** *43* (17), 2200212.

(63) Kim, S. M.; Kim, C. H.; Kim, Y.; Kim, N.; Lee, W. J.; Lee, E. H.; Kim, D.; Park, S.; Lee, K.; Rivnay, J.et al. Influence of PEDOT:PSS crystallinity and composition on electrochemical transistor performance and long-term stability. *Nat Commun* **2018,** *9* (1), 3858.

(64) Hallani, R. K.; Paulsen, B. D.; Petty, A. J., 2nd; Sheelamanthula, R.; Moser, M.; Thorley, K. J.; Sohn, W.; Rashid, R. B.; Savva, A.; Moro, S.et al. Regiochemistry-Driven Organic Electrochemical Transistor Performance

Enhancement in Ethylene Glycol-Functionalized Polythiophenes. *J. Am. Chem. Soc.* **2021,** *143* (29), 11007.

(65) Moser, M.; Hidalgo, T. C.; Surgailis, J.; Gladisch, J.; Ghosh, S.; Sheelamanthula, R.; Thiburce, Q.; Giovannitti, A.; Salleo, A.; Gasparini, N.et al. Side Chain Redistribution as a Strategy to Boost Organic Electrochemical Transistor Performance and Stability. *Adv. Mater.* **2020,** *32* (37), 2002748.

(66) Lan, L. Y.; Chen, J. X.; Wang, Y. Z.; Li, P. Y.; Yu, Y. P.; Zhu, G. M.; Li, Z. K.; Lei, T.; Yue, W.; McCulloch, I. Facilely Accessible Porous Conjugated Polymers toward High-Performance and Flexible Organic Electrochemical Transistors. *Chem. Mater.* **2022,** *34* (4), 1666.

(67) Wu, X.; Liu, Q.; Surendran, A.; Bottle, S. E.; Sonar, P.; Leong, W. L. Enhancing the electrochemical doping efficiency in diketopyrrolopyrrole-based polymer for organic electrochemical transistors. *Adv. Electron. Mater.* **2021,** *7* (1), 2000701.

(68) Griggs, S.; Marks, A.; Bristow, H.; McCulloch, I. n-Type organic semiconducting polymers: stability limitations, design considerations and applications. *J Mater Chem C Mater* **2021,** *9* (26), 8099.

(69) Giovannitti, A.; Nielsen, C. B.; Sbircea, D.-T.; Inal, S.; Donahue, M.; Niazi, M. R.; Hanifi, D. A.; Amassian, A.; Malliaras, G. G.; Rivnay, J. N-type organic electrochemical transistors with stability in water. *Nat. Commun.* **2016,** *7* (1), 1.

(70) Giovannitti, A.; Maria, I. P.; Hanifi, D.; Donahue, M. J.; Bryant, D.; Barth, K. J.; Makdah, B. E.; Savva, A.; Moia, D.; Zetek, M.et al. The Role of the Side Chain on the Performance of N-type Conjugated Polymers in Aqueous Electrolytes. *Chem. Mater.* **2018,** *30* (9), 2945.

(71) Savva, A.; Ohayon, D.; Surgailis, J.; Paterson, A. F.; Hidalgo, T. C.; Chen, X. X.; Maria, I. P.; Paulsen, B. D.; Petty, A. J.; Rivnay, J.et al. Solvent Engineering for High-Performance n-Type Organic Electrochemical Transistors. *Adv. Electron. Mater.* **2019,** *5* (8), 1900249.

(72) Paterson, A. F.; Savva, A.; Wustoni, S.; Tsetseris, L.; Paulsen, B. D.; Faber, H.;

Emwas, A. H.; Chen, X.; Nikiforidis, G.; Hidalgo, T. C.et al. Water stable molecular n-doping produces organic electrochemical transistors with high transconductance and record stability. *Nat Commun* **2020,** *11* (1), 3004.

(73) Ohayon, D.; Savva, A.; Du, W.; Paulsen, B. D.; Uguz, I.; Ashraf, R. S.; Rivnay, J.; McCulloch, I.; Inal, S. Influence of Side Chains on the n-Type Organic Electrochemical Transistor Performance. *Acs Appl. Mater. Inter.* **2021,** *13* (3), 4253.

(74) Samuel, J. J.; Garudapalli, A.; Mohapatra, A. A.; Gangadharappa, C.; Patil, S.; Aetukuri, N. P. B. Single-Component CMOS-Like Logic using Diketopyrrolopyrrole-Based Ambipolar Organic Electrochemical Transistors. *Adv. Funct. Mater.* **2021,** *31* (45), 2102903.

(75) Li, P.; Shi, J.; Lei, Y.; Huang, Z.; Lei, T. Switching p-type to high-performance n-type organic electrochemical transistors via doped state engineering. *Nat Commun* **2022,** *13* (1), 5970.

(76) Bischak, C. G.; Flagg, L. Q.; Yan, K.; Li, C. Z.; Ginger, D. S. Fullerene Active Layers for n-Type Organic Electrochemical Transistors. *Acs Appl. Mater. Inter.* **2019,** *11* (31), 28138.

(77) Stein, E.; Nahor, O.; Stolov, M.; Freger, V.; Petruta, I. M.; McCulloch, I.; Frey, G. L. Ambipolar blend-based organic electrochemical transistors and inverters. *Nat Commun* **2022,** *13* (1), 5548.

(78) Feng, K.; Shan, W.; Ma, S.; Wu, Z.; Chen, J.; Guo, H.; Liu, B.; Wang, J.; Li, B.; Woo, H. Y.et al. Fused Bithiophene Imide Dimer-Based n-Type Polymers for High-Performance Organic Electrochemical Transistors. *Angew. Chem. Int. Ed. Engl.* **2021,** *60* (45), 24198.

(79) Feng, K.; Shan, W. T.; Wang, J. W.; Lee, J. W.; Yang, W. L.; Wu, W. C.; Wang, Y. M.; Kim, B. J.; Guo, X. G.; Guo, H. Cyano-Functionalized n-Type Polymer with High Electron Mobility for High-Performance Organic Electrochemical Transistors. *Adv. Mater.* **2022,** *34* (24), 2201340.

(80) Sun, H. D.; Vagin, M.; Wang, S. H.; Crispin, X.; Forchheimer, R.; Berggren, M.;

Fabiano, S. Complementary Logic Circuits Based on High-Performance n-Type Organic Electrochemical Transistors. *Adv. Mater.* **2018,** *30* (9), 1704916.

(81) Surgailis, J.; Savva, A.; Druet, V.; Paulsen, B. D.; Wu, R. H.; Hamidi-Sakr, A.; Ohayon, D.; Nikiforidis, G.; Chen, X. X.; McCulloch, I.et al. Mixed Conduction in an N-Type Organic Semiconductor in the Absence of Hydrophilic Side-Chains. *Adv. Funct. Mater.* **2021,** *31* (21), 2010165.

(82) Chen, X. X.; Marks, A.; Paulsen, B. D.; Wu, R. H.; Rashid, R. B.; Chen, H.; Alsufyani, M.; Rivnay, J.; McCulloch, I. n-Type Rigid Semiconducting Polymers Bearing Oligo(Ethylene Glycol) Side Chains for High-Performance Organic Electrochemical Transistors. *Angew Chem Int Edit* **2021,** *60* (17), 9368.

(83) Zhu, G.; Chen, J.; Duan, J.; Liao, H.; Zhu, X.; Li, Z.; McCulloch, I.; Yue, W. Fluorinated Alcohol-Processed N-Type Organic Electrochemical Transistor with High Performance and Enhanced Stability. *Acs Appl. Mater. Inter.* **2022,** *14* (38), 43586.

(84) Duan, J. Y.; Zhu, G. M.; Wang, L. W.; Chen, J. X.; Cong, S. Y.; Zhu, X. Y.; Zhou, Y. C.; Li, Z. K.; McCulloch, I.; Yue, W. Highly Efficient Mixed Conduction in N-type Fused Small Molecule Semiconductors. *Adv. Funct. Mater.* **2022,** *32* (34), 2203937.

(85) Marks, A.; Chen, X.; Wu, R.; Rashid, R. B.; Jin, W.; Paulsen, B. D.; Moser, M.; Ji, X.; Griggs, S.; Meli, D.et al. Synthetic Nuances to Maximize n-Type Organic Electrochemical Transistor and Thermoelectric Performance in Fused Lactam Polymers. *J. Am. Chem. Soc.* **2022,** *144* (10), 4642.

(86) Lo, C. Y.; Wu, Y. H.; Awuyah, E.; Meli, D.; Nguyen, D. M.; Wu, R. H.; Xu, B. H.; Strzalka, J.; Rivnay, J.; Martin, D. C.et al. Influence of the molecular weight and size distribution of PSS on mixed ionic-electronic transport in PEDOT:PSS. *Polymer Chemistry* **2022,** *13* (19), 2764.

(87) Giovannitti, A.; Sbircea, D. T.; Inal, S.; Nielsen, C. B.; Bandiello, E.; Hanifi, D. A.; Sessolo, M.; Malliaras, G. G.; McCulloch, I.; Rivnay, J. Controlling the mode of operation of organic transistors through side-chain engineering. *Proc.*

Natl. Acad. Sci. U.S.A. **2016,** *113* (43), 12017.

(88) Savva, A.; Hallani, R.; Cendra, C.; Surgailis, J.; Hidalgo, T. C.; Wustoni, S.; Sheelamanthula, R.; Chen, X. X.; Kirkus, M.; Giovannitti, A.et al. Balancing Ionic and Electronic Conduction for High-Performance Organic Electrochemical Transistors. *Adv. Funct. Mater.* **2020,** *30* (11), 1907657.

(89) Nielsen, C. B.; Giovannitti, A.; Sbircea, D. T.; Bandiello, E.; Niazi, M. R.; Hanifi, D. A.; Sessolo, M.; Amassian, A.; Malliaras, G. G.; Rivnay, J.et al. Molecular Design of Semiconducting Polymers for High-Performance Organic Electrochemical Transistors. *J. Am. Chem. Soc.* **2016,** *138* (32), 10252.

(90) Moser, M.; Savva, A.; Thorley, K.; Paulsen, B. D.; Hidalgo, T. C.; Ohayon, D.; Chen, H.; Giovannitti, A.; Marks, A.; Gasparini, N. Polaron delocalization in donor–acceptor polymers and its impact on organic electrochemical transistor performance. *Angew. Chem. Int. Ed.* **2021,** *60* (14), 7777.

(91) Jia, H.; Huang, Z.; Li, P.; Zhang, S.; Wang, Y.; Wang, J.-Y.; Gu, X.; Lei, T. Engineering donor–acceptor conjugated polymers for high-performance and fast-response organic electrochemical transistors. *J. Mater. Chem. C* **2021,** *9* (14), 4927.

(92) Kawan, M.; Hidalgo, T. C.; Du, W. Y.; Pappa, A. M.; Owens, R. M.; McCulloch, I.; Inal, S. Monitoring supported lipid bilayers with n-type organic electrochemical transistors. *Mater Horiz* **2020,** *7* (9), 2348.

(93) Maria, I. P.; Paulsen, B. D.; Savva, A.; Ohayon, D.; Wu, R. H.; Hallani, R.; Basu, A.; Du, W. Y.; Anthopoulos, T. D.; Inal, S.et al. The Effect of Alkyl Spacers on the Mixed Ionic-Electronic Conduction Properties of N-Type Polymers. *Adv. Funct. Mater.* **2021,** *31* (14), 2008718.

(94) Jeong, D.; Jo, I. Y.; Lee, S.; Kim, J. H.; Kim, Y.; Kim, D.; Reynolds, J. R.; Yoon, M. H.; Kim, B. J. High-Performance n-Type Organic Electrochemical Transistors Enabled by Aqueous Solution Processing of Amphiphilicity-Driven Polymer Assembly. *Adv. Funct. Mater.* **2022,** *32* (16), 2111950.

(95) Maria, I. P.; Griggs, S.; Rashid, R. B.; Paulsen, B. D.; Surgailis, J.; Thorley, K.;

Le, V. N.; Harrison, G. T.; Combe, C.; Hallani, R.et al. Enhancing the Backbone Coplanarity of n-Type Copolymers for Higher Electron Mobility and Stability in Organic Electrochemical Transistors. *Chem. Mater.* **2022,** *34* (19), 8593.

(96) Shi, J. W.; Li, P. Y.; Deng, X. Y.; Xu, J. C.; Huang, Z.; Lei, Y. Q.; Wang, Y. F.; Wang, J. Y.; Gu, X. D.; Lei, T. Revealing the Role of Polaron Distribution on the Performance of n-Type Organic Electrochemical Transistors. *Chem. Mater.* **2022,** *34* (2), 864.

(97) Yang, C. Y.; Stoeckel, M. A.; Ruoko, T. P.; Wu, H. Y.; Liu, X.; Kolhe, N. B.; Wu, Z.; Puttisong, Y.; Musumeci, C.; Massetti, M.et al. A high-conductivity n-type polymeric ink for printed electronics. *Nat Commun* **2021,** *12* (1), 2354.

(98) Lin, P.; Yan, F. Organic thin-film transistors for chemical and biological sensing. *Adv. Mater.* **2012,** *24* (1), 34.

(99) Wang, N.; Yang, A.; Fu, Y.; Li, Y.; Yan, F. Functionalized Organic Thin Film Transistors for Biosensing. *Acc. Chem. Res.* **2019,** *52* (2), 277.

(100) Yang, A.; Li, Y.; Yang, C.; Fu, Y.; Wang, N.; Li, L.; Yan, F. Fabric Organic Electrochemical Transistors for Biosensors. *Adv. Mater.* **2018,** *30* (23), e1800051.

(101) Liu, H.; Yang, A. N.; Song, J. J.; Wang, N. X.; Lam, P. Y.; Li, Y. L.; Law, H. K. W.; Yan, F. Ultrafast, sensitive, and portable detection of COVID-19 IgG using flexible organic electrochemical transistors. *Sci. Adv.* **2021,** *7* (38), eabg8387.

(102) Lin, P.; Luo, X. T.; Hsing, I. M.; Yan, F. Organic Electrochemical Transistors Integrated in Flexible Microfluidic Systems and Used for Label-Free DNA Sensing. *Adv. Mater.* **2011,** *23* (35), 4035.

(103) Hu, J.; Wei, W. W.; Ke, S. M.; Zeng, X. R.; Lin, P. A novel and sensitive sarcosine biosensor based on organic electrochemical transistor. *Electrochim. Acta* **2019,** *307*, 100.

(104) Diamandis, E. P.; Christopoulos, T. K. The biotin-(strept)avidin system: principles and applications in biotechnology. *Clin. Chem.* **1991,** *37* (5), 625.

(105) Pappa, A. M.; Curto, V. F.; Braendlein, M.; Strakosas, X.; Donahue, M. J.;

Fiocchi, M.; Malliaras, G. G.; Owens, R. M. Organic Transistor Arrays Integrated with Finger-Powered Microfluidics for Multianalyte Saliva Testing. *Adv Healthc Mater* **2016,** *5* (17), 2295.

(106) Fu, Y.; Wang, N.; Yang, A.; Law, H. K.; Li, L.; Yan, F. Highly Sensitive Detection of Protein Biomarkers with Organic Electrochemical Transistors. *Adv. Mater.* **2017,** *29* (41), 1703787.

(107) Xie, K.; Wang, N.; Lin, X.; Wang, Z.; Zhao, X.; Fang, P.; Yue, H.; Kim, J.; Luo, J.; Cui, S.et al. Organic electrochemical transistor arrays for real-time mapping of evoked neurotransmitter release in vivo. *Elife* **2020,** *9*, e50345.

(108) Galliani, M.; Diacci, C.; Berto, M.; Sensi, M.; Beni, V.; Berggren, M.; Borsari, M.; Simon, D. T.; Biscarini, F.; Bortolotti, C. A. Flexible Printed Organic Electrochemical Transistors for the Detection of Uric Acid in Artificial Wound Exudate. *Adv Mater Interfaces* **2020,** *7* (23), 2001218.

(109) Diacci, C.; Lee, J. W.; Janson, P.; Dufil, G.; Mehes, G.; Berggren, M.; Simon, D. T.; Stavrinidou, E. Real-Time Monitoring of Glucose Export from Isolated Chloroplasts Using an Organic Electrochemical Transistor. *Adv. Mater. Technol.* **2020,** *5* (3), 1900262.

(110) Zhang, Y.; Wang, Y.; Qing, X.; Wang, Y.; Zhong, W.; Wang, W.; Chen, Y.; Liu, Q.; Li, M.; Wang, D. Fiber organic electrochemical transistors based on multi-walled carbon nanotube and polypyrrole composites for noninvasive lactate sensing. *Anal. Bioanal. Chem.* **2020,** *412* (27), 7515.

(111) Zhu, R. F.; Wang, Y. D.; Tao, Y.; Wang, Y.; Chen, Y. L.; Li, M. F.; Liu, Q. Z.; Yang, L. Y.; Wang, D. Layer-by-layer assembly of composite conductive fiber-based organic electrochemical transistor for highly sensitive detection of sialic acid. *Electrochim. Acta* **2022,** *425*, 140716.

(112) Yu, J.; Yang, A.; Wang, N.; Ling, H.; Song, J.; Chen, X.; Lian, Y.; Zhang, Z.; Yan, F.; Gu, M. Highly sensitive detection of caspase-3 activity based on peptide-modified organic electrochemical transistor biosensors. *Nanoscale* **2021,** *13* (5), 2868.

(113) Liao, C. Z.; Mak, C. H.; Zhang, M.; Chan, H. L. W.; Yan, F. Flexible Organic Electrochemical Transistors for Highly Selective Enzyme Biosensors and Used for Saliva Testing. *Adv. Mater.* **2015,** *27* (4), 676.

(114) Hu, J.; Lu, M. J.; Chen, F. Z.; Jia, H. M.; Zhou, H.; Li, K. Z.; Zeng, X. R.; Zhao, W. W.; Lin, P. Multifunctional Hydrogel Hybrid-Gated Organic Photoelectrochemical Transistor for Biosensing. *Adv. Funct. Mater.* **2022,** *32* (26), 2109046.

(115) Song, J. J.; Lin, P.; Ruan, Y. F.; Zhao, W. W.; Wei, W. W.; Hu, J.; Ke, S. M.; Zeng, X. R.; Xu, J. J.; Chen, H. Y.et al. Organic Photo-Electrochemical Transistor-Based Biosensor: A Proof-of-Concept Study toward Highly Sensitive DNA Detection. *Adv. Healthcare Mater.* **2018,** *7* (19), 1800536.

(116) Ban, R.; Lu, M. J.; Hu, J.; Li, C. J.; Li, Y. M.; Gao, G.; Wang, C. S.; Kong, F. Y.; Zhou, H.; Lin, P.et al. Biological modulating organic photoelectrochemical transistor through in situ enzymatic engineering of photoactive gate for sensitive detection of serum alkaline phosphatase. *Biosens. Bioelectron.* **2022,** *218*, 114752.

(117) Li, Z.; Hu, J.; Gao, G.; Liu, X.-N.; Wu, J.-Q.; Xu, Y.-T.; Zhou, H.; Zhao, W.-W.; Xu, J.-J.; Chen, H.-Y. Organic photoelectrochemical transistor detection of tear lysozyme. *Sensors Diagnostics* **2022,** *1* (2), 294.

(118) Li, C. J.; Xu, Y. T.; Lu, M. J.; Li, Y. M.; Ban, R.; Hu, J.; Gao, G.; Dong, X. Y.; Zhou, H.; Lin, P.et al. Semiconducting metal-organic framework derivatives-gated organic photoelectrochemical transistor immunoassay. *Biosens. Bioelectron.* **2022,** *217*, 114700.

(119) Shi, Z.; Xu, Z.; Hu, J.; Wei, W.; Zeng, X.; Zhao, W. W.; Lin, P. Ascorbic acid-mediated organic photoelectrochemical transistor sensing strategy for highly sensitive detection of heart-type fatty acid binding protein. *Biosens. Bioelectron.* **2022,** *201*, 113958.

(120) Li, Z.; Xu, Y. T.; Hu, J.; Liu, X. N.; Chen, F. Z.; Jia, H. M.; Zhou, H.; Chen, G.; Lin, P.; Zhao, W. W. Light-Fueled Organic Photoelectrochemical Transistor for

Probing Membrane Protein in an H-Cell. *Adv Mater Interfaces* **2022,** *9* (3), 2102040.

(121) Lu, M. J.; Chen, F. Z.; Hu, J.; Zhou, H.; Chen, G. X.; Yu, X. D.; Ban, R.; Lin, P.; Zhao, W. W. Regulating Light-Sensitive Gate of Organic Photoelectrochemical Transistor toward Sensitive Biodetection at Zero Gate Bias. *Small Struct* **2021,** *2* (11), 2100087.

(122) Gao, G.; Chen, J.-H.; Li, C.-J.; Wang, C.-S.; Hu, J.; Zhou, H.; Lin, P.; Xu, Q.; Zhao, W.-W. Duplex-Specific Nuclease-Enabled Target Recycling on Semiconducting Metal–Organic Framework Heterojunctions for Energy-Transfer-Based Organic Photoelectrochemical Transistor miRNA Biosensing. *Anal. Chem.* **2022**.

(123) Gao, G.; Hu, J.; Li, Z.; Xu, Q.; Wang, C. S.; Jia, H. M.; Zhou, H.; Lin, P.; Zhao, W. W. Hybridization chain reaction for regulating surface capacitance of organic photoelectrochemical transistor toward sensitive miRNA detection. *Biosens. Bioelectron.* **2022,** *209*, 114224.

(124) Lu, M.-J.; Li, C.-J.; Ban, R.; Chen, F.-Z.; Hu, J.; Gao, G.; Zhou, H.; Lin, P.; Zhao, W.-W. Tuning the Surface Molecular Charge of Organic Photoelectrochemical Transistors with Significantly Improved Signal Resolution: A General Strategy toward Sensitive Bioanalysis. *ACS sensors* **2022,** *7* (9), 2788.

(125) Fenoy, G. E.; von Bilderling, C.; Knoll, W.; Azzaroni, O.; Marmisolle, W. A. PEDOT:Tosylate-Polyamine-Based Organic Electrochemical Transistors for High-Performance Bioelectronics. *Adv. Electron. Mater.* **2021,** *7* (6), 2100059.

(126) Aerathupalathu Janardhanan, J.; Chen, Y.-L.; Liu, C.-T.; Tseng, H.-S.; Wu, P.-I.; She, J.-W.; Hsiao, Y.-S.; Yu, H.-h. Sensitive Detection of Sweat Cortisol Using an Organic Electrochemical Transistor Featuring Nanostructured Poly (3, 4-Ethylenedioxythiophene) Derivatives in the Channel Layer. *Anal. Chem.* **2022**.

(127) Bonafè, F.; Decataldo, F.; Zironi, I.; Remondini, D.; Cramer, T.; Fraboni, B. AC amplification gain in organic electrochemical transistors for impedance-based

single cell sensors. *Nat. Commun.* **2022,** *13* (1), 1.

(128) Yeung, S. Y.; Gu, X.; Tsang, C. M.; Tsao, S. W. G.; Hsing, I. M. Organic electrochemical transistor array for monitoring barrier integrity of epithelial cells invaded by nasopharyngeal carcinoma. *Sensor Actuat B-Chem* **2019,** *297*, 126761.

(129) Yeung, S. Y.; Gu, X.; Tsang, C. M.; Tsao, S. W.; Hsing, I. M. Engineering organic electrochemical transistor (OECT) to be sensitive cell-based biosensor through tuning of channel area. *Sensor Actuat a-Phys* **2019,** *287*, 185.

(130) Wei, W.; Xiao, K.; Tao, M.; Nie, L.; Liu, D.; Ke, S.; Zeng, X.; Hu, Z.; Lin, P.; Zhang, Y. A Novel Organic Electrochemical Transistor-Based Platform for Monitoring the Senescent Green Vegetative Phase of Haematococcus pluvialis Cells. *Sensors (Basel)* **2017,** *17* (9), 1997.

(131) Pappa, A. M.; Ohayon, D.; Giovannitti, A.; Maria, I. P.; Savva, A.; Uguz, I.; Rivnay, J.; McCulloch, I.; Owens, R. M.; Inal, S. Direct metabolite detection with an n-type accumulation mode organic electrochemical transistor. *Sci Adv* **2018,** *4* (6), eaat0911.

(132) Koklu, A.; Ohayon, D.; Wustoni, S.; Hama, A.; Chen, X. X.; McCulloch, I.; Inal, S. Microfluidics integrated n-type organic electrochemical transistor for metabolite sensing. *Sensor Actuat B-Chem* **2021,** *329*, 129251.

(133) Decataldo, F.; Barbalinardo, M.; Tessarolo, M.; Vurro, V.; Calienni, M.; Gentili, D.; Valle, F.; Cavallini, M.; Fraboni, B. Organic Electrochemical Transistors: Smart Devices for Real-Time Monitoring of Cellular Vitality. *Adv Mater Technol-Us* **2019,** *4* (9), 1900207.

(134) Decataldo, F.; Barbalinardo, M.; Gentili, D.; Tessarolo, M.; Calienni, M.; Cavallini, M.; Fraboni, B. Organic electrochemical transistors for real-time monitoring of in vitro silver nanoparticle toxicity. *Advanced Biosystems* **2020,** *4* (1), 1900204.

(135) Decataldo, F.; Grumiro, L.; Marino, M. M.; Faccin, F.; Giovannini, C.; Brandolini, M.; Dirani, G.; Taddei, F.; Lelli, D.; Tessarolo, M.et al. Fast and

real-time electrical transistor assay for quantifying SARS-CoV-2 neutralizing antibodies. *Commun Mater* **2022,** *3* (1), 1.

(136) Pitsalidis, C.; Ferro, M. P.; Iandolo, D.; Tzounis, L.; Inal, S.; Owens, R. M. Transistor in a tube: A route to three-dimensional bioelectronics. *Sci Adv* **2018,** *4* (10), eaat4253.

(137) Khodagholy, D.; Curto, V. F.; Fraser, K. J.; Gurfinkel, M.; Byrne, R.; Diamond, D.; Malliaras, G. G.; Benito-Lopez, F.; Owens, R. M. Organic electrochemical transistor incorporating an ionogel as a solid state electrolyte for lactate sensing. *J. Mater. Chem.* **2012,** *22* (10), 4440.

(138) Scheiblin, G.; Aliane, A.; Strakosas, X.; Curto, V. F.; Coppard, R.; Marchand, G.; Owens, R. M.; Mailley, P.; Malliaras, G. G. Screen-printed organic electrochemical transistors for metabolite sensing. *MRS Commun.* **2015,** *5* (3), 507.

(139) Bihar, E.; Deng, Y.; Miyake, T.; Saadaoui, M.; Malliaras, G. G.; Rolandi, M. A Disposable paper breathalyzer with an alcohol sensing organic electrochemical transistor. *Sci. Rep.* **2016,** *6* (1), 27582.

(140) Lieberth, K.; Brückner, M.; Torricelli, F.; Mailänder, V.; Gkoupidenis, P.; Blom, P. W. Monitoring Reversible Tight Junction Modulation with a Current-Driven Organic Electrochemical Transistor. *Adv Mater Technol-Us* **2021,** *6* (5), 2000940.

(141) Bean, B. P. The action potential in mammalian central neurons. *Nat. Rev. Neurosci.* **2007,** *8* (6), 451.

(142) AlGhatrif, M.; Lindsay, J. A brief review: history to understand fundamentals of electrocardiography. *J Community Hosp Intern Med Perspect* **2012,** *2* (1), 14383.

(143) Lee, H.; Lee, S.; Lee, W.; Yokota, T.; Fukuda, K.; Someya, T. Ultrathin Organic Electrochemical Transistor with Nonvolatile and Thin Gel Electrolyte for Long-Term Electrophysiological Monitoring. *Adv. Funct. Mater.* **2019,** *29* (48), 1906982.

(144) Leleux, P.; Rivnay, J.; Lonjaret, T.; Badier, J. M.; Benar, C.; Herve, T.; Chauvel, P.; Malliaras, G. G. Organic electrochemical transistors for clinical applications. *Adv. Healthcare Mater.* **2015,** *4* (1), 142.

(145) Lee, W.; Kim, D.; Rivnay, J.; Matsuhisa, N.; Lonjaret, T.; Yokota, T.; Yawo, H.; Sekino, M.; Malliaras, G. G.; Someya, T. Integration of Organic Electrochemical and Field-Effect Transistors for Ultraflexible, High Temporal Resolution Electrophysiology Arrays. *Adv. Mater.* **2016,** *28* (44), 9722.

(146) Shalf, J. The future of computing beyond Moore's Law. *Philosophical Transactions of the Royal Society a-Mathematical Physical and Engineering Sciences* **2020,** *378* (2166), 20190061.

(147) Ye, P. D.; Ernst, T.; Khare, M. V. The last silicon transistor: Nanosheet devices could be the final evolutionary step for Moore's Law. *Ieee Spectrum* **2019,** *56* (8), 30.

(148) Janissek, A.; Lenz, J.; Giudice, F. d.; Gaulke, M.; Pyatkov, F.; Dehm, S.; Hennrich, F.; Wei, L.; Chen, Y.; Fediai, A. Ionic liquid gating of single-walled carbon nanotube devices with ultra-short channel length down to 10 nm. *Appl. Phys. Lett.* **2021,** *118* (6), 063101.

(149) Desai, S. B.; Madhvapathy, S. R.; Sachid, A. B.; Llinas, J. P.; Wang, Q.; Ahn, G. H.; Pitner, G.; Kim, M. J.; Bokor, J.; Hu, C.et al. MoS2 transistors with 1-nanometer gate lengths. *Science* **2016,** *354* (6308), 99.

(150) Wu, F.; Tian, H.; Shen, Y.; Hou, Z.; Ren, J.; Gou, G.; Sun, Y.; Yang, Y.; Ren, T. L. Vertical MoS2 transistors with sub-1-nm gate lengths. *Nature* **2022,** *603* (7900), 259.

(151) Liu, L. T.; Kong, L. A.; Li, Q. Y.; He, C. L.; Ren, L. W.; Tao, Q. Y.; Yang, X. D.; Lin, J.; Zhao, B.; Li, Z. W.et al. Transferred van der Waals metal electrodes for sub-1-nm MoS2 vertical transistors. *Nat. Electron.* **2021,** *4* (5), 342.

(152) Fry-Bouriaux, L.; Rosamond, M.; Williams, D.; Davies, A.; Wälti, C. Field-enhanced direct tunneling in ultrathin atomic-layer-deposition-grown Au− Al 2 O 3-Cr metal-insulator-metal structures. *Phys. Rev. B* **2017,** *96* (11), 115435.

(153) Groner, M. D.; Fabreguette, F. H.; Elam, J. W.; George, S. M. Low-temperature Al2O3 atomic layer deposition. *Chem. Mater.* **2004,** *16* (4), 639.

(154) Rivnay, J.; Inal, S.; Salleo, A.; Owens, R. M.; Berggren, M.; Malliaras, G. G. Organic electrochemical transistors. *Nat. Rev. Mater.* **2018,** *3* (2), 1.

(155) Rashid, R. B.; Du, W.; Griggs, S.; Maria, I. P.; McCulloch, I.; Rivnay, J. Ambipolar inverters based on cofacial vertical organic electrochemical transistor pairs for biosignal amplification. *Sci Adv* **2021,** *7* (37), eabh1055.

(156) Donahue, M. J.; Williamson, A.; Strakosas, X.; Friedlein, J. T.; McLeod, R. R.; Gleskova, H.; Malliaras, G. G. High-Performance Vertical Organic Electrochemical Transistors. *Adv. Mater.* **2018,** *30* (5), 1705031.

(157) Lenz, J.; Seiler, A. M.; Geisenhof, F. R.; Winterer, F.; Watanabe, K.; Taniguchi, T.; Weitz, R. T. High-performance vertical organic transistors of sub-5 nm channel length. *Nano Lett.* **2021,** *21* (10), 4430.

(158) Paudel, P. R.; Skowrons, M.; Dahal, O.; Krishnan, R. K. R.; Lussem, B. The Transient Response of Organic Electrochemical Transistors. *Adv. Theory Simul.* **2022,** *5* (5), 2100563.

(159) Friedlein, J. T.; Donahue, M. J.; Shaheen, S. E.; Malliaras, G. G.; McLeod, R. R. J. A. M. Microsecond response in organic electrochemical transistors: exceeding the ionic speed limit. **2016,** *28* (38), 8398.

(160) Inal, S.; Rivnay, J.; Hofmann, A. I.; Uguz, I.; Mumtaz, M.; Katsigiannopoulos, D.; Brochon, C.; Cloutet, E.; Hadziioannou, G.; Malliaras, G. G. Organic Electrochemical Transistors Based on PEDOT with Different Anionic Polyelectrolyte Dopants. *J. Polym. Sci., Part B: Polym. Phys.* **2016,** *54* (2), 147.

(161) Lee, S. K.; Cho, Y. W.; Lee, J. S.; Jung, Y. R.; Oh, S. H.; Sun, J. Y.; Kim, S.; Joo, Y. C. Nanofiber Channel Organic Electrochemical Transistors for Low-Power Neuromorphic Computing and Wide-Bandwidth Sensing Platforms. *Adv Sci* **2021,** *8* (10), 2001544.

(162) Doris, S. E.; Pierre, A.; Street, R. A. Dynamic and Tunable Threshold Voltage in Organic Electrochemical Transistors. *Adv. Mater.* **2018,** *30* (15), e1706757.

(163) Romele, P.; Ghittorelli, M.; Kovacs-Vajna, Z. M.; Torricelli, F. Ion buffering and interface charge enable high performance electronics with organic electrochemical transistors. *Nat Commun* **2019,** *10* (1), 3044.

(164) Yang, C. Y.; Tu, D.; Ruoko, T. P.; Gerasimov, J. Y.; Wu, H. Y.; Harikesh, P. C.; Massetti, M.; Stoeckel, M. A.; Kroon, R.; Müller, C. Low-Power/High-Gain Flexible Complementary Circuits Based on Printed Organic Electrochemical Transistors. *Adv. Electron. Mater.* **2022,** *8* (3), 2100907.

(165) Zhang, Y. X.; Ye, G.; van der Pol, T. P. A.; Dong, J. J.; van Doremaele, E. R. W.; Krauhausen, I.; Liu, Y. R.; Gkoupidenis, P.; Portale, G.; Song, J.et al. High-Performance Organic Electrochemical Transistors and Neuromorphic Devices Comprising Naphthalenediimide-Dialkoxybithiazole Copolymers Bearing Glycol Ether Pendant Groups. *Adv. Funct. Mater.* **2022,** *32* (27), 2201593.

(166) Ha, M.; Seo, J.-W. T.; Prabhumirashi, P. L.; Zhang, W.; Geier, M. L.; Renn, M. J.; Kim, C. H.; Hersam, M. C.; Frisbie, C. D. Aerosol jet printed, low voltage, electrolyte gated carbon nanotube ring oscillators with sub-5 μs stage delays. *Nano Lett.* **2013,** *13* (3), 954.

(167) Zare Bidoky, F.; Tang, B.; Ma, R.; Jochem, K. S.; Hyun, W. J.; Song, D.; Koester, S. J.; Lodge, T. P.; Frisbie, C. D. Sub-3 V ZnO electrolyte-gated transistors and circuits with screen-printed and photo-crosslinked ion gel gate dielectrics: New routes to improved performance. *Adv. Funct. Mater.* **2020,** *30* (20), 1902028.

(168) Bidoky, F. Z.; Frisbie, D. Sub-3V, MHz-Class Electrolyte-Gated Transistors and Inverters. **2022**.

(169) Yao, Y.; Huang, W.; Chen, J.; Wang, G.; Chen, H.; Zhuang, X.; Ying, Y.; Ping, J.; Marks, T. J.; Facchetti, A. Flexible complementary circuits operating at sub-0.5 V via hybrid organic–inorganic electrolyte-gated transistors. *Proc. Natl. Acad. Sci.* **2021,** *118* (44).

(170) Yang, P.; Wang, X. COVID-19: a new challenge for human beings. *Cell. Mol. Immunol.* **2020,** *17* (5), 555.

(171) Li, X.; Geng, M.; Peng, Y.; Meng, L.; Lu, S. Molecular immune pathogenesis

and diagnosis of COVID-19. *J. Pharm. Anal.* **2020,** *10* (2), 102.

(172) Petherick, A. Developing antibody tests for SARS-CoV-2. *Lancet* **2020,** *395* (10230), 1101.

(173) Böger, B.; Fachi, M. M.; Vilhena, R. O.; de Fátima Cobre, A.; Tonin, F. S.; Pontarolo, R. Systematic review with meta-analysis of the accuracy of diagnostic tests for COVID-19. *Am. J. Infect. Control* **2021,** *49*, 21.

(174) Assadiasl, S.; Fatahi, Y.; Zavvar, M.; Nicknam, M. H. COVID-19: Significance of antibodies. *Hum. Antibodies* **2020,** *28* (4), 287.

(175) Li, K.; Huang, B.; Wu, M.; Zhong, A.; Li, L.; Cai, Y.; Wang, Z.; Wu, L.; Zhu, M.; Li, J.et al. Dynamic changes in anti-SARS-CoV-2 antibodies during SARS-CoV-2 infection and recovery from COVID-19. *Nat. Commun.* **2020,** *11* (1), 6044.

(176) Muruato, A. E.; Fontes-Garfias, C. R.; Ren, P.; Garcia-Blanco, M. A.; Menachery, V. D.; Xie, X.; Shi, P. Y. A high-throughput neutralizing antibody assay for COVID-19 diagnosis and vaccine evaluation. *Nat. Commun.* **2020,** *11* (1), 4059.

(177) Eckerle, I.; Meyer, B. SARS-CoV-2 seroprevalence in COVID-19 hotspots. *Lancet* **2020,** *396* (10250), 514.

(178) Peeling, R. W.; Wedderburn, C. J.; Garcia, P. J.; Boeras, D.; Fongwen, N.; Nkengasong, J.; Sall, A.; Tanuri, A.; Heymann, D. L. Serology testing in the COVID-19 pandemic response. *Lancet Infect. Dis.* **2020,** *20* (9), 245.

(179) Wang, Q.; Du, Q.; Guo, B.; Mu, D.; Lu, X.; Ma, Q.; Guo, Y.; Fang, L.; Zhang, B.; Zhang, G.et al. A method to prevent SARS-CoV-2 IgM false positives in gold immunochromatography and enzyme-linked immunosorbent assays. *J. Clin. Microbiol.* **2020,** *58* (6), e00375.

(180) Isabel, M.; Damien, G.; Benoit, K.; Hafid, D.; Soleimani, R.; Vincenzo, C.; Olivier, V.; Beatrice, G.; Fleur, W.; Rodriguez-Villalobos, H. Evaluation of two automated and three rapid lateral flow immunoassays for the detection of anti-SARS-CoV-2 antibodies. *J. Clin. Virol.* **2020,** *128*, 104413.

(181) Liu, T.; Hsiung, J.; Zhao, S.; Kost, J.; Sreedhar, D.; Hanson, C. V.; Olson, K.; Keare, D.; Chang, S. T.; Bliden, K. P.et al. Quantification of antibody avidities and accurate detection of SARS-CoV-2 antibodies in serum and saliva on plasmonic substrates. *Nat. Biomed. Eng.* **2020,** *4* (12), 1188.

(182) Li, X. Y.; Pomares, C.; Peyron, F.; Press, C. J.; Ramirez, R.; Geraldine, G.; Cannavo, I.; Chapey, E.; Levigne, P.; Wallon, M.et al. Plasmonic gold chips for the diagnosis of Toxoplasma gondii, CMV, and rubella infections using saliva with serum detection precision. *Eur. J. Clin. Microbiol. Infect. Dis.* **2019,** *38* (5), 883.

(183) Isho, B.; Abe, K. T.; Zuo, M.; Jamal, A. J.; Rathod, B.; Wang, J. H.; Li, Z.; Chao, G.; Rojas, O. L.; Bang, Y. M.et al. Persistence of serum and saliva antibody responses to SARS-CoV-2 spike antigens in COVID-19 patients. *Sci. Immunol.* **2020,** *5* (52).

(184) Romele, P.; Gkoupidenis, P.; Koutsouras, D. A.; Lieberth, K.; Kovacs-Vajna, Z. M.; Blom, P. W. M.; Torricelli, F. Multiscale real time and high sensitivity ion detection with complementary organic electrochemical transistors amplifier. *Nat. Commun.* **2020,** *11* (1), 3743.

(185) Lin, P.; Yan, F.; Yu, J. J.; Chan, H. L. W.; Yang, M. The Application of Organic Electrochemical Transistors in Cell-Based Biosensors. *Adv. Mater.* **2010,** *22* (33), 3655.

(186) Wang, N.; Liu, Y.; Fu, Y.; Yan, F. AC Measurements Using Organic Electrochemical Transistors for Accurate Sensing. *Acs Appl. Mater. Inter.* **2018,** *10* (31), 25834.

(187) Burgi, T. Properties of the gold-sulphur interface: from self-assembled monolayers to clusters. *Nanoscale* **2015,** *7* (38), 15553.

(188) Gao, Z. L.; Ducos, P.; Ye, H. C.; Zauberman, J.; Sriram, A.; Yang, X. P.; Wang, Z. Y.; Mitchell, M. W.; Lekkas, D.; Brisson, D.et al. Graphene transistor arrays functionalized with genetically engineered antibody fragments for Lyme disease diagnosis. *2D Mater.* **2020,** *7* (2), 024001.

(189) Ierardi, V.; Ferrera, F.; Millo, E.; Damonte, G.; Filaci, G.; Valbusa, U. Bioactive surfaces for antibody-antigen complex detection by Atomic Force Microscopy. *J. Phys.: Conf. Ser.* **2013,** *439* (1), 012001.

(190) Haris, P. I.; Severcan, F. FTIR spectroscopic characterization of protein structure in aqueous and non-aqueous media. *J. Mol. Catal. B: Enzym.* **1999,** *7* (1-4), 207.

(191) Kong, J.; Yu, S. Fourier transform infrared spectroscopic analysis of protein secondary structures. *Acta Biochim. Biophys. Sin.* **2007,** *39* (8), 549.

(192) Long, G. L.; Winefordner, J. D. Limit of detection. A closer look at the IUPAC definition. *Anal. Chem.* **2008,** *55* (7), 712A.

(193) Gitlin, I.; Carbeck, J. D.; Whitesides, G. M. Why are proteins charged? Networks of charge-charge interactions in proteins measured by charge ladders and capillary electrophoresis. *Angew. Chem., Int. Ed.* **2006,** *45* (19), 3022.

(194) Bernards, D. A.; Macaya, D. J.; Nikolou, M.; DeFranco, J. A.; Takamatsu, S.; Malliaras, G. G. Enzymatic sensing with organic electrochemical transistors. *J. Mater. Chem. C* **2008,** *18* (1), 116.

(195) Thompson, M.; Cheran, L. E.; Zhang, M.; Chacko, M.; Huo, H.; Sadeghi, S. Label-free detection of nucleic acid and protein microarrays by scanning Kelvin nanoprobe. *Biosens. Bioelectron.* **2005,** *20* (8), 1471.

(196) Kukic, P.; Farrell, D.; McIntosh, L. P.; Garcia-Moreno, E. B.; Jensen, K. S.; Toleikis, Z.; Teilum, K.; Nielsen, J. E. Protein dielectric constants determined from NMR chemical shift perturbations. *J. Am. Chem. Soc.* **2013,** *135* (45), 16968.

(197) Bhalla, N.; Pan, Y.; Yang, Z.; Payam, A. F. Opportunities and challenges for biosensors and nanoscale analytical tools for pandemics: COVID-19. *Acs Nano* **2020,** *14* (7), 7783.

(198) Stern, E.; Wagner, R.; Sigworth, F. J.; Breaker, R.; Fahmy, T. M.; Reed, M. A. Importance of the Debye screening length on nanowire field effect transistor sensors. *Nano Lett.* **2007,** *7* (11), 3405.

(199) Hammock, M. L.; Knopfmacher, O.; Naab, B. D.; Tok, J. B. H.; Bao, Z. A. Investigation of protein detection parameters using nanofunctionalized organic field-effect transistors. *Acs Nano* **2013,** *7* (5), 3970.

(200) Hartvig, R. A.; van de Weert, M.; Ostergaard, J.; Jorgensen, L.; Jensen, H. Protein adsorption at charged surfaces: the role of electrostatic interactions and interfacial charge regulation. *Langmuir* **2011,** *27* (6), 2634.

(201) Li, Q.; Gordon, M.; Cao, C.; Ugen, K. E.; Morgan, D. Improvement of a low pH antigen-antibody dissociation procedure for ELISA measurement of circulating anti-Aβ antibodies. *BMC Neurosci.* **2007,** *8* (1), 1.

(202) Bergveld, P. Thirty years of ISFETOLOGY - What happened in the past 30 years and what may happen in the next 30 years. *Sens. Actuators, B* **2003,** *88* (1), 1.

(203) Yan, F.; Estrela, P.; Mo, Y.; Migliorato, P.; Maeda, H.; Inoue, S.; Shimoda, T. Polycrystalline silicon ion sensitive field effect transistors. *Appl. Phys. Lett.* **2005,** *86* (5), 053901.

(204) Zeng, W.; Ma, H.; Ding, C.; Yang, Y.; Sun, Y.; Huang, X.; He, W.; Xiang, Y.; Gao, Y.; Jin, T. Characterization of SARS-CoV-2-specific antibodies in COVID-19 patients reveals highly potent neutralizing IgA. *Signal Transduction Targeted Ther.* **2021,** *6* (1), 35.

(205) Emaminejad, S.; Javanmard, M.; Gupta, C.; Chang, S.; Davis, R. W.; Howe, R. T. Tunable control of antibody immobilization using electric field. *Proc. Natl. Acad. Sci. U. S. A.* **2015,** *112* (7), 1995.

(206) Hekstra, D. R.; White, K. I.; Socolich, M. A.; Henning, R. W.; Srajer, V.; Ranganathan, R. Electric-field-stimulated protein mechanics. *Nature* **2016,** *540* (7633), 400.

(207) Torrente-Rodriguez, R. M.; Lukas, H.; Tu, J. B.; Min, J. H.; Yang, Y. R.; Xu, C. H.; Rossiter, H. B.; Gao, W. SARS-CoV-2 RapidPlex: A graphene-based multiplexed telemedicine platform for rapid and low-cost COVID-19 diagnosis and monitoring. *Matter* **2020,** *3* (6), 1981.

(208) Funari, R.; Chu, K. Y.; Shen, A. Q. Detection of antibodies against SARS-CoV-

2 spike protein by gold nanospikes in an opto-microfluidic chip. *Biosens. Bioelectron* **2020,** *169*, 112578.

(209) Tan, X.; Krel, M.; Dolgov, E.; Park, S.; Li, X.; Wu, W.; Sun, Y. L.; Zhang, J.; Khaing Oo, M. K.; Perlin, D. S.et al. Rapid and quantitative detection of SARS-CoV-2 specific IgG for convalescent serum evaluation. *Biosens. Bioelectron* **2020,** *169*, 112572.

(210) Wang, Z.; Zheng, Z.; Hu, H.; Zhou, Q.; Liu, W.; Li, X.; Liu, Z.; Wang, Y.; Ma, Y. A point-of-care selenium nanoparticle-based test for the combined detection of anti-SARS-CoV-2 IgM and IgG in human serum and blood. *Lab Chip* **2020,** *20* (22), 4255.

(211) Lin, Q. Y.; Wen, D. H.; Wu, J.; Liu, L. L.; Wu, W. J.; Fang, X. E.; Kong, J. L. Microfluidic immunoassays for sensitive and simultaneous detection of IgG/IgM/antigen of SARS-CoV-2 within 15 min. *Anal. Chem.* **2020,** *92* (14), 9454.

(212) Li, Z.; Yi, Y.; Luo, X.; Xiong, N.; Liu, Y.; Li, S.; Sun, R.; Wang, Y.; Hu, B.; Chen, W.et al. Development and clinical application of a rapid IgM-IgG combined antibody test for SARS-CoV-2 infection diagnosis. *J. Med. Virol.* **2020,** *92*, 1518.